Structural and bioenergetic changes in tumour spheroids during growth



Katarzyna Bloch

St Cross College

Nuffield Department of Clinical Laboratory Sciences

Life Sciences Interface Doctoral Training Centre

University of Oxford

Supervisors: Dr Catherine Kelly and Prof Philip Maini

A thesis submitted for the degree of *Doctor of Philosophy*

Trinity Term 2012

Structural and bioenergetic changes in tumour spheroids during growth

Katarzyna Bloch, St Cross College

A thesis submitted for the degree of Doctor of Philosophy

Trinity Term 2012

Abstract

Multicellular tumour spheroids (TS) are an *in vitro* model of avascular tumours, and have been widely used to investigate tumour growth, metabolism and hypoxia. The geometry of the TS lends itself to mathematical representation, and theoretical models of TS growth and the development of hypoxia are abundant. With some notable exceptions however, these models have been developed independently of the biological data collection process and are overwhelmingly based upon data from multiple sources. Thus, whilst mathematical modeling has the potential to help explain and guide biological experiments, without reliable data it is unlikely to live up to this expectation.

In this thesis, a combination of experimental and theoretical approaches was used to characterize the relationship between proliferation, hypoxia and metabolism during the growth of TS derived from the DLD-1 human colon adenocarcinoma cell line. Experimental data were collected over the entire period of TS growth, generating a high volume of predominantly imaging data. To facilitate the extraction of quantitative information from this, a suite of image analysis software, which is readily applicable to other data sets, was developed. During growth, the DLD-1 TS maintained a macroscopic spherical geometry but at the microscale level the TS boundary was increasingly irregular, with TS disintegrating rapidly after 20 days. Immunofluorescence (IF) studies showed that hypoxia developed soon after TS initiation, followed by the characteristic onset of necrosis. Reduced proliferation was found to be concomitant with the development of hypoxia, although some cells retained proliferative capacity even under severely hypoxic conditions. Towards the end of culture, TS were primarily comprised of severely hypoxic and necrotic cells, a probable cause of disintegration.

Mathematical simulation of oxygen gradients in TS using literature-based values for the maximal rate of oxygen consumption was used to estimate the partial oxygen pressure (pO_2) at which the IF marker of hypoxia was bound. Assuming a spatially-invariant rate of oxygen consumption, the model predicted that the onset of hypoxic binding occurs at pO_2 levels similar to those reported in the literature, however the onset of necrosis was overestimated. Mathematical simulations predicted that oxygen consumption decreases as TSs increase in size, supporting previous observations.

The Warburg Effect, where glucose metabolism is favoured even under aerobic conditions, is a hallmark of tumours. Although development of the glycolytic phenotype during TS growth was observed in the form of an elevated activity of the lactate dehydrogenase V (LDHV) enzyme, the activity and expression of other glycolytic enzymes, such as hexokinase II (HKII), was unaltered. Whilst the spatial distribution of HKII was unrestricted throughout the TS's viable fraction, LDHV expression was elevated in regions of hypoxia, suggesting constant adaptation of tumour cells to their microenvironment.

In addition to the above findings, the data generated have been collected and analysed in the context of the requirements of theoretical modelling at each step; thus, they can be used to parameterise and inform more sophisticated models of tumour metabolism.

Acknowledgements

First and foremost I would like to thank Filip to whom I dedicate this thesis to. I would like to thank my supervisors, Cat and Philip, who have been very supportive and provided lots of guidance. I am especially grateful to Alex who has been my supervisor and a true friend from the beginning of my Doctoral Training Centre studies. Finally, I am indebted to my mother and sister for their unwavering support throughout my entire education.

Contents

1 Introduction 1

1.1 Cancer metabolism and the microenvironment 1
1.2 Multicellular tumour spheroids 5
1.3 The value of mathematical modelling 7
1.4 The DLD-1 cell line 9
1.5 Thesis outline 10
1.6 Statement of originality 12

2 Materials and methods 14

2.1 Cell Culture 14
2.1.1 Cell line initiation and maintenance 14
2.1.2 Cell cryopreservation and storage 15
2.1.3 Cell density measurement 16
2.2 TS preparation protocol 16
2.2.1 TS initiation and maintenance 16
2.2.2 TS homogenates 17
2.2.3 TS growth measurement 17
2.2.4 TS fixation and cryopreservation 18
2.3 TS-based assays 18
2.3.1 Glucose concentration 19
2.3.2 Lactate concentration 20
2.4 Enzyme activity protocols 21
2.4.1 Quantification of protein concentration 21
2.4.2 Enzyme reaction components 22
2.4.3 Enzyme activity calculations 24
2.5 Immunofluorescence 25
2.5.1 IHC markers description 25
2.5.2 EF5 incubation 27
2.5.3 Ki-67 and EF5 co-staining 27
2.5.4 Image analysis pre-processing 30
2.5.5 HKII and LDHV detection 31
2.6 Western blots 33
2.6.1 Sample preparation 33
2.6.2 Gel electrophoresis 33
2.6.3 Blotting protocol 34
2.6.4 Membrane development 35

3 Changes in TS size and morphology during culture 37

3.1 Introduction 37
3.1.1 Assessment of TS size 40
3.1.2 Characterising TS growth 42
3.1.3 Logistic and Gompertz models of TS growth kinetics 45
3.2 Aim of work 47
3.3 Methods 48
3.3.1 Image acquisition 48
3.3.2 Automated image analysis of TS growth 48
3.4 Results 52
3.5 Discussion 60

4 The relationship between hypoxia and cell proliferation in TS 65

4.1 Introduction 66
4.1.1 Tumour hypoxia 66
4.1.2 The cellular response to hypoxia is coordinated by HIF-1 67
4.1.3 Hypoxia and proliferation 69
4.1.4 The TS as a desirable model for investigating the relationship between hypoxia and proliferation 73
4.1.5 Experimental evaluation of tissue hypoxia 75
4.1.6 Aim of work 77
4.2 Methods 77
4.2.1 IHC markers 77
4.2.2 Epifluorescent image analysis of TS cross-sections 77
4.3 Results 83
4.3.1 Quantitative assessment of changes in normoxia, hypoxia and severe hypoxia during TS development 85
4.3.2 Proliferation decreases, but is not fully diminished, under hypoxia 87
4.4 Discussion 90

5 Integrative study of the role of proliferation in defining oxygen gradients in TS 93

5.1 Introduction 93
5.1.1 Oxygen consumption in TS 95
5.1.2 Oxygen consumption rates in the literature 97
5.2 Aim of work 100
5.3 Model development 100
5.3.1 Modelling oxygen diffusion 101
5.3.2 Modelling oxygen consumption 103

5.3.3 Parameter estimation 106
5.3.4 Non-dimensionalisation 107
5.3.5 Numerical solution 109
5.4 Results 110
5.4.1 The effect of cell size 110
5.4.2 Estimation of parameter values for Model 1 and Model 2 suggests that oxygen consumption decreases during TS culture 113
5.4.3 Considering the effect of proliferation on oxygen consumption does not improve estimation of hypoxia 115
5.5 Discussion 120

6 Development of the glycolytic phenotype in TSs 125
6.1 Introduction 126
6.1.1 The central role of glucose consumption in tumour metabolism 126
6.1.2 Glycolysis and proliferation 131
6.1.3 Glycolytic enzymes and cancer 133
6.1.4 HIF-1 as a modulator of glycolysis in tumour cells 138
6.2 Aim of this work 142
6.3 Experimental methods 143
6.4 Results 145
6.4.1 Changes in glucose and lactate levels in TS medium 145
6.4.2 Changes in glucose and lactate consumption per viable TS cell 147
6.4.3 Summary of changes in glucose and lactate metabolism 150
6.4.4 Characterisation of key-glycolytic enzymes in DLD-1 TS homogenates 150
6.4.5 Evaluation of HIF-1α content in DLD-1 TS homogenates 157
6.4.6 Changes in the spatio-temporal distribution of HKII and LDHV 158
6.5 Discussion 159

7 Summary and further work 166
7.1 Summary 166
7.2 Further work 172

Acronyms 178
Bibliography 184

Chapter 1 Introduction

1.1 Cancer metabolism and the microenvironment

Cancer is the second most common cause of mortality in the developed world, accounting for 7.6 million deaths worldwide in 2008 [1-3]. Rather than a single disease, cancer represents a group of diseases characterised by dynamic changes in the genome that lead to deregulated cell growth and invasion from the primary site to other locations in the body [4]. A variety of genomic alterations have been found to underlie tumourgenesis, from point mutations to multiple genetic alterations including changes in deoxyribonucleic acid (DNA) content, and entire chromosome fragments [5]. The common feature in all of those alterations is that they offer some form of growth advantage during the process of tumour development.

Most normal and healthy cells will not proliferate unless they are stimulated to do so by some extracellular signals, mainly mitogenic factors. Growth factor-initiated signal transduction, as well as nutrient status and intracellular signals, have to be integrated for a cell to decide if it is going to proliferate or maintain a quiescent state [6]. Cancer cells, by interferring in the relay of information transmitted by the signalling pathways, alter the cellular response, leading to upregulated growth and invasion [7].

One of the consequences of dysregulated growth is tumour hypoxia, where the rapidly growing tumour mass outstrips the ability of its vasculature to supply sufficient oxygen. Hypoxia leads to resistance to both radiotherapy and chemotherapy [8]. Additionally, hypoxia is predictive of tumour progression towards a malignant phenotype which correlates with a worse prognosis for many different types of cancer [9, 10]. At a cellular level, hypoxia can be harmful and cause cell injury. In order to protect itself from the potentially harmful effects of reduction in oxygen levels, cells must adapt. Adaptation to hypoxia is coordinated by the master regulator hypoxia-inducible factor-1 (HIF-1), an oxygen sensitive transcriptional activator, which promotes cell survival under hypoxic conditions [11]. HIF-1 regulates multiple processes by transcriptional induction of genes involved in proliferation, angiogenesis and metabolism.

Immunohistochemical (IHC) studies have shown that even though proliferating cells are present in hypoxic regions, their number is small and markedly reduced compared to that in normoxic compartments [12-14]. HIF-1 can act to slow tumour proliferation by inhibiting cell growth [11]. Cell cycle progression is regulated primarily by the expression and activity of cyclins, cyclin-dependent kinases (CDKs), CDK activators, and CDK inhibitors [15]. HIF-1, by upregulating expression of the CDK inhibitors p21 and p27, induces cell cycle arrest in tumour cells [16]. HIF-1 also counteracts the action of c-MYC oncoprotein, which acts as a transcription factor to promote cell proliferation, to induce cell cycle arrest [17].

It is known that under hypoxic conditions HIF-1 also promotes changes in cell metabolism [18]. Oxidative phosphorylation, which is the predominant route of cellular energy production in normoxic cells, requires molecular oxygen. Under hypoxic conditions, the limited availability of oxygen forces cells to switch to using glycolysis in order to generate sufficient energy. HIF-1 facilitates this switch by activating the

glycolytic pathway, promoting the transcription of glucose transporters and glycolytic enzymes [18-22]. By increasing expression of pyruvate dehydrogenase kinase (PDK), HIF-1 also inhibits the flux of pyruvate towards mitochondrial metabolism.

Alterations in the signalling pathways that lead to deregulated control of cell proliferation frequently also *directly* affect energy metabolism in the absence of changes in oxygenation. Increased glucose consumption and production of lactic acid, even in the presence of oxygen, the so-called Warburg Effect, is a common feature of many solid tumours [23-26]. In order to sustain enhanced cell proliferation, glycolysis provides the supply of carbon skeletons that is required to generate new proteins, nucleotides and lipids needed for doubling of cell biomass [27]. In addition to oxygen sensing, HIF-1 acts as an effector of various signalling cascades which are dysregulated in cancer [28]. Hyperactivation of Ras, which coordinates the response to growth factors (Figure 1.1) activates HIF-1 [29], as does activation of its downstream effectors, the phosphatidylinositol 3-OH kinase (PI3K)/Akt and mitogen-activated protein kinase (MAPK) pathways [30-32]. In the absence of growth factor signalling, hematopoietic cells fail to express HIF-1 messenger ribonucleic acid (mRNA) suggesting that growth factor signalling is required for induction of HIF-1 under hypoxia [33].

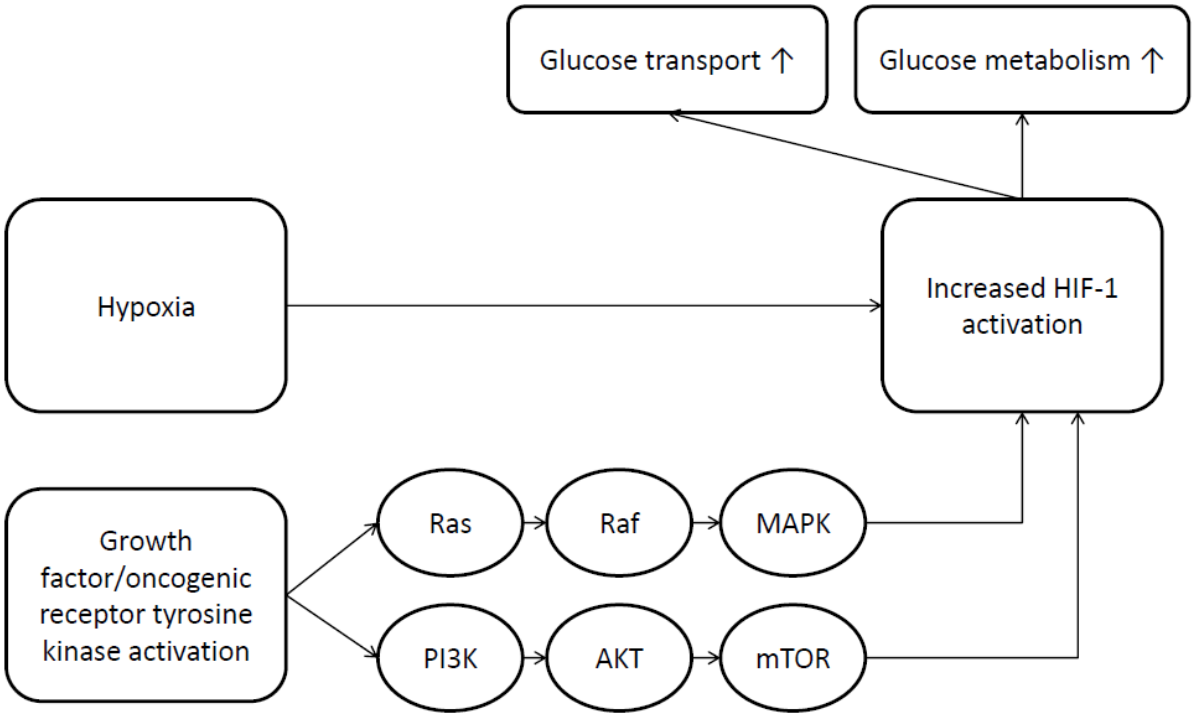


Figure 1.1: HIF-1 signalling responds to both hypoxia and growth factors to regulate glucose metabolism. When not degraded, HIF-1 can promote the expression of genes encoding glucose transporters and most enzymes of glycolysis.

Due to their clinical importance, hypoxia, proliferation and glycolysis are all individual therapeutic targets in their own right [10, 24, 25, 34-37]. However, the interlinking nature of these three tumour properties means that considering them in isolation runs the risk of missing information on the relationships between them. Only by studying the temporal changes in proliferation, hypoxia and glycolysis together, it will be possible to fully understand how these interrelated 'hallmarks' develop during tumour growth.

1.2 Multicellular tumour spheroids

Investigating the relationship between tumour growth, and the development of hypoxia and metabolic changes requires an appropriate experimental model. Figure 1.2 gives an overview of the available models. On first consideration, resected surgical specimens might seem best positioned to provide a complete picture of carcinogenesis. However, the majority of tumours are diagnosed after these properties have developed. Furthermore, they are likely to have developed a vascular network and invaded the host vascular system, which can confound analysis [38]. Hence, clinical samples do not allow for the systematic assessment of metabolic and physiological changes which occur during the earliest, avascular stages of tumour formation.

Preclinical models, such as mice, offer the closest approximation to tumour growth in humans [39, 40]. However, the *in vivo* approach suffers from a combination of ethical and economic problems, such as provocation of the disease in mice and high costs [41]. Furthermore, when using preclinical models, one is faced with the inability to separate the effects of the molecular tumour microenvironment from the heterogeneous vascular network of the host [42]. Thus, results from *in vivo* studies can be difficult to analyze quantitatively.

Conventional *in vitro* monolayer studies are highly manipulable and relatively inexpensive in comparison to *in vivo* studies. Monolayers are widely used to study the effects of hypoxia on proliferation and metabolism, by altering the atmospheric O_2 [16, 43-45]. However, it is impossible to form physiologically relevant gradients in oxygen in a two-dimensional (2D) environment. The multicellular tumour spheroid (TS) model offers a unique experimental bridge between conventional two-dimensional monolayer

cultures and *in vivo* models such as xenografts. TS are three-dimensional (3D) aggregates of tumour cells that are cultured *in vitro*. Although more time-consuming to initiate than monolayer cultures, TSs reproduce crucial tumour characteristics, such as histological organization and growth patterns.

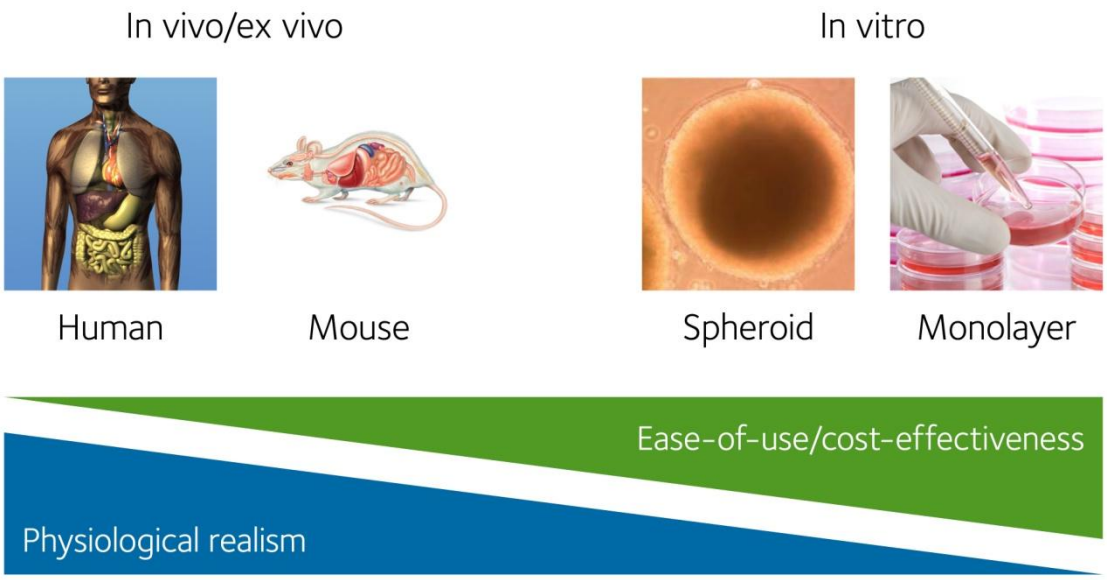


Figure 1.2: Overview of the available experimental models. Physiological realism is reduced in monolayer culture which is the cheapest experimental model. Spheroid culture is less expensive than using animal models, such as mice, and better at reproducing the tumour microenvironment than monolayer culture *in vitro*.

Diffusion processes play a crucial role in the growth and development of different cell phenotypes in both *in vivo* tumours and *in vitro* TSs. As a TS grows, proliferating cells located in its inner region naturally become hypoxic. The diffusion of oxygen and other nutrients, such as glucose, limits TS growth and leads to the development of a necrotic inner core. Thus, when attempting to replicate *in vitro* the hypoxic environment detected in many solid tumours, the TS model does not require the artificial maintenance of different oxygen tensions that is required in monolayer cultures. Instead, regions of hypoxia and necrosis emerge as a consequence of limitations in the supply of nutrients to interior cells. In contrast, a monolayer culture is an unsuitable model for reproducing

tumour growth, as in this model all cells are equally exposed to oxygen and other nutrients. In addition, the controlled environment in which TS are cultured simplifies the experimental process and allows for easy manipulation of the TS surroundings, which is technically difficult in *in vivo* xenografts. The microenvironment significantly influences intracellular signalling so that cells may be more radioresistant in 3D than in 2D systems. Mansbridge [46] showed that TSs had much less epidermal growth factor (EGF) receptors, which when activated stimulates cell division, than corresponding monolayers. The lower density of EGF receptors in TSs, which is not accompanied by a lower cell proliferation index, reflects a more efficient EGF autocrine loop in TS when compared to monolayer cultures. Hence, 2D systems may not be adequate to study the response of tumour cell growth to growth factors.

In summary, TSs reproduce the most fundamental characteristics of solid tumour growth and provide a model of intermediate complexity between *in vivo* tumours and traditional 2D tissue cultures. For these reasons, the TS system has been widely used in cancer research to investigate tumour growth, hypoxia and metabolism, and to test the efficacy of different anti-cancer drugs and radiotherapy protocols therapies [47-50]. Indeed, over the four decades since its introduction by Sutherland and co-workers [51], the TS culture has become a widespread *in vitro* model of tumour growth.

1.3 The value of mathematical modelling

Over the last few decades, a vast amount of experimental information on tumour growth, hypoxia and metabolism has been generated [10, 24, 25, 34-37]. It is a challenge to combine all of these disparate sources into a coherent description of the whole. As

cancer is a highly heterogeneous disease at both the genetic and phenotypic level, with large variation within individual tumours and between more than 100 known cancer types, the problem is very complex [52]. In order to organize large amounts of data regarding tumour metabolism and its multifactorial regulation through various genetic and biochemical pathways, a theoretical approach is highly desirable. Comparing results from different studies, whilst considering the complexity of multiscale biological processes, is difficult to achieve without a rigorous, systematic approach. Mathematical modelling enables progression beyond a verbal description of a process, enabling quantitative analysis and, crucially, prediction of the behaviour of the system. Mathematical models offer a formalised framework within which it is possible to consider changes in tumour growth at different scales: subcellular, cellular, tissue or organ. When parameterised with relevant data, mathematical models can be used to better describe, explain and predict the development of cancer.

Mathematical modelling can enable the reduction of the number of experiments, which may be expensive and time-consuming, by guiding experimental research to focus on the crucial information needed to characterise the phenomena of interest. Additionally, mathematical models can be used to efficiently analyse how system behaviour varies within a wide range of parameter values [53-56]. By comparing model outcomes, we can determine which parameter values are biologically realistic, whereas it may be impossible, or very costly, to estimate them experimentally. Simple, but carefully designed, experiments can provide the information needed to parameterise and validate mathematical models, which then can be used to generate novel hypotheses concerning the behaviour of a complex biological system [57, 58]. Although, ideally, experimental work and model development should go hand in hand, in practice it is rare for mathematical models and experimental studies to complement each other.

Due to insufficient numbers of relevant measurements, modellers must often resort to using parameter estimates from a range of sources. Yet these parameter values may have been estimated under very different culture conditions, using different cell lines, or measured using different techniques. Altered metabolism of cancer cells has been incorporated in several mathematical models that try to associate changes in nutrient consumption and dynamics of TS growth [53-56]. However, these models use parameters of questionable biological realism, and lack validation through quantitative comparison of model simulations with experimental results. Despite over 30 years of research, the fundamental question of how oxygen gradients are related to proliferation and how this relationship changes during tumour growth remains unanswered. Studies by Freyer and co-workers [58, 59] and Rodríguez-Enríquez et al. [35] have shown that larger TSs consume less oxygen than smaller TSs, but the exact mechanism of how oxygen availability impacts proliferation and, more generally, TS growth remains unknown.

In order to gain insights about the processes which regulate tumour growth *in vivo*, experimental and theoretical studies should complement and guide each other. Only then can we improve our understanding of tumour biology and design more efficient tumour treatment modalities. We therefore adopt an integrative approach in this thesis incorporating both experimental and modelling components.

1.4 The DLD-1 cell line

Over the last few decades a large number of human immortal cancer cell lines have been established for *in vitro* tissue cultures. In this thesis we use the DLD-1 cell line, derived

from a human colon adenocarcinoma cell line, as it is an exemplar of fast-growing tumour cells in terms of intrinsic metabolic and physiological characteristics [60]. The DLD-1 cell line has an activated copy of the K-Ras oncogene, which has been found in 45% of colorectal cancers [61] with oncogenic mutations of components of the Ras signalling pathway frequently found in all cancer types [62, 63]. For a more detailed characterisation of the DLD-1 cell line, please refer to Sarthy et al. [60] or Dexter et al. [64].

1.5 Thesis outline

The aim of this thesis is to characterise the development of DLD-1 TSs, focusing on the relationship between proliferation, hypoxia and metabolism. Whilst many studies concentrate on the precise mechanisms which link two or more of these tumour attributes, such as signalling pathways, we take a step back and look at how these relationships develop from a *macroscopic* perspective. To achieve this, we employ an interdisciplinary approach, using both experimental and theoretical methods. We summarise the interdependencies of Chapters 1 to 6 in Figure 1.3. Note that each chapter has a detailed introduction to the topics considered therein and possible routes for further work. A list of acronyms is provided on page 178.

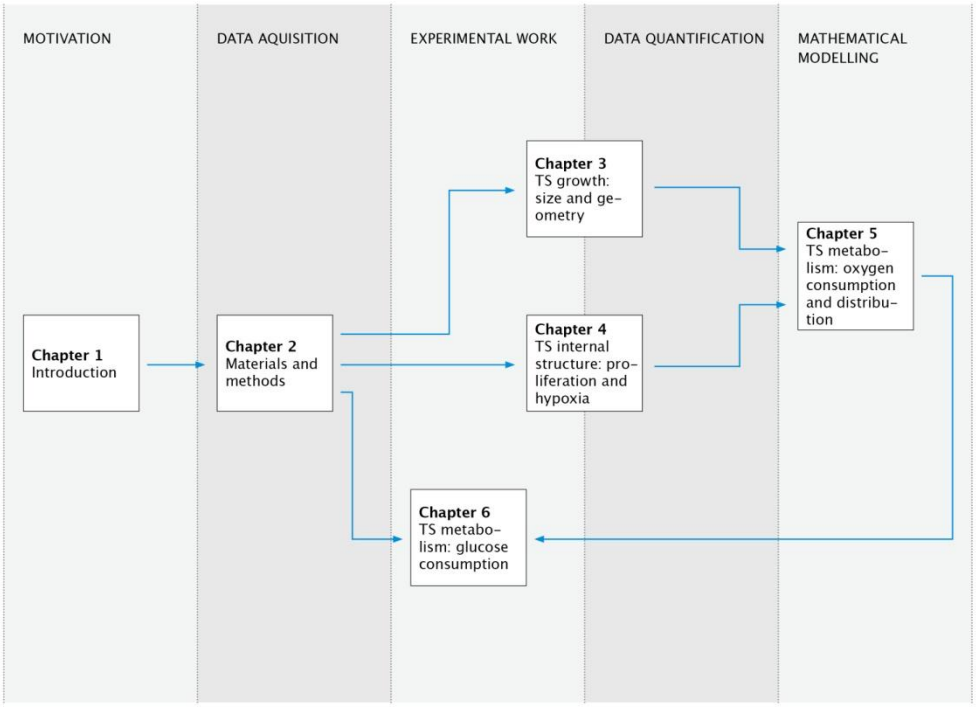


Figure 1.3: Diagrammatic representation of the links between Chapters 1 to 6 of this thesis, indicating the division of work.

In Chapter 2 we explain the experimental methods used to generate DLD-1 TSs and the laboratory techniques used to acquire the data discussed in Chapters 3, 4, 5 and 6.

In Chapter 3 we characterise changes in DLD-1 TS size and geometry during spheroid development. In order to determine changes in TS size, we develop an automated method of image analysis which provides a robust method for TS size assessment, in contrast to subjective techniques. Additionally, we examine and quantify changes in gross TS morphology during growth. We complete our description of DLD-1 TSs growth by fitting the most commonly used mathematical models to the data to assess which of the models captures the observed growth behaviour most accurately.

In Chapter 4, we extend the image analysis methods presented in Chapter 3 to develop a method to extract quantitative estimates of proliferation and hypoxia during

growth. These values are used to quantify changes in proliferation in response to hypoxia.

Although the impact of hypoxia on proliferation through HIF-1 is well understood, it is not clear whether changes in proliferation, in turn, have an effect on hypoxia. In Chapter 5, we investigate whether the spatial changes in proliferation observed in Chapter 4, have an impact on spheroid oxygenation, via oxygen consumption. As it is experimentally infeasible to measure oxygen consumption at all radial positions within a TS we resort to theoretical tools to investigate it. We use mathematical modelling in conjunction with the datasets generated in Chapters 3 and 4 to assess whether varying oxygen consumption according to proliferative status of the cells needs to be considered for prediction of spatial distribution of oxygen within TSs.

In Chapter 6 we return to an experimental approach and characterise the development of one of the best described features of cancer cells: the glycolytic phenotype. By analysing changes in key-regulatory glycolytic enzymes and the HIF-1 oxygen-regulated subunit, HIF-1α, we determine the bioenergetic changes that occur in DLD-1 TSs during growth.

Finally, in Chapter 7, we conclude with a summary of the major results presented in this thesis and discuss possible avenues for future work.

1.6 Statement of originality

Chapters 3, 4 and 6 are original work.

In Chapter 5 the developed model of oxygen distribution within TSs is based on the reviewed models of oxygen consumption within a TS that consider the steady-state

pO_2 distribution resulting from the balance between diffusion from the surrounding growth medium, described with Fick's laws, and a Michaelis-Menten description of oxygen consumption [53-56]. Originality is claimed for the implementation of this model with the selected parameter values and assessment to what extent it gives an accurate prediction of the experimental data obtained in Chapter 4. Originality is claimed for the extension of the simple model of oxygen transport and uptake by incorporation of more biological detail which is based on the experimental results of the fractions of proliferating and non-proliferating cell types in regions of normoxia, hypoxia and severe hypoxia obtained in Chapter 4.

Chapter 2 Materials and methods

In this chapter we describe the experimental methods used to generate the data presented in Chapters 3, 4 and 6 of this thesis. We describe the tissue culture techniques for DLD-1 TS generation and maintenance (Section 2.1) assessed in the context of changes in TS size and gross morphology in Chapter 3; immunofluorescent (IF) techniques used to detect hypoxia and proliferation (Section 2.5.3) which we investigate in Chapter 4; the metabolic assays used to assess the content of glucose and lactate in TS medium (Section 2.3); the enzymatic assays used to evaluate glycolytic enzyme activities (Section 2.4); the Western blots which we used to describe changes in content of key-regulatory glycolytic enzymes and HIF-1α (Section 2.6); IF techniques used to detect spatial distribution of hexokinase II (HKII) and lactate dehydrogenase V (LDHV) (Section 2.5.5) presented in Chapter 6.

2.1 Cell Culture

2.1.1 Cell line initiation and maintenance

The DLD-1 human colon adenocarcinoma cell line (obtained from Dr. Richard Callaghan, University of Oxford, UK) was used in this study. Characterization of the DLD-1 cell line can be found in Sarthy et al. [60] or Dexter et al. [64]. Cells were maintained as a monolayer in RPMI-1640 medium (with L-Glutamine and 25 mM Hepes) supplemented

with 10% fetal bovine serum (FBS) and penicillin (100 IU ml $^{-1}$)/streptomycin (100 mg ml^{-1}) (P/S), subsequently referred to as complete RPMI medium.

Subculture of cells was carried out in a bioMAT class II sterile laminar flow hood and maintained in a tissue culture incubator at 37^{o} C with 20% oxygen and 5% carbon dioxide (CO_2).

When initiating a new tissue culture cycle, cells were removed from liquid nitrogen storage and thawed in a water bath at 37^{o} C. After thawing, cells were diluted 1 in 5 volume of RPMI-1640 medium and seeded on a T25 cell flask. When cells reached confluency, the following standard splitting procedure was performed: RPMI medium was aspirated from the flask, cells were rinsed with sterile 1x phosphate buffered saline (PBS) and dissociated by adding 1 ml of 1 x 0.05% Trypsin- ethylenediaminetetraacetic acid (EDTA) (Gibco) diluted 1 in 10 in sterile 1x PBS. Cells were then diluted 1 in 5 volume of the complete RPMI-1640 medium and reseeded in a T75 or T25 flask. The subsequent reseedings were performed at the desired cell density needed for specific experiments.

2.1.2 Cell cryopreservation and storage

Cells were centrifuged at 3000 revolutions per minute (rpm) for 5 minutes (min) and the supernatant aspirated off. Subsequently, the cell pellet was resuspended in a complete RPMI medium supplemented with sterile-filtered 10% DMSO (Sigma Chemical Company) and 10% (FBS) 1 ml cell aliquots were transferred into cryovials. Vials were put in a Nalgene® Mr Frosty filled with 200ml isopropanol at room temperature, and placed for short-term storage at -80^{o} C. After 24 hours (h) cryopreserved cells were moved to long-term storage in liquid nitrogen.

2.1.3 Cell density measurement

The total number of viable cells was counted by using the NucleoCounter NC-100 (Chemometec). The method relies on DNA staining with propidium iodide (PI) which is immobilized in the measurement NucleoCassette. Prior to loading the samples into the cassette, cells are lysed with lysis buffer prepared by mixing Reagent A and Reagent B in 1:1 ratio. The lysis of cells before loading into the cassette allows for PI staining of free nuclei, therefore providing a total cell count. The non-viable cell number can be calculated by directly loading cells into the cassette as those cells are permeable to PI without treatment. Using the NucleoCounter method in assessment of cell number has been shown to generate more reproducible results than using traditional trypan blue/haemocytometer methods [65]. The NucleoCounter method reduces the intra- and inter-observer variation inevitably linked with conventional cell counting with trypan blue using haemocytometer.

2.2 TS preparation protocol

2.2.1 TS initiation and maintenance

24-well tissue culture plates were coated with liquefied 1% agarose (Sigma) in 1x PBS. After the agarose had set, exponentially growing DLD-1 cells were seeded at a density of 1.6×10^4 cells per well in 200 µl of complete RPMI medium. Subsequently, plates were incubated without disturbance at 37° C, 5% CO_2 for four days at constant humidity.

After four days the cells formed well-contained tumour spheres which were kept in culture for a maximum period of 20 days. For continuous culturing of TSs the whole amount of medium (200 µl) was refreshed every 48 h in each well.

2.2.2 TS homogenates

In order to evaluate glycolytic enzyme activities and expression, TSs were harvested from each well of the 24-well culture plate and transferred to a 1.5 ml sterile microtube. After collection, the TSs were washed with 0.5 ml 1x PBS for 5 min on the plate shaker and 1x PBS was removed. Subsequently, one 'complete mini protease inhibitor' tablet (Roche) was dissolved in 10 ml of 0.05 M tris (hydroxymethyl) aminomethane (Tris)-hydrogen chloride (HCl) (pH 8.0). 400 µl of the prepared solution was added to a microtube containing collected TSs. The TSs were homogenized with a plastic homogenizer and pressing syringe with a needle on the side of the eppendorf tube until total dissociation. Afterwards, 50 µl aliquots of TS homogenates were snap-frozen in liquid nitrogen and stored at -80^{o} C.

2.2.3 TS growth measurement

In order to dynamically monitor TS growth, images were acquired in 1280x1024 pixels and 24-bit format on an inverted Leica DM IRBE microscope, using Simple PCI Imaging Software, made by Hamamatsu. One hundred images of randomly selected TSs were taken were taken every 24 h for a period of 20 days, after which the TSs quickly disintegrated. The images of the TSs were obtained using a 10x magnification lens until day 12. After day 12, the TSs were too big to monitor changes in their size with this lens.

Therefore, it was replaced with a 4x magnification lens which was used to obtain images until the end of the culture period.

2.2.4 TS fixation and cryopreservation

TSs were harvested from each well of the 24-well culture plate and transferred to a 1.5 ml sterile microtube. After collection, the TSs were washed with 0.5 ml 1x PBS for 5 min on the plate shaker and 1x PBS was removed. Subsequently, the TSs were fixed by adding 0.5 ml freshly prepared paraformaldehyde (PFA) in 1x PBS to the eppendorf and incubated at 4^{o} C for 12 h. After fixation, PFA was removed. Then the TSs were washed with 0.5 ml 1x PBS for 30 min on the plate shaker and following that the 1x PBS rinse was removed. Following the wash with 1x PBS, 0.5 ml of freshly prepared 25% sucrose in 1x PBS was added to the eppendorf and TSs were cryopreserved at 4^{o} C for 12 h. After cryopreservation, 25% sucrose in 1x PBS was aspirated off and the TSs were moved to plastic molds where they were embedded in optimal cutting temperature compound (OCT). Bright 5040 microtome (Bright Instruments) was used to cut 10 µm sections which were then collected on microscope slides (VWR) and placed in a slide box. Prior to long-term storage, the collected microscope slides with the microtome TS cross-sections on them were air dried at 37^{o} C overnight. After that, samples were stored at -20^{o} C.

2.3 TS-based assays

Changes in glucose consumption and lactate production are an indirect indication of the elevated glycolysis that is typical for cancer cells [66]. In order to evaluate this, glucose

and lactate concentrations in the TS medium were measured throughout TS growth. Cell culture medium samples were collected from 24-well tissue culture plates (20 wells per sample). 1 ml aliquots of the collected supernatant were prepared and stored at -20^{o} C for later use.

2.3.1 Glucose concentration

Glucose concentration was measured using a proprietary assay kit (Cambridge Bioscience). The measured reaction relies on glucose oxidation in the tested and standard samples to generate a product that reacts with a dye to generate a colour (λ = 570 nm). The colour intensity obtained is proportional to the glucose concentration of the tested and standard samples.

For colorimetric glucose measurement, a standard curve of concentrations was created by adding an adequate volume of the glucose standard provided to a 96-well transparent, flat bottom tissue culture plate and adjusted to 50 µl/well with Glucose Assay Buffer for all standards. The glucose standard curve obtained was in the range from 0 to 10 nmol. 2 µl of each test sample, diluted 1/5 with water, was added to the 96-well plate in duplicate. 48 µl of Glucose Assay Buffer was added to all samples to make up the total volume to 50 µl/well. 50 µl of Glucose Reaction Mix, which consisted of 92% of Glucose Assay Buffer, 4% of Glucose Probe, and 4% of Glucose Enzyme Mix, was then added to all samples and standards and following that the 96-well plate was incubated at 37^{o} C for 30 min. After incubation, the absorbance was measured at 570 nm in a 96-well plate using a microplate reader (Tecan Infinite® 200 Pro) and the standard curve was plotted. Sample readings were then applied to the standard curve. Glucose concentrations of the test samples were then calculated using the following formula

$$C = 5\frac{Sa}{Sv}, \tag{2.1}$$

where *C* denotes glucose concentration of the test sample in nmol/µl, *Sa* represents sample amount (in nmol) from the standard curve, *Sv* is the sample volume (in µl) added into the sample wells and 5 accounts for sample dilution.

2.3.2 Lactate concentration

The Eton Bioscience L-lactate assay kit was used to determine lactate concentration in TS culture medium. For lactate measurement, a standard curve of concentrations (in the range from 0 mM to 5 mM) was created by adding 20 µl of the lactate standards provided to a 96-well transparent, flat bottom tissue culture plate. Then, after thawing, medium samples were diluted 1/5 with water in order to obtain a linear assay range. A pilot assay was used to optimize the best dilution factor for the test samples. Subsequently, 20 µl of the test samples were added to a 96-well plate in triplicates. 50 µl of Lactate Assay Solution, which was supplied in the kit, was added to all samples and standards. Afterwards, the 96-well plate was incubated at 37^{o} C for 30 min.

The theory of the lactate assay is based on enzymatic conversion of lactate and nicotinamide adenine dinucleotide (NAD+) to pyruvate and NADH by lactate dehydrogenase. The reaction is coupled with the reduction of the tetrazolium salt to formazan, which can be detected at 490 nm. The measured absorbance intensity of formazan formed is proportional to the lactate concentration of the tested and standard samples. After incubation, the reduction reaction was terminated by adding 50 µl of 0.5 M acetic acid per well to all samples and standards. Subsequently, the absorbance was measured at 490 nm using the microplate reader (Tecan Infinite® 200 Pro). Afterwards,

the data obtained from the standard curve were plotted and used to obtain the straight line equation which then was used to calculate the lactate concentration (in mM) in the samples. Finally, the results were multiplied by 5 in order to account for the dilution factor of the measured medium samples.

2.4 Enzyme activity protocols

2.4.1 Quantification of protein concentration

The Pierce® BCA Protein Assay Kit (Thermo Scientific) was used to calculate the total amount of protein present in the TS homogenates. Prior to measurement, all test samples were rapidly thawed and placed on ice. 2 mg/ml bovine serum albumin (BSA) standard, which was provided in the kit, was serially diluted with 1/12.5 (0.05 M Tris-HCl pH 8.0/water) to prepare standards in the range from 0 mg/ml to 2 mg/ml. A standard curve of concentrations was created by adding 25 µl of the prepared BCA standards to a 96-well transparent, flat bottom tissue culture plate in duplicate. Subsequently, the TS homogenate samples of unknown protein concentration were diluted 1/12.5 with water and added to the same 96-well plate. The reagent A (containing sodium bicarbonate, bicinchoninic acid and sodium tartrate in 0.1 M sodium hydroxide) and reagent B (containing 4% cupric sulfate) were combined in a ratio 50:1 to prepare the BCA Working Reagent. Then 200 µl of prepared BCA working reagent was added to each sample and standard on the 96-well plate. The plate was then incubated at 37^{o} C for 30 min.

The method of protein concentration assessment is based on the reduction of Cu^{2+} to Cu^{1+} by protein in an alkaline medium with the Cu^{1+} reagent which contains

bicinchoninic acid [67]. The product of this reaction forms an intense purple complex which increases proportionally with increasing protein concentrations in standard and tested samples.

After incubation, the absorbance was measured at 562 nm in a 96-well plate using the microplate reader (Tecan Infinite® 200 Pro). In order to calculate the actual protein concentration of test samples, the background value obtained from the blank glucose control was subtracted from all the test readings. Afterwards, the data obtained from the standard curve were plotted and used to obtain the straight line equation which was then used to estimate the protein concentration (in µg/µl). Finally, the results were multiplied by 12.5 in order to account for the dilution factor used during the assay and the actual protein concentration of the TS homogenates was determined.

2.4.2 Enzyme reaction components

The Michaelis-Menten model predicts that the velocity of a reaction is given by

$$f(C) = \frac{vC}{C + K}, \tag{2.2}$$

which increases roughly linearly with substrate concentration (*C*) when the substrate concentration is low and saturates when substrate concentration goes above the Michaelis constant (*K*) [68]. The calculation of maximal reaction velocity (*v*) and affinity constant (*K*) of the selected enzymes was performed prior to measuring enzyme activities in the TS homogenates, by using pure commercially-available enzymes. The Michaelis-Menten model will be explained in detail in the context of oxygen consumption in Section 5.1.

To measure selected enzyme activities, reactions were started by adding TS homogenate (0.1 mg total protein content) to a spectrophotometric cuvette filled with specified buffer components in a final volume of 1 ml. Depending on the measured assay, NAD(P)H oxidation or NAD(P) reduction was measured. NAD(P)H is a coenzyme of many glycolytic enzymes which absorbs UV light in its reduced, but not in its oxidised, form. $NADP^+$ differs from NAD^+ in the presence of an additional phosphate group on the 2' position of the ribose ring that carries the adenine moiety. LDHV, which utilises NADH as a substrate can be directly measured by following changes in ultraviolet (UV) absorbance as the reaction which they catalyse consumes the coenzyme at the same rate as the enzyme activity [69]. Activities of other glycolytic enzymes (HKII, phosphofructokinase-1 (PFK-1), and pyruvate kinase M2 (PKM2)) were measured using a coupled assay where the product of one reaction is used as a substrate of another reaction which uses NAD(P)H as a coenzyme and can be detected using spectrophotometric assays [69]. Hence, enzyme activity was estimated by measuring the change in absorbance at 340 nm in a Hitachi Model U-2010 spectrophotometer (Hitachi Instruments). In order to make sure that the reactions were measured at maximal enzyme activities, values determined for affinity constants were multiplied by a factor of 10 and used as optimal substrate concentrations in the adjusted assay conditions. The specific conditions for measurements of selected enzymes and monitored reactions are shown in Table 2.1.

Enzyme	Buffer components	Reaction monitored
HK II	0.05 M Tris-HCl (pH 8.0), 13.3 mM magnesium sulphate ($MgSO_4$), 0.55 mM adenosine-5'-triphosphate (ATP), 0.22 mM NADP, 20 mM glucose and 1.5 unit/ml glucose-6-phosphate dehydrogenase	NADP reduction
PFK-1	50 mM TRIS-HCL (pH 7.4), 5mM $MgSO_4$, 5mM ammonium sulfate, 0.5 mM fructose-6-phosphate, 0.1 mM ATP, 0.25 unit/ml NADH, 2.5 unit/ml trisephosphate isomerase, 1.49 unit/ml aldolase, 3.62 unit/ml alpha-glycerophosphate dehydrogenase	NADH oxidation
PKM2	0.05 M Imidazole-HCl (pH 7.6), 0.12 M potassium chloride, 0.062 M $MgS0_4$, 1.48 mM adenosine diphosphate (ADP), 0.218 mM NADH, 0.2 mg/ml LDHV and 3 mM phosphoenolpyruvate	NADH oxidation
LDHV	0.2 M Tris-HCl (pH 7.3), 0.218 mM NADH and 4 mM sodium pyruvate	NADH oxidation

Table 2.1: The conditions for measurements of the activities of HKII, PFK-1, PKM2 and LDHV. The monitored reactions were started by adding TS homogenate of 0.1 mg total protein content.

2.4.3 Enzyme activity calculations

In order to calculate enzyme activities from measured changes in absorbance/s the Beer-Lambert law was applied [70]:

$$\Delta A = \Delta \varepsilon c l, \tag{2.3}$$

where Δ denotes measured changes, A represents absorbance, ε is the molar absorption coefficient, which is a property of the NAD(P) and NAD(P)H reduced coenzymes at 340 nm wavelength equal to 6220 $M^{-1}cm^{-1}$, l is the length of the light-path in the spectrophotometer cuvette, which was equal to 5 mm and c is the concentration of the product formed. As Beer's law states that the concentration is proportional to

absorbance, enzyme activity can be calculated from the change in absorbance per unit of time. Hence, concentration of the product formed per min per mg of protein in TS homogenate sample (calculated as described in Section 2.4.1) gives the enzyme activity in units of µmol/min per mg of protein.

2.5 Immunofluorescence

Actively proliferating cells are identified in this study by using Ki-67, an endogenous marker of proliferation [37, 71]. Regions of hypoxia are identified using the IHC marker EF5 (2-(2-Nitro-1*H*-imidazol-1-yl)-*N*-(2,2,3,3,3-pentafluoropropyl)acetamide), which is reduced under hypoxic conditions [10, 72]. Hoescht 33342 stain is used to identify the location of all cell nuclei.

2.5.1 IHC markers description

EF5 is a 2-nitroimidazole which is a highly specific and widely used marker of hypoxia. As a bioreductive dye, EF5 covalently binds all viable hypoxic cells at a rate that is inversely proportional to tissue oxygen level [73, 74]. EF5 binding to hypoxic cells has been extensively studied *in vitro* and *in vivo* for more than 15 years and is currently used to detect hypoxia in solid tumours in clinical settings [75, 76]. Anti-EF5 monoclonal antibodies conjugated to the Cy3 fluorophore, which, upon excitation, gives the region of hypoxia an intense red colour were used in this study.

Ki-67 human nuclear antigen is the most classical histopathological marker of cell proliferation [77-79]. Ki-67 is expressed in proliferating cells but not in quiescent cells

[71]. A detailed cell cycle analysis of Ki-67 expression has shown that Ki-67 expression is restricted to late gap 1 (G1), DNA synthesis phase (S), gap 2 (G2) and mitosis (M) phases, and is absent in quiescent (G0) phase [71]. Increased Ki-67 expression is also related to poor metastasis-free survival and death [37].

HKII is a key glycolytic enzyme which catalyzes the first-step of the glycolytic pathway. HKII is greatly over-expressed in tumour cells [80, 81]. It is a cytoplasmic enzyme but the majority of HKII binds to transmembrane channels, called the voltage-dependent anion channels, which are located within the outer mitochondrial membrane [82]. Mitochondrial-bound HKII has access to ATP generated through aerobic respiration, thus it can initiate glycolysis independently of glycolytic ATP delivery. Furthermore, mitochondrial-bound HKII can inhibit apoptosis in some cells via inhibition of cytochrome *c* release [83, 84].

LDHV is another cytoplasmic enzyme which takes part in glucose metabolism. The LDHV catalyzes the conversion of pyruvate to lactate hence, the final reaction of anaerobic glucose metabolism [85]. In highly malignant and hypoxic carcinomas, the most prevalent is the LDHV isoform, which is absent from normal epithelia but extensively expressed in cancer cells and linked with tumour hypoxia and poor prognosis [85, 86].

The final marker used is Hoescht 33342, which is a bisbenzamide stain that dyes DNA. Hoescht can bind to any nucleic acid present but DNA strands rich in adenine and thymine increase its fluorescence [87]. In TSs, the rate of uptake of Hoescht is independent of cell type. Hoescht distribution is uniform throughout the TS cross-section and only dependent on stain delivery [88].

2.5.2 EF5 incubation

EF5 was a gift from Dr. Cameron J. Koch (University of Pennsylvania, Philadelphia, PA). For characterization of EF5 binding please refer to [73-75]. The EF5 was dissolved in PBS to obtain a 3 mM concentration. Then 20 µl of 3 mM stock was added to 180 µl of medium in each TS culture well to obtain the final concentration of 0.3 mM per TS. The TSs were incubated with EF5 for four h, which was optimal for adequate marker exposure. Following EF5 incubation, the TSs were harvested, washed with PBS, fixed, cryopreserved and cut as previously described.

2.5.3 Ki-67 and EF5 co-staining

Staining was performed using reagents from Perkin Elmer Tyramide Signal Amplification (TSA™) Plus Fluorescence Kit and Streptavidin/Biotin blocking kit from Vectashield. The selected IF method uses incorporated horseradish peroxidise (HRP) enzyme to catalyse the deposition of a fluorophore-labelled tyramide amplification reagent onto tissue sections that were previously blocked with proteins. The reaction results in deposition of fluorophore-labelled reagent in proximity of the immobilized HRP enzyme which allows for amplification of the signal and accurate detection of the selected antigen. The specific methods for IF protocol followed are shown in Table 2.2.

Step	Procedure	Incubation time
1. Slides thawing	Incubate at room temperature	5 min
2. Antigen retrieval	Place in a microwave oven in 10 mM sodium citrate with 0.05% Tween 20, pH 6.0	First 4 min at 300W, followed by 16 min at 80W
3. Wash	Immerse in 1x PBS	5 min
4. Suppression of endogenous peroxidases activity	Immerse in 0.3% freshly prepared H_2O_2 in 1x PBS	20 min
5. Wash	1x PBS	2 x 5 min
6. Endogenous biotin block	Incubate with streptavidin reagent (Vectashield) in the humidifying chamber	15 min
7. Wash	Immerse in 1x PBS	5 min
8. Endogenous Streptavidin block	Incubate with biotin (Vectashield) and incubated in a humidifying chamber	15 min
9. Wash	Immerse in 1x PBS	5 min
10. Blocking step	Incubate with TNB Blocking Buffer (0.1 M Tris-HCL pH 7.5, 0.15 M NaCl, 0.5% Blocking Reagent) (Perkin Elmer) in a humidifying chamber	45 min
11. Primary antibody (Ki-67)	Incubate with mouse anti-human Ki-67 primary antibody* (clone 2531, HCA053A, AbD Serotec) diluted in TNB blocking buffer at 1/100 dilution in a humidifying chamber at 4^o C	overnight at 4^o C
12. Wash	Immerse in 1x PBS	3 x 5 min
13. Secondary antibody (Ki-67)	Incubate with goat anti-mouse biotinylated antibody in a dilution of 1/500 in TNB Blocking Buffer and incubated in a humidifying chamber	30 min
14. Wash	Immerse in 1x PBS	3 x 5 min
15. Streptavidin-HRP	Incubate with streptavidin-HRP Reagent (provided in Perkin Elmer kit) in a dilution of 1/200 in TNB Blocking Buffer and incubated in a humidifying chamber	30 min
16. Wash	Immerse in 1x PBS	2 x 5 min

17. Detection of Ki-67	TSA-fluorescein isothiocyanate (FITC) conjugated amplification reagent in a dilution 1/100 in Amplification Diluent and incubated in a humidifying chamber	5 min
18. Wash	Immerse in 1x PBS	1 x 5 min
19. Fixation	Incubate with 4% PFA under the fume hood	20 min
20. Wash	1x PBS	3 x 5 min
21. Blocking	Incubate with TNB Blocking Buffer in a humidifying chamber	30 min
22. Wash	Immerse in 1x PBS supplemented with 0.3% Tween 20	5 min
23. Primary antibody (EF5)	Incubate with Cy3-conjugated anti-EF5 monoclonal antibodies ELK3-51 (75 µg/mL, obtained from Dr. Cameron J. Koch)**	overnight incubation at 4^{o} C
24. Wash	Immerse in ice-cold 1x PBS supplemented with 0.3% Tween 20	3 x 5 min
25. Wash	Immerse in 1x PBS	1 x PBS
26. Nuclear staining	Incubate with Hoechst 33342 (Sigma) in a dilution 1/1000 in 1x PBS in a humidifying chamber	5 min
27. Wash	Ice-cold 0.3% Tween 20 in 1x PBS for 45 min***	3 x 45 min
28. Mounting sections	One drop of Vectashield® mounting medium and coverslips placed on slides.	

Table 2.2: IF techniques used in Ki-67 and EF5 co-staining of slides containing TS cross-sections prepared as described in Section 2.2.4. *To assess nonspecific antibody binding one slide ('negative control') was incubated in TNB blocking buffer only. **To assess nonspecific antibody binding one slide was treated with a 'competed stain' consisting of 75 µg/ml antibody mixed with 0.5 mM EF5 to block specific sites. *** The slide incubated with competed stain was firstly rinsed five times in ice-cold 0.3% Tween 20 in 1x PBS containing 0.25 mM EF5 for 2 min and placed in ice-cold 0.3% Tween 20 in 1x PBS containing 0.25 mM EF5 for 35 min. Following initial washes, the slide with competed stain was incubated in ice-cold 0.3% Tween 20 in 1x PBS containing 0.25 mM EF5 for 45 min. Finally, the slide with competed stain was rinsed once with ice-cold 0.3% Tween 20 in 1x PBS for 45 min.

Images were obtained using an epifluorescent microscope (Leica).

2.5.4 Image analysis pre-processing

Emission of the fluorescent marker of hypoxia, EF5-Cy3, was written to the red (R) channel of the RGB picture: emission of Ki-67-FITC, which was used to detect cell proliferation, was written to the green (G) channel of the RGB picture and emission of Hoescht 33342, which was used to detect cell nuclei, was written to the blue (B) channel of the RGB picture. Each channel was separated from the RGB picture (as shown in Figure 2.1) to allow further analysis.

The background autofluorescence, which was defined as the intensity value taken by the largest number of pixels in the image, and the unspecific contribution of either EF5-Cy3 dye (calculated by the average staining intensity in the image with 'competed stain') or Ki-67-FITC dye (calculated by the average staining intensity in the image with 'negative control') were subtracted from the generated image.

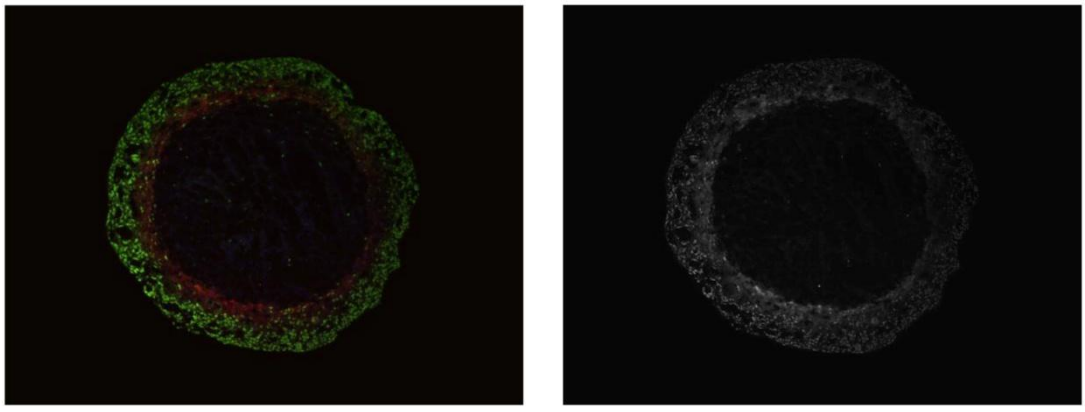


Figure 2.1: Pre-processing a TS image used to separate the R channel from the input RGB image. A) A sample epifluorescent image of TS taken at day 16 of growth. B) The R channel separated from the image.

2.5.5 HKII and LDHV detection

In order to detect the spatial distribution of HKII and LDHV, staining was performed using reagents from Perkin Elmer Tyramide Signal Amplification (TSA™) Biotin System Kit and Streptavidin/Biotin blocking kit from Vectashield. Steps 1-9 were the same as used in the case of Ki-67 and EF5 co-staining explained in Table 2.2. The remaining steps of the IF procedure used to detect HKII and LDHV distribution in the TS cross-sections are listed in Table 2.3.

Step	Procedure	Incubation time
10. Signal enhancement	Incubate with Image-it FX Signal Enhancer (Invitrogen) in a humidifying chamber	30 min
11. Wash	Immerse in 1x PBS	5 min
12. Blocking	Incubate with TNB Blocking Buffer (0.1 M Tris-HCL pH 7.5, 0.15 M NaCl, 0.5% Blocking Reagent) (Perkin Elmer) in a humidifying chamber at room temperature	45 min
13. Primary antibody	Incubation with primary antibody* diluted in TNB Blocking Buffer in a humidifying chamber	overnight incubation at 4º C
14. Wash	Immerse in 1x PBS	2 x 5 min
15. Secondary antibody	Incubate with secondary biotinylated antibody in a dilution 1/500 in TNB Blocking Buffer in a humidifying chamber	30 min
16. Wash	Immerse in 1x PBS	3 x 5 min
17. Streptavidin-Horseradish Peroxidase	Incubate with Streptavidin-Horseradish Peroxidase (SA-HRP) Reagent (provided in Perkin Elmer kit) in a dilution of 1/200 in TNB Blocking Buffer in a humidifying chamber	30 min
18. Wash	Immerse in 1x PBS	3 x 5 min
19. Biotinyl tyramide	Incubation with Biotinyl tyramide reagent in a dilution of 1/100 in Amplification Diluent (both reagents were provided in Perkin Elmer kit) in a humidifying chamber	30 min
20. Wash	Immerse in 1x PBS	2 x 5 min
21. Streptavidin-fluorophore	Incubation with Streptavidin–fluorophore conjugated reagent in a dilution 1/250 in TNB Blocking Buffer in a humidifying chamber	30 min
22. Wash	Immerse in 1x PBS	2 x 5 min
23. Nuclear staining	Incubate with Hoechst 33342 (Sigma) in a dilution 1/1000 in 1x PBS in a humidifying chamber	5 min
24. Wash	Immerse in 1x PBS	3 x 5 min
25. Mounting sections	One drop of Vectashield® mounting medium and coverslips placed on slides	

Table 2.3: IF techniques used in HKII and LDHV staining of slides containing TS cross-sections prepared as described in Section 2.2.4. *For HKII detection primary antibody (Cell Signalling, Rabbit, C64G5) was diluted 1/50 in TNB Blocking Buffer whereas for LDHV detection primary antibody (Cell Signalling, Rabbit, C4B4) was diluted 1/200 in TNB Blocking Buffer.

Images were obtained using an epifluorescent microscope (Leica).

2.6 Western blots

2.6.1 Sample preparation

The TS homogenate samples prepared as described in Section 2.2.2 were thawed and the total amount of protein in the samples was determined by using Pierce® BCA Protein Assay Kit (Thermo Scientific) as described previously. The volume of the sample was equal to 20 µl and it was prepared as follows: the calculated volume of TS homogenate which corresponded to 5 µg of protein was added to the eppendorf tube, followed by 1 mM DTT, RunBlue LDS Sample Buffer (Expedeon) that contributed to 25% of the total sample volume and water to make up the remaining sample volume. Subsequently, samples were denatured at 70^{o} C for 10 min and then subjected to fast spin in the centrifuge.

2.6.2 Gel electrophoresis

10 µl of the prepared protein sample was loaded onto a gel and separated by sodium dodecyl sulphate-polyacrylamide gel electrophoresis (SDS-PAGE). 17-well RunBlue® Pre-cast gels (Expedeon) of various acrylamide concentrations (4-12% and 4-20% gradient for lower molecular weight protein detection, such as LDHV) were used. Before use, gels were washed with distilled water and placed into a Novex mini-cell tank (Invitrogen) that was filled with SDS running buffer, supplied by RunBlue® (Expedeon) and composed of 2-5% trycine, 2-4% tris-hydroxymethylaminomethane, 0.1-2.5% sodium dodecyl sulphate, 0.002-0.5% sodium bisulfate. Prior to use, the RunBlue® SDS running buffer was diluted 1

in 20 with distilled water. 10 µl of precision plus protein™ standards (Bio-Rad) was loaded to the first well on the gel, which was followed by other prepared protein samples using loading tips. After loading all of the samples the gel was run for 1 h at 150V.

2.6.3 Blotting protocol

Following protein separation by gel electrophoresis, the protein samples were transferred from the gel onto a 48 cm^2 polyvinylidene fluoride (PVDF) transfer membrane (Immobilon™ from Millipore). Firstly, the PVDF membrane was activated by immersion for 5 min in 100% methanol. During this activation, two sheets of Whatman paper and several sponges were soaked in freshly prepared transfer buffer composed of 25 mM Tris, 192 mM glycine, 20% methanol and 0.1% SDS. Subsequently, the membrane was placed on the gel and both were sandwiched between two sheets of Whatman paper, surrounded with sponges and inserted into a XCell II™ blot module (Invitrogen) which was filled with transfer buffer. Transfer was performed at 30V for 1 h 15 min.

After proteins were transferred to a PVDF membrane, the membrane was immersed in 5% milk TBS-T (prepared by dissolving Marvel skimmed milk powder in Tris-buffered saline supplemented with 0.1% Tween-20) and placed on a shaker for 1 h at room temperature. After blocking, the membrane was moved to a falcon tube and incubated with primary antibody diluted in 5% milk TBS-T overnight at 4^{o} C on a tube roller (SRT6, Stuart Equipment). The primary antibodies used are listed in Table 2.4, along with the concentrations used.

Following incubation with primary antibody, the membrane was washed three times with TBS-T for 5 min. Subsequently, the membrane was incubated with secondary

antibody diluted in 5% milk TBS-T at room temperature on a tube roller (SRT6, Stuart Equipment) for 1 h. After incubation with secondary antibody, the membrane was washed three times with TBS-T for 5 min and was ready for development.

2.6.4 Membrane development

Depending on the primary antibody used, the membrane was developed by using either Amersham™ enhanced chemiluminescence ECL or ECL+ kit (GE healthcare). ECL and ECL+ Advance Protein Detection systems are based on chemiluminescence technology. Briefly, the principle of this system relies on reactions catalyzed by HRP enzyme which is conjugated to the secondary antibody that is attached to the specific antigen present on the PVDF membrane that needs to be detected. The ECL+ kit consists of a lumingen PS-3 acridan substrate, which is converted to an acridinium ester intermediate when catalyzed by HRP. The ester intermediate reacts with peroxide in alkaline conditions and emits light, which can be detected by film. The ECL+ kit includes Solution A (substrate solution containing Tris buffer) and Solution B (acridan substrate solution in dioxane and ethanol). The two solutions were mixed in a 40:1 ratio. Then the membrane was soaked in the prepared ECL reagent for 1 min, protected from light by using an autoradiography cassette (Fisher), exposed to film (Fuji) and developed using a XoGraph processor (XoGraph Imaging Systems).

The ECL kit is based on the same chemiluorescence principle as the ECL+ kit and detection of the reaction that is catalyzed by HRP. ELC Advance Solution A (containing Tris buffer in 3.2% ethanol) and ECL Advance Solution B (proprietary substrate in Tris buffer) were mixed in a ratio of 1:1. When the two solutions were mixed, the membrane

was soaked in the prepared solution and developed as described previously using ECL+ kit.

Protein name	Company (order #)	Species	Dilution of primary antibody	Dilution of secondary antibody	Polyacrylamide gel used
β-actin	Insight Biotechnology (sc-1615)	Mouse	1/10,000	1/10,000	4-12%
HIF-1 α	Milipore (MAB5382)	Mouse	1/500	1/5000	4-12%
HKII	Cell Signalling (C64G5)	Rabbit	1/1000	1/5000	4-12%
PFK-1	Santa Cruz (sc-166722)	Mouse	1/250	1/5000	4-12%
PKM2	Abcam (ab6191)	Goat	1/2000	1/5000	4-20%
LDHV	Cell Signalling (C4B4)	Rabbit	1/1000	1/5000	4-20%

Table 2.4: Details of primary antibodies and dilutions of primary and secondary antibodies used for Western blots.

We used the techniques described in this chapter to generate the results we present in Chapter 3, where we investigate changes in TS size and gross morphology prepared as described in Sections 2.1-2.2, Chapter 4 where we analyze changes in hypoxia and cell proliferation in TS cross-sections generated using IF methods described in Section 2.5, and Chapter 6 where we show the results of changes TS metabolism measured as described in Sections 2.3-2.4 and Section 2.6.

Chapter 3 Changes in TS size and morphology during culture

It is widely accepted that TSs more accurately reproduce the microenvironment of an avascular tumour than standard monolayer cultures [89, 90]. However, the most common experimental assessment of a TS's size is conducted manually, which is both time-consuming and not reproducible between researchers. Thus, in this chapter we develop an automated method of image analysis to quantitatively characterize changes in TS size and gross morphology. We use this method to analyse a total of 2000 images of DLD-1 TSs, taken every 24 hours, throughout the entire period of growth.

3.1 Introduction

Monitoring the growth of tumours is important on several accounts. In the first instance, the intrinsic rate of growth is a key indicator of tumour malignancy [91, 92]. Secondly, knowing whether a tumour is growing slowly or fast can impact upon treatment planning, as tumour growth rate affects the outcome to anticancer therapies [91]. Finally, being able to accurately determine changes in growth is crucial to determine the success of therapy.

In the clinic, the major method of determining the response to therapy in tumours is by measuring the change in lesion size [93, 94]. In this context, size is determined as the longest measured diameter of a tumour, as taken from images obtained using computerized tomography (CT) or magnetic resonance imaging (MRI) [92,

95]. The RECIST measurement, which denotes Response Evaluation Criteria In Solid Tumors, is used in the majority of clinical trials to measure response to therapy [94, 96, 97]. The gross morphology of a tumour, though less widely measured, can also be an indication of invasive cancer phenotype and metastatic cell potential [98]: malignant colorectal polyps usually have a distinct fractal geometry characterized by irregular boundaries, in contrast to benign polyps that are characterized by smooth boundaries [99].

Prior to human studies, preclinical investigations are essential in order to compare and contrast different therapies. However, when using *in vivo* preclinical models it is difficult to investigate the effects of therapy on growth in a causal capacity due to the problem of distinguishing between the effects of confounding factors.

In vitro tumour models, which minimise outside interactions, enable the investigation of tumour cell proliferation under closely monitored conditions and allow for studying an easily identifiable response to a given treatment. The traditionally-used 2D monolayer culture provides an attractive alternative to preclinical models. Proliferation of tumour cells in a monolayer can be quickly and easily calculated by trypsinizing cells and evaluating cell number using any number of standard methods, including trypan blue and haemocytometer [65]. Alternatively, the growth rate may be evaluated by measuring DNA synthesis, using flow cytometry and bromodeoxyuridine (BrdU) [100]. However, tumour cells in a monolayer exist in an environment highly dissimilar to the *in vivo* situation. *In vivo*, access to nutrients is limited by distance to the nearest vascular supply. For this reason, growth in monolayer culture may overestimate the growth of *in vivo* tumours and pharmacological alteration of growth in monolayer culture is likely to overestimate drug efficacy in *in vivo* tumours.

In contrast to conventional monolayer studies, cultivation of TSs restores tumour-like architecture, together with morphological and functional features, of a solid tumour. With increasing size, TSs exhibit nutrient and proliferation gradients from the periphery towards the TS centre, naturally developing hypoxic regions, which are associated with increased drug resistance. In preclinical investigations, TSs are widely used to predict tumour response to chemotherapy and radiotherapy and provide an invaluable system for testing the actions of new therapies [47-50].

In the TS model, response to therapy is primarily assessed through changes in size during growth. Monazzam et al. [49] measured changes in size in response to various chemotherapeutic drugs using breast cancer cell line MCF-7 TS. The authors showed that, over the period of 7 days, most drugs resulted in a reduction or even regression of the TS size. In another study, the impact on MCF-7 TS size of another anti-cancer drug, mitomycin C, was evaluated by Zhang et al. [101]. The authors showed that size of the MCF-7 TSs was reduced with an increase in exposure time. Changes in DLD-1 TSs size in response to various organic and platinum(II)-based anticancer drugs was evaluated by Hall et al. [102]. The authors showed that all the organic and platinum-based cytotoxic agents produced, to varying degrees, either a retardation or reduction in DLD-1 TS size.

In general, evaluation of TS size is a common method to determine the effectiveness of an anti-cancer therapy. Chemotherapy induced changes in cell metabolism have to be translated into an anti-tumoural action, such as growth inhibition, for a drug to be selected for further testing.

3.1.1 Assessment of TS size

The most common experimental evaluation of a TS's size, is by measuring two-orthogonal diameters and taking their geometric mean [35, 103-109]. The schematic representation of this method is shown in Figure 3.1.

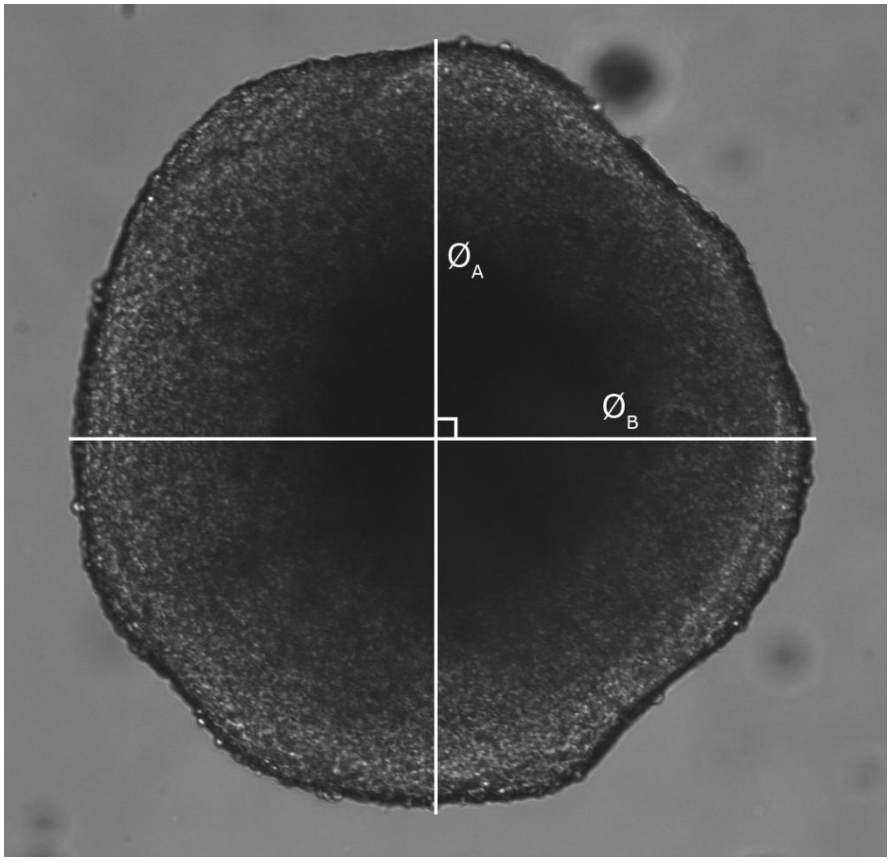


Figure 3.1: Schematic representation of the conventional method of a TS's size evaluation based on manual orthogonal diameters (Ø).

The geometric mean, *G*, of two-orthogonal diameters of the TS, denoted in Figure 3.1, $\varnothing_A$ and $\varnothing_B$, is defined by

$$G = \sqrt{\varnothing_A \varnothing_B}\,. \tag{3.1}$$

The methods of diameter (Ø) assessment vary, from the crudest evaluation 'by eye' using the in-built microscope graticule, to more advanced methods using simple software to manually estimate diameters with a calibrated ruler. The manually-evaluated

orthogonal diameters are then used to calculate the TS volume *V* under the assumption that the TS is exactly spherical, using the formula

$$V = \frac{4}{3}\pi\left(\frac{\emptyset}{2}\right)^3. \quad (3.2)$$

This type of manual assessment can be time consuming and imprecise, especially when the TS boundary is irregular.

Alternative, more rapid, methods of TS size assessment rely on acquiring microscope images of TSs photographed while they are in culture. A simple method of acquiring TS images was proposed by Kim and Forbes [110], who manually fitted ellipses to TS boundaries and averaged the lengths of the major and minor axes to calculate the mean diameters. The authors then used these as an indicator of changes in TS size in response to HIF-1 knockdown.

More advanced methods of image analysis remove the manual component of analysis and enable automatic calculation of TS cross-sectional area, from which TS volume is then approximated. The advantage of automation is removal of user 'bias', where the user adds their own potentially-incorrect bias, and also inter-user variability. For example, Kelm et al. [111] used the software package ImageJ (a widely-used image processing program, which is freely available to download from http://rsb.info.nih.gov/ij/) to calculate TS cross-sectional area and cross-sectional perimeter in TS images. In order to analyze TS shape, which, when irregular, can result in false over- or under- estimation of TS size, the authors evaluated sphericity *γ*. For a TS with computed cross-sectional area *A* and perimeter *P*, sphericity is defined as the ratio of the diameter of a circle with area *A* to the diameter of a circle perimeter P, hence is given by

$$\gamma = \frac{\pi\sqrt{\frac{4A}{\pi}}}{P}. \quad (3.3)$$

In the case of a perfectly spherical TS, we have $\gamma = 1$. Calculation of sphericity allows for further correction of the TS volume calculated from cross-sectional area by a more realistic TS shape factor.

In other work, Monazzam et al. [112] developed a Matlab program to analyze TS images automatically. Their method relies upon automatic delineation of a TS in the image, and involves integration of the total number of pixels enclosed within the TS cross-sectional area, and from this an approximation of the TS volume, under the assumption that the TSs are perfectly spherical. However, the method introduced by Monazzam et al. [112] lacks any analysis of TS shape, which would reveal whether the author's primary assumption that the TS is exactly spherical is valid.

3.1.2 Characterising TS growth

The quantitative description of TS growth has been a major focus of theoretical biology for over four decades. In 1982 Landry et al. [113] described the characteristic growth pattern of TSs based on experimental observations from TS studies, by dividing it into three distinct phases. The description of growth proposed by the authors has become the most widely used assessment criterion for predicting TS growth behavior in theoretical studies. The first phase describes the initial period of growth, which is typified by clumping of individual cells and the formation of cell aggregates, leading to exponential growth. When a certain volume is reached, the distribution of cells within the TS changes, resulting in the formation of a quiescent region in the centre of the TS that is surrounded by proliferating cells on the outside rim [114]. Changes in the proportions of proliferating and quiescent cells lead to a decrease in the growth rate from an exponential to a linear expansion in TS diameter. Physical constraints, such as a

gradual reduction in surface area to volume ratio as proposed nearly 40 years ago by Folkman and Hochberg [115], result in a reduction in TS growth rate. The authors suggested that TSs reach a critical size, after which growth stops, due to there being insufficient surface area for the TS to remove catabolites and absorb nutrients. The metabolic constraints were found to result in slowing of the TS growth rate by Freyer and Sutherland [58, 116], who showed that the maximum volume attained by a TS is correlated with the onset of necrosis, and on glucose and oxygen concentration in the surrounding medium. This defines the intermediate phase of TS growth [114]. In the final phase, the growth rate decreases and the 3D aggregate reaches a maximum size when its volumetric expansion halts [113].

Various theoretical approaches have been developed to describe avascular solid tumour growth, based on the TS model. A comprehensive recent review of the most significant publications in this field is provided by Roose et al. [117].

The simplest approach to describing the growth of TSs is to assume an exponential growth, i.e. a constant cellular doubling time [118]. Exponential growth can be used to describe the early stages of tumour growth, when nutrients are unlimited and tumour cells proliferate rapidly [118]. According to the exponential growth model, the tumour volume *N* grows according to the ordinary differential equation (ODE)

$$\frac{dN}{dt} = rN, \tag{3.4}$$

where *t* represents time and *r* is the linear growth rate. The exponential model predicts that the tumour volume can increase indefinitely and the growth rate of a tumour is proportional to its volume.

The analytic solution to equation (3.4) satisfying the initial condition $N(0) = N_0$ is given by [119]

$$N(t) = N_0 e^{rt} \, . \tag{3.5}$$

TS doubling time, the period that is required for a TS to double in mass, is a parameter derived from the tumour growth rate, which was introduced by Collins et al. in 1956 [120]. The linear growth rate is commonly used for prognostic purposes to quantify the therapeutic and environmental effects of different conditions or treatment modalities [121-126]. It is used in clinical radiotherapy to aid therapeutic decisions and patient screening [127]. Although doubling time is a representative estimate only for the exponential growth phase of tumours it reflects the basic pattern of neoplastic proliferation [128].

The doubling time can be calculated from the best-fit linear growth rate according to the expression [129]

$$DT = \frac{\ln(2)}{r} , \tag{3.6}$$

where *DT* denotes doubling time, and *r* represents the linear growth rate of tumour cells.

It is not, in general, reasonable to assume that TS growth will continue exponentially. The exponential model does not describe the TS growth rate, which slows as the TS size increases. To account for the observed reduction in TS growth rate, resulting from a combination of physical and metabolic constraints, another parameter is used to describe kinetics of tumour growth, the carrying capacity, K_c. Biologically, this means that tumours in a living organism, or TSs in culture, reach a maximum volume. These volumetric growth parameters can be estimated by fitting experimental data to the logistic and Gompertz growth models.

3.1.3 Logistic and Gompertz models of TS growth kinetics

The logistic and Gompertz models are classical growth models that have been applied to various biological processes. TS growth has been shown to follow Gompertzian or logistic kinetics in many studies [59, 116, 129, 130]. Both models predict an initial exponential growth phase, followed by a continuous deceleration from the initial point of observation. We show typical solutions to the logistic and Gompertz models in Figure 3.2.

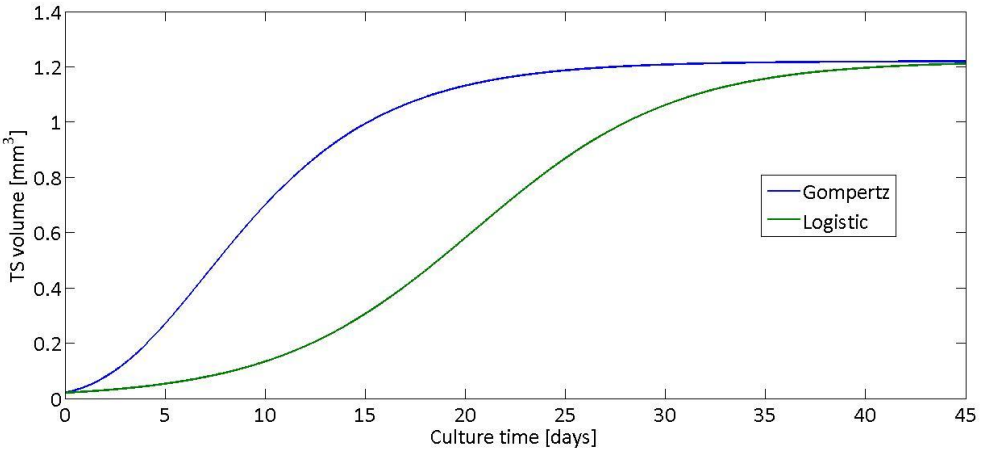


Figure 3.2: Solutions to the Gompertz and logistic models of TS growth for the specified linear growth rate α of 0.2 day^{-1} and carrying capacity K_c of 1.22 mm^2.

The logistic model is one of the classical theoretical models of growth and was introduced by Verhulst in 1838 [131]. The logistic model has found various applications, including the growth of organisms and populations, the evolution of autocatalytic chemical reactions [132], and the dynamics of neural networks [133], as well as TS growth [134]. Verhulst proposed that such processes exhibit an initial exponential increase followed by a phase of increasing size leading to a saturation size. In its simplest form, the logistic model is given by the ODE [135]

$$\frac{dN}{dt} = rN\left(1 - \frac{N}{K_c}\right), \tag{3.7}$$

where *N* denotes TS volume, *t* represents time, *r* is the linear growth rate and K_c is the carrying capacity. The analytic solution to this equation [119] satisfying $N(0) = N_0$ is given by

$$N(t) = \frac{K_c N_0 e^{rt}}{K_c + N_0(e^{rt} - 1)}. \tag{3.8}$$

The logistic model predicts a gradual and slow increase in TS volume. K_c is gradually approached as *r* decreases linearly to finally decline to zero. Hence, the logistic model has equal periods of slow and fast growth and the growth curve that it predicts is symmetric around the point which marks a maximum growth rate.

Another influential model which is a simple, yet adequate, descriptor of various TS growth curves is the Gompertz model. The Gompertz model was proposed by Benjamin Gompertz in 1825, but to describe growth of decelerating tumours it was first successfully used by Laird [118]. The Gompertz equation has since been used to model a variety of cellular processes, including kinetics of enzymatic reactions, intensity of photosynthesis and growth of normal and malignant cells [136].

The Gompertz model provides an optimum fit to the majority of data on tumour growth. The ODE defining the Gompertz model [137] is given by

$$\frac{dN}{dt} = rN ln\left(\frac{K_c}{N}\right), \tag{3.9}$$

where *N* represents the tumour volume, *t* denotes time, *r* is the linear growth rate and K_c is the carrying capacity. The analytic solution to this equation [137] satisfying $N(0) = N_0$ is given by

$$N(t) = K_c\, e^{ln\left(\frac{N_0}{K_c}\right) e^{-rt}}. \quad (3.10)$$

The initial period of TS formation before the TS starts to expand at an exponential rate is shorter in tumours which follow Gompertzian kinetics than in those which can be described with the logistic model. The Gompertz model predicts a fast period of growth and an exponential decrease in growth rate as the tumour approaches its carrying capacity. Hence, the Gompertz model has a shorter period of fast growth.

Even though both the logistic and Gompertz models display saturated growth, illustrated by a sigmoidal shaped growth curve, as described above, the way that growth saturation is attained in both models varies significantly.

3.2 Aim of work

Changes in TS size are often used to assess the effect of different experimental conditions on growth. However, not understanding the pattern of TS growth may give rise to capturing information at a stage of growth which is not representative of the situation *in vivo*. Additionally, to allow for meaningful comparison between TSs treated with a new drug and untreated, a reproducible method of size and morphology evaluation must be used.

In this chapter therefore, we develop an automatic method to measure diameter, cross-sectional area and perimeter from bright-field images of TSs. Quantification of these three characteristics enables us to determine changes in TS size and gross morphology, providing further insight into TS development.

We then aim to determine which of the most commonly used mathematical models (exponential, logistic or Gompertz) best describes the growth of DLD-1 TSs.

3.3 Methods

We described the experimental protocol of DLD-1 TS generation and culture in detail in Chapter 2. In brief, every 24 h we collect 100 images of DLD-1 TS cross-sections while TSs are growing in culture for a period of 20 days.

3.3.1 Image acquisition

Images are acquired in 1280x1024 pixels and 24-bit format by Simple PCI Imaging Software, made by Hamamatsu, connected to an inverted Leica DM IRBE microscope. TS images are obtained using a 10x magnification lens until day 12. After day 12, the TSs are too large to monitor changes in their size with the 10x magnification lens. Thus, we replace the 10x magnification lens with a 4x magnification lens for the remaining period of TS culture.

3.3.2 Automated image analysis of TS growth

All acquired images represent a TS cross-section taken at the maximum TS diameter. We upload the TS images in a JPEG format into Matlab and analyze all the pixels in the image. Figure 3.3 summarises our image analysis method.

We develop a software program in Matlab which analyses all images automatically and sequentially. The same set of image analysis parameters is used throughout the entire data set.

In order to undertake the image analysis, various in-built Matlab functions are utilised to perform the following steps:

1. The 2D grayscale image (Figure 3.3A) is normalised (Figure 3.3B) and converted to a binary image (Figure 3.3C) by thresholding, using the subjectively chosen threshold intensity of 0.8. The output binary image thus has the value 1 (white) for all pixels in the input image with luminance greater than 0.8 and 0 (black) for all other pixels. In order to ensure accurate detection of TS boundaries, the threshold value was chosen to match the collected images.

2. In order to detect a fully closed TS region, any discontinuous regions are removed from the objects detected in the image, any 'holes' (areas of black pixels surrounded by white pixels) identified in these objects are filled in (Figure 3.3D).

3. As there are large areas of microscope stage clearly visible at 10x magnification, which merge with the borders of the image, an edge mask is created to remove these objects (Figure 3.3E).

4. It is assumed that the TS is the object with the largest cross-sectional area in the resulting image and that all the other objects identified represent small clusters of cells that failed to form TSs or are a result of cell shedding. All but the largest object are therefore removed from the image (Figure 3.3F).

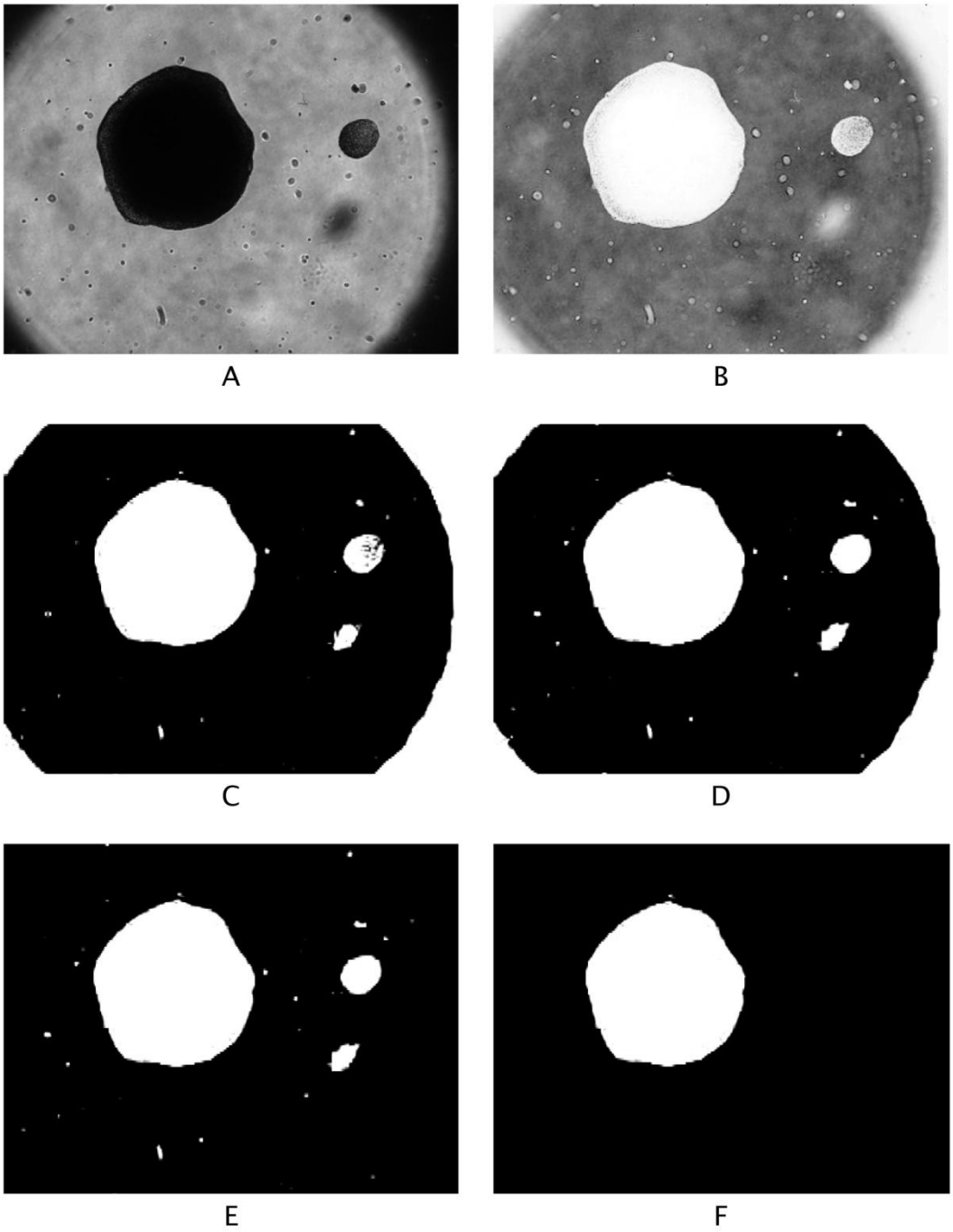


Figure 3.3: The automated method of TS image analysis. A) A sample image of a TS collected at day 15 of growth. B) The image is reduced to grayscale and normalised pixel values between 0 and 1. C) This greyscale image is then converted to a binary image based on a simple threshold (whose value was chosen by trial and error by analysing all images). D) Small holes identified in the objects detected in the image are filled in. E) The objects which are merged with the edges of the image are identified and removed. F) The TS is identified in the image under the assumption that the TS is the object with the largest cross-sectional area. All of the steps are performed automatically.

5. The following crude TS measures are automatically extracted:

1) Cross-sectional area, calculated by integrating the number of pixels enclosed within the TS;
2) Cross-sectional perimeter, calculated by integrating the number of adjoining pixels located around the border of the identified TS;
3) Major and minor axes, calculated by integrating the number of pixels of the major and minor axes of the ellipse that has the same normalised second central moments as the identified TS. The geometric mean of the minor and major axes length is the TS orthogonal diameter.

We use the extracted measures of TS size, including cross-sectional area, cross-sectional perimeter and major and minor axes length, to calculate the corresponding diameters under the simplifying assumption that a TS is perfectly spherical. This assumption has been made by several authors [103, 109, 138]. Table 3.1 explains our methods of diameter calculation from cross-sectional area, cross-sectional perimeter and major and minor axes length.

Measurement obtained:	Cross-sectional area (*A*)	Cross-sectional perimeter (*P*)	Major (*a*) and minor (*b*) axes length
Diameter (Ø) calculation:	$\emptyset = \sqrt{\frac{4A}{\pi}}$	$\emptyset = \frac{P}{\pi}$	$\emptyset = \sqrt{ab}$

Table 3.1: Methods of diameters (Ø) calculation under the assumption that a TS is exactly spherical.

In order to assess TS geometry the aspect ratio, which is commonly used to determine symmetry [54], is calculated. This quantity is defined by

$$Aspect\ ratio\ = \frac{b}{a}, \tag{3.11}$$

where the major axis length *a* is the longest axis of the TS which is perpendicular to the minor axis length *b*, which represents the shortest axis of the TS.

Additionally, we calculate the sphericity γ using the formula 3.3 provided in Section 3.1.1.

Finally, we convert the calculated TS characteristics from pixels to mm using the scale factors obtained by calculating the number of pixels corresponding to 1 mm length of the grid. As we used 10x and 4x magnifications in the experiment, we calculate two different scale factors. We use in-built Matlab functions to determine the mean, median and standard deviation of each of these measures.

3.4 Results

Figure 3.4 shows representative images of TSs, taken every 24 h for a period of 20 days. We observe that TSs increase in size on a daily basis throughout the entire period of TS culture time. Around days 10-11, the TS boundary becomes less regular than in the first few days of culture time. At days 19-20 we notice the first signs of TS disintegration, as an increasing number of cells are present in the medium around the TS and the TS boundary is most irregular. Even though the TSs show irregularities around their boundary, they maintain their macroscopic spherical geometry throughout all of the examined time points.

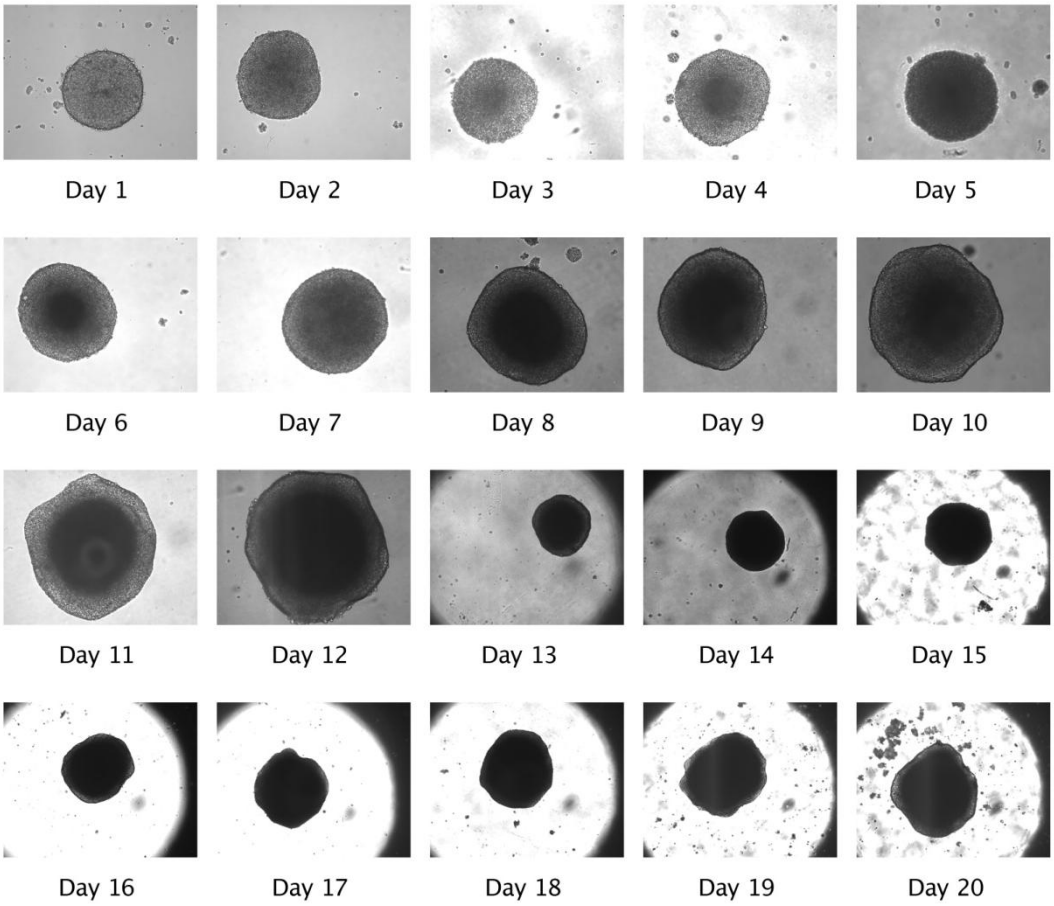


Figure 3.4: Representative images of TSs, photographed every 24 hours while the TSs are in culture for a period of 20 days. For continuous culturing the medium is refreshed from day 4 every 48 hours throughout the entire period of TS culture time. The TS images are obtained using a 10x magnification lens until day 12. After day 12, images are taken with a 4x magnification lens.

3.4.1.1 Comparison of cross-sectional diameters (Ø)

Figure 3.5 shows results of the estimates of cross-sectional Ø for the three approaches summarised in Table 3.1. Although all three methods suggest that Ø increases over culture time, the mean Ø calculated from the cross-sectional perimeter is significantly higher than both the mean orthogonal Ø or that calculated from the cross-sectional area time points, except for day 8 (1-way ANOVA was used to calculate significance for P value < 0.05). The mean Øs calculated either from cross-sectional area or mean

orthogonal Ø were not statistically different from one another, (1-way ANOVA P value > 0.05) except at day 1 (P value < 0.05).

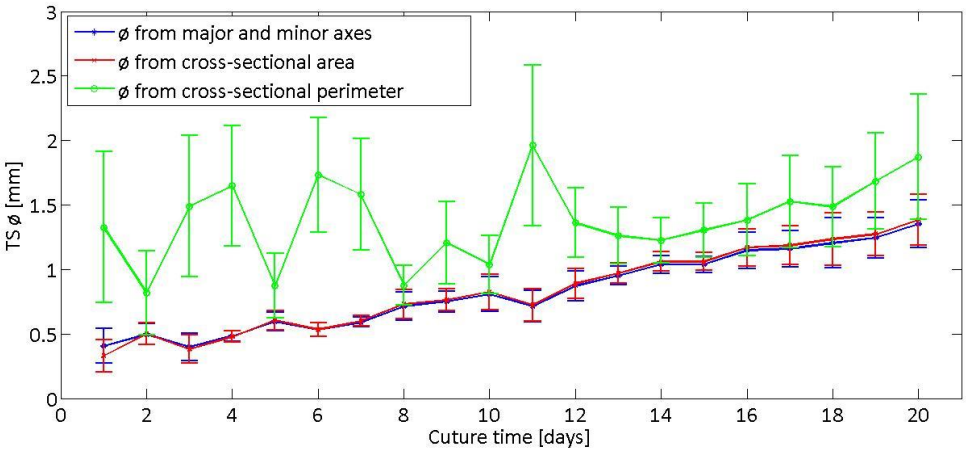


Figure 3.5: Changes in TS cross-sectional Ø (mm) calculated from cross-sectional area (blue), cross-sectional perimeter (green) and the geometric mean of minor and major axes length (red) obtained by analysis of images taken every 24 hours using the automated algorithm. Data represent the mean Øs of 100 randomly selected TSs where error bars denote standard deviation.

We find that the TS border is very irregular at the micro-scale. Thus, the Ø calculated from the cross-sectional perimeter overestimates the TS size as demonstrated using the exactly spherical tumour example in Figure 3.6. Hence, using cross-sectional perimeter as a feature to estimate TS Ø as required for volume evaluation would be inappropriate as the volume obtained would be falsely overestimated. Variation in the cross-sectional perimeter is lower following day 12 than in the early stages of TS development but remains consistently higher than Øs calculated from cross-sectional area and major and minor axes length. Presumably, following day 12, TS border irregularities are maintained but are less distinct at 4 x magnification than in the images of the TSs which were obtained using 10x magnification lens.

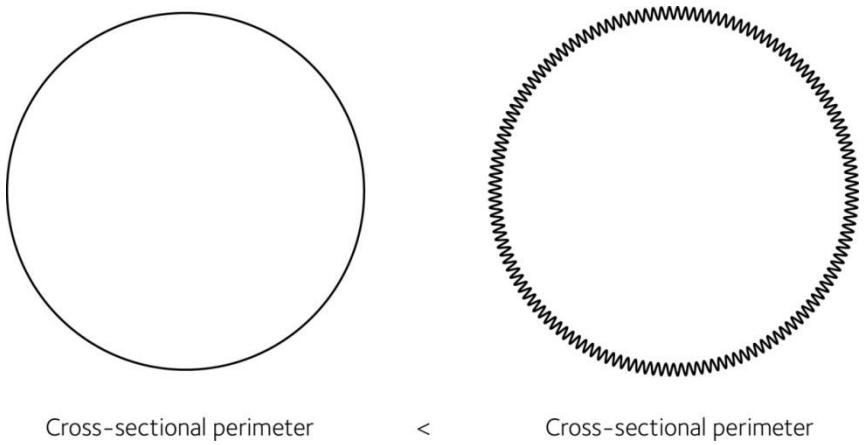


Figure 3.6: Our method of cross-sectional perimeter calculation relies on integrating the pixels located around the TS boundary. Thus, if a perfectly symmetrical TS had an irregular boundary, then the cross-sectional perimeter would be larger than the cross-sectional perimeter calculated if the TS had a smooth and regular boundary.

3.4.1.2 Aspect ratio and sphericity (*γ*) as methods of evaluation of TS shape

The assumption that TSs are perfectly spherical is made in the majority of theoretical studies (for example, Smallbone et al. [139], Horas et al. [140] and Wein [141]), which consider changes in TS size and histomorphology. The simplifying assumption that, at any given distance from the TS boundary cells have the same access to nutrients, such as oxygen, allows for division of a TS into concentrically arranged regions based on nutrient threshold, modelling of nutrient and metabolite transport and movement of cells within a TS [109, 142].

Kelm et al. [111] showed that HepG2 TSs derived from the hepatoma cell line cultured with the hanging drop method formed well-rounded TSs as evaluated by $\gamma > 0.70$ between days 10 and 16 of culture time.

Here, we use the extracted measures of TS size of major and minor axes length to characterize TS symmetry, and cross-sectional area and cross-sectional perimeter to calculate γ.

If a TS was a perfect sphere then the ratio of the two axes would be equal (giving the aspect ratio equal to 1). We show the results of our analysis in Figure 3.7. The mean aspect ratio is maintained relatively constant from day 5 (mean aspect ratio of 0.91) until the end of TS culture time, that is, for the majority of TS culture time points. Statistical analysis (1-way ANOVA was used to calculate significance for P value < 0.05) shows that changes in aspect ratio are significant between days 1-5 (P value <0.05) and not significant from day 5 onwards throughout the remaining culture time (P value > 0.05). Once again, the effect of magnification on determining sphericity has a major impact on the results here, as sphericity is constantly higher after magnification is switched from 10x to 4x.

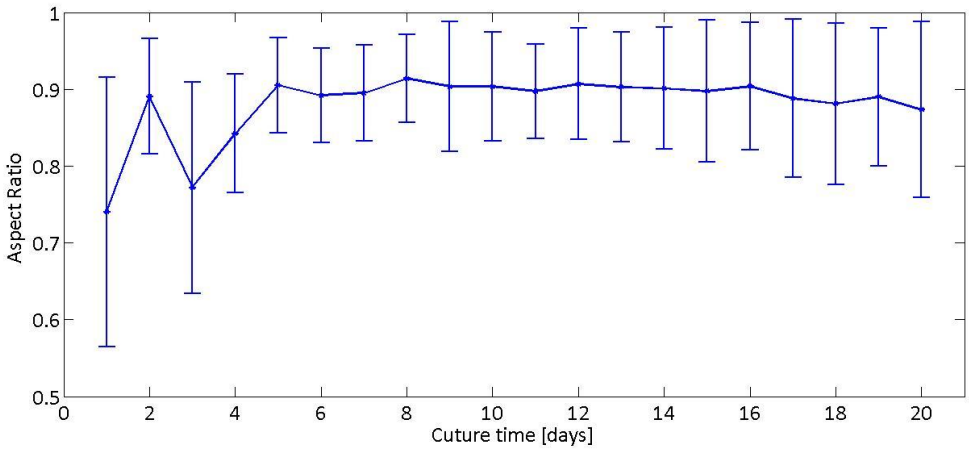


Figure 3.7: Changes in TS aspect ratio calculated by dividing the mean values of minor axes length by the mean values of major axes length (mm) obtained by analysis of TS images taken every 24 hours using the automated algorithm. Data represent the mean aspect ratio of 100 randomly selected TSs where error bars denote standard deviation.

Figure 3.8 shows changes in γ (derived from equation (3.3)) during TS growth. The γ increases to greater than 0.75 by day 8 (mean γ of 0.84) and remains stable until day 20 (mean γ of 0.76) except for day 11 (mean γ of 0.41). Statistical analysis (1-way ANOVA was used to calculate significance for P value < 0.05) reveals that changes in γ are significant between days 1-14 (P value <0.05) and not significant from day 14 onwards throughout the remaining culture time (P value > 0.05).

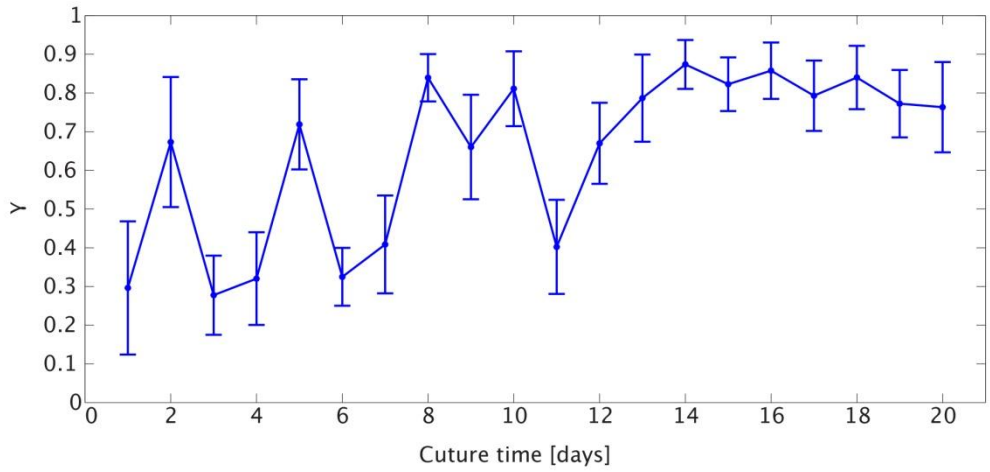


Figure 3.8: Changes in TS *γ* calculated by using cross-sectional area and cross-sectional perimeter obtained by analysis of TS images taken every 24 hours using the automated algorithm. Data represent the mean *γ* of 100 randomly selected TSs where error bars denote standard deviation.

3.4.1.3 Fitting the exponential, logistic and Gompertz models

In order to better understand TS growth dynamics we describe DLD-1 TS growth in terms of growth rate and carrying capacity, by performing a fit of the exponential, logistic and Gompertz equations to the measured TS volume, calculated from the cross-sectional area.

In Section 3.4.1.2, we showed that TSs were well-rounded but not perfectly spherical. Hence, in order to calculate TS volume we take into account the measured deviation from perfect sphericity. We estimate the corrected volume (*CV*) of TS using the formula [111]:

$$CV = \gamma \frac{4}{3}\pi\left(\frac{\emptyset}{2}\right)^3. \tag{3.12}$$

The results of fitting the logistic, Gompertz and exponential models to the corrected TS volume data are shown in Figure 3.9. The linear growth rate *r* and carrying

capacity, K_c, are estimated by minimizing the sum-squared error between the TS corrected volume data and each model and the results are listed in Table 3.2.

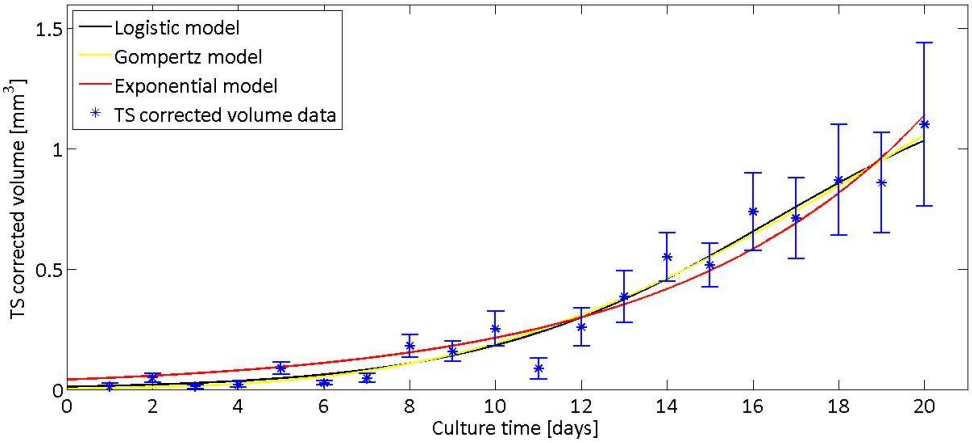


Figure 3.9: Changes in TS corrected volume (mm^3) determined using cross-sectional diameter calculated from area, under the assumption that the TS is a perfect sphere, obtained by analyzing TS images using the automated algorithm fitted with logistic, Gompertz, and exponential curves. Data represent mean TS volume of 100 randomly selected DLD-1 TSs where error bars denote standard deviation.

TS experimental data	Initial diameter (Ø)	0.27 mm
Exponential model	Initial diameter (Ø)	0.28 mm
	Linear growth rate (r)	0.30 day^{-1}
	Carrying capacity (K_c)	Not applicable
	Sum-squared error	0.11
Logistic model	Initial diameter (Ø)	0.28 mm
	Linear growth rate (r)	0.30 day^{-1}
	Carrying capacity (K_c) Ø	1.38 mm
	Sum-squared error	7.2 x 10^{-2}
Gompertz model	Initial diameter (Ø)	0.16 mm
	Linear growth rate (r)	0.09 day^{-1}
	Carrying capacity (K_c) Ø	1.81 mm
	Sum-squared error	7.4 x 10^{-2}

Table 3.2: The initial diameter Ø, linear growth rate r and carrying capacity, K_c, estimates calculated by minimizing the sum-squared error between the experimentally determined TS corrected volume data and each model. The sum-squared errors for the TS corrected volume and the predicted exponential, logistic and Gompertz curves are listed. For comparison, the experimentally determined diameter (Ø) measured at day 1 of TS growth is shown.

For the exponential model, the initial diameter Ø estimate is found to be a very close approximation of the TS Ø measured at the first day of growth. The linear growth

rate *r* estimated for the exponential model is equal to 0.30 day^{-1} which gives a doubling time of 2.34 days.

The linear growth rates and the doubling time estimates for the logistic and the Gompertz models are calculated under the assumption that the growth conditions are optimal and unlimited for both models. In order to reduce the experimental error associated with the measurement of the first data point, we find initial volume, from which we calculate Ø we present here, and initial linear growth rate estimates by fitting an exponential curve to the first five data points. The initial Ø estimate we find for the logistic model is a closer approximation to the experimental data than the initial Ø estimate we calculate for the Gompertz model.

For the logistic model, the estimated linear growth rate *r* is equal to 0.30 day^{-1}, which gives a doubling time of 2.34 days, and these values are similar to those obtained for these parameters estimated by fitting the exponential model. In contrast, the value of *r* estimated using the Gompertz model is equal to 0.09 day^{-1}, giving a doubling time of 7.26 days. There is a difference in the estimated carrying capacity sizes K_c which are calculated to be 1.39 mm^3 for the logistic model (equivalent to a Ø of 1.38 mm) and 3.09 mm^3 (equivalent to a Ø of 1.81 mm) for the Gompertz model.

Fitting the exponential model gives a worse fit to the experimental data than both logistic and Gompertz models. The fitting results are verified by calculating the sum-squared errors for experimentally determined TS volume and the predicted logistic (sum-squared error equal to 7.2×10^{-2}), Gompertz (sum-squared error equal to 7.4×10^{-2}) and exponential curves (sum-squared error equal to 0.11).

Overall, the logistic curve is best at recapitulating our experimental results in terms of exhibiting the lowest sum-squared error for experimentally determined TS volume and the predicted logistic curve. Hence, the results show that a carrying capacity of 1.39

mm^3, predicted by the logistic model (equivalent to a Ø of 1.38 mm), is not reached at day 20 (final TS volume equal to 1.10 mm^3 equivalent to a Ø of 1.28 mm), when the TSs start to disintegrate.

3.5 Discussion

In this chapter we developed an automated method of image analysis of TSs, which was used to characterise temporal changes in TS size, gross morphology and geometry during growth. Our method can be used to quantify cross-sectional area, cross-sectional perimeter and orthogonal diameter in any TS protocols where bright field microscopy images are recorded. We emphasise that our quantification method can be widely used in TS research as it is based on analysis of images obtained by standard microscopy available in most laboratories. The primary advantage of using our method of TS size and gross morphology evaluation over the traditional orthogonal diameter calculation using an in-built microscope graticule is that our method is objective, relying only on computation of the number of pixels which are included inside the identified TS boundary. Hence, our method of TS characterisation gives 100% reproducibility and removes the error associated with subjective measurement of orthogonal diameters.

From our results we concluded that the integrated cross-sectional area and mean orthogonal diameter calculated from the minor and major axes reflected changes in DLD-1 TS size equally well. DLD-1 aggregates formed compact TSs remarkably quickly within the first 24 hours of culture. We note that the observed TSs did not reach a plateau phase of growth and quickly disintegrated after reaching a maximal diameter around day 20. Fast disintegration of TSs after reaching a maximal diameter has previously been

reported in both DLD-1 and Hek-293 TSs. Although it has been attributed to large areas of necrosis, this suggestion has not been experimentally validated [35, 107].

Changing the microscope objective from a 10x to a 4x magnification lens at day 12 of TS culture resulted in a reduction in observed variability of the detected cross-sectional perimeter, which also affected calculation of sphericity. Presumably, this was caused by the fact that border irregularities became less distinct which resulted in an increase in cross-sectional perimeter from day 12 until the final day of TS culture. However, the cross-sectional perimeter overestimated TS size throughout the entire period of culture as revealed by analysis of diameters calculated by using the three methods explained in Table 3.1. Hence, we showed that the gross morphology of the TSs was very irregular on the microscale. In future however, we would recommend that TS size is determined using images taken at the same magnification to avoid this effect.

We note that we have not validated the accuracy of our method of TS size and morphology evaluation. To do this will require comparison with existing image analysis methods of TS size assessment (described in Section 3.1.1), but crucially requires the availability of a 'gold standard' or 'ground truth' measurement with which to compare all methods.

In Figure 3.7 we showed that the TS geometry remained unchanged from day 5 until the end of TS culture time. Moreover, the TSs were similar in shape, as assessed by analysis of calculated sphericity greater than 0.75, which was maintained for the majority of culture time points (Figure 3.8), to the well-rounded HepG2 TSs cultured using the hanging drop method generated by Kelm et al. [111]. The observed deviation in aspect ratio and sphericity from ideally spherical TSs is most likely a result of the experimental procedure and method of TS culture linked with agarose solidification and medium refreshment.

The primary characteristics that describe the dynamics of TS growth include growth rate and saturation size [143]. Hence, in this chapter we fitted the classical exponential, logistic and Gompertz models to volume data. The volume data were calculated by measurement of TS cross-sectional area corrected by sphericity in order to obtain objective estimates of initial growth rates and carrying capacities. Despite the fact that the TSs did not reach a carrying capacity, as predicted in the theoretical literature, the exponential model failed to recapitulate the experimental data as well as the logistic and the Gompertz models, suggesting that a carrying capacity would at some point be reached. The logistic model, which predicted larger linear growth rate than the Gompertz model, provided the best representation of the growth dynamics of the measured TS population. This difference may be explained by the different characteristics of the logistic and Gompertz equations: the latter underestimates the initial growth rates for growth curves that are sharply curving [116, 144]. We verified that the best-fit to the data was provided by the logistic model, which showed that TS growth was slow and gradual over the 20 day culture time period. It should be noted that slow growth relative to other cancers, is one of the primary characteristics of human colon cancers found *in vivo* hence, as the DLD-1 cell line is derived from human colon adenocarcinoma, our results are in agreement with what is clinically relevant [145]. The slow TS growth might be attributed to accumulation of non-proliferating cells which are less metabolically active as their proliferative counterparts. The reduction in the rate of proliferation of cells cultured as TSs as compared to monolayer culture has been observed by Lawlor et al. [146]. The authors showed that Ewing tumour (ET) cells (derived from pluripotent neural stem cells) have significantly higher rates of proliferation when cultured as monolayers than as TSs. In another study, Takagi et al.

[147] observed similar reduction in the rate of proliferation using the human prostate cancer cells (LNCaP) grown as TSs as compared to these cells grown as a monolayer.

TSs are intrinsically more resistant to virtually all anticancer cytotoxic drugs than conventional monolayer cultures. For example, EMT-6 and MDA-MB-231 human breast cancer cells when cultured as TSs, rapidly develop resistance to either cisplatin or 4-hydroperoxycyclophosphamide which is not observed when monolayer cell cultures are used [148]. In another study, Olive et al. [149] showed that TSs derived from Chinese hamster V79-171b lung fibroblasts were approximately 50-times more resistant to effective antiproliferative tumour agents, such as etoposide, than corresponding monolayer cultures. One mechanism contributing to multicellular drug resistance may be the reduced growth fractions of tumour cells, which are typically observed in TSs, compared to monolayer cell cultures [47]. It has been found that the CDK inhibitor p27 is up-regulated at the protein level in TSs, compared to the corresponding monolayers [150]. All of these studies suggest that TS are better at representing TS growth than monolayer which further supports the importance of our results. Additionally, the reported literature suggests that the accumulation to non-proliferating cell fraction in TSs is likely to be the primary cause for the DLD-1 TS slow growth pattern observed here.

We note that the carrying capacity predicted by the logistic model was not attained due to TS disintegration. This loss of TS integrity may be attributed to the development of large necrotic areas in the TS centre. Slow growth of DLD-1 TSs might be due to a large fraction of non-proliferating cells that are present within the TS from the start of culture. We will investigate these possibilities further in Chapter 4 by analysing TS internal composition. Hence, in the next chapter (Chapter 4) we shall continue our characterisation of DLD-1 TS growth and focus on cell proliferation and the development of hypoxia, which are established as the most crucial processes controlling growth. Thus,

we will analyse changes in the internal structure of DLD-1 TSs in order to gain insights into the observed growth behaviour.

Chapter 4 The relationship between hypoxia and cell proliferation in TS

In Chapter 3 we characterised changes in the size and *gross* morphology of DLD-1 TSs during their establishment and growth. In this chapter we consider the development of the *internal* structure of a TS and investigate the relationship between hypoxia and proliferation during TS growth.

During the early stages of TS growth, the TS is a cluster of proliferating cells. All cells within the TS will initially consume oxygen, but as the TS increases in size, access to oxygen becomes restricted for cells towards the centre of the TS. When the oxygen level drops below a threshold, the cells become hypoxic. Indeed, with increasing size, TSs exhibit an oxygen gradient from the periphery towards the TS centre. Proliferation also varies with distance from the TS surface. Many factors are known to affect tumour proliferation, including nutrient availability, cell signalling and cell death. Whilst it has been shown that presence of hypoxia negatively correlates with proliferation, it is not known what is cause and what is consequence. Here, we consider the temporal development of hypoxia and cell proliferative behaviour in TS.

4.1 Introduction

4.1.1 Tumour hypoxia

Hypoxia, a state of decreased or subnormal oxygen partial pressure (pO_2) which alters the normal function of tissues or cells [151], results from an imbalance between oxygen (O_2) supply and consumption. It can be chronic, acute, or a combination of both [152]. Chronic or 'diffusion limited' hypoxia arises from an irregular tumour microvasculature geometry, leading to increased diffusion distances between the nutritive blood vessels and the tumour cells. Acute, or 'perfusion-limited' hypoxia, results from spontaneous fluctuations in tumour blood flow, caused by the temporary closure of, or reduced flow in, certain vessels. Both types of hypoxia can be found in human tumours and are a common feature of human malignancies [153].

Hypoxia is associated with an aggressive, invasive phenotype, poor prognosis and resistance to both chemotherapy and radiotherapy [13, 76]. It can affect therapeutic outcome by inducing changes in the proteome and genome of neoplastic cells that promote survival and malignant progression [13, 76, 152].

Oxygen deficiency influences the major intracellular pathways involved in cell proliferation, cell cycle progression, apoptosis and cell adhesion. Hypoxia elicits a number of *compensatory responses,* which lead to the induction of multiple genes which promote oxygen supply and support anaerobic energy production. Overviews of the cellular processes inhibited at specific pO_2 levels were given by Höckel et al. [151] and Vaupel et al. [152].

4.1.2 The cellular response to hypoxia is coordinated by HIF-1

HIF-1 is a key modulator of the cellular response to hypoxia and controls multiple physiological and biological changes. HIF-1 is a heterodimeric protein made of alpha (α) and beta (β) subunits with the HIF-1α subunit acting as an oxygen sensor. A schematic representation of the regulation of HIF-1α by oxygen concentration is shown in Figure 4.1. HIF-1α is synthesised at a high rate under both hypoxic and normoxic conditions; however, under normoxic conditions it is almost immediately degraded. First, proline hydroxylase enzymes oxidize proline residues on HIF-1α. Next, the von Hippel–Lindau tumour suppressor protein (pVHL) binds to hydroxylated HIF-1α and activates a complex of proteins that mark it by ubiquitination for degradation in the proteasome. In contrast, in hypoxic conditions proline hydroxylases are inactive and unable to oxidize HIF-1α proline residues and pVHL cannot bind to and ubiquitinate HIF-1α. Consequently, HIF-1α can bind with HIF-1β and stable HIF-1 then binds *cis*-regulatory elements to activate hypoxia-inducible genes [154, 155].

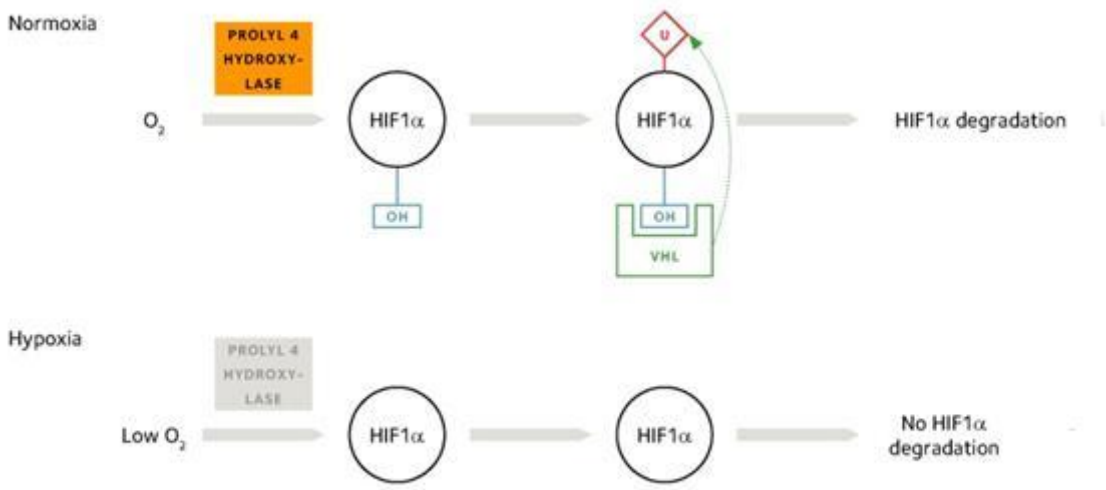


Figure 4.1: Schematic representation of the degradation of HIF-1 in normoxia. As HIF-1 is degraded in normoxia and detected in hypoxia it can be used to identify hypoxic tumour regions.

Aebersold et al. [156] and Birner et al. [157] showed that there is a direct causal relationship between hypoxia and cancer progression through increased HIF-1 expression. Patients with cervical or endometrial cancers where high levels of HIF-1 expression were detected had poorer outcomes [157]. IHC staining methods to identify HIF-1 expression in oropharyngeal squamous cell carcinoma biopsies showed that HIF-1 staining was concentrated in the viable hypoxic cells surrounding necrotic tissue [156]. This observation suggests that HIF-1 is present only in hypoxic cells and can be used as a marker of hypoxia. However, one-third of the examined oropharyngeal squamous cell carcinoma biopsies showed staining throughout the entire tissue, even in normoxic cells located in the proximity of blood vessels [156]. Hence, although HIF-1 expression is increased in hypoxic conditions, oxygen-independent mechanisms can also induce HIF-1 expression. This is discussed further in Section 4.1.3.1.

4.1.3 Hypoxia and proliferation

4.1.3.1 Hypoxia and proliferation are negatively correlated

Studies in several human tumour cell lines (including WiDr adenocarcinoma of the colon, SiHa, a squamous cell carcinoma of the uterine cervix, and DU-145, a prostate carcinoma) grown as xenografts suggested that the populations of proliferating and hypoxic cells were distinct [158]. However, further experiments confirmed that hypoxia and proliferation can overlap. *In vitro* studies have shown that elongation of the G1-phase, or G1 arrest in the cell cycle, can be detected below a threshold of 0.2 – 1 mmHg, which is significantly lower than the level below which we detect radiobiological hypoxia (below 10 mmHg) [159, 160]. An IHC study by Varia et al. [161] indicated a partial spatial overlap of tumour hypoxia and proliferation in cervical carcinoma samples obtained from ten patients. Another study, by Ljungkvist et al. [162] in xenograft lines of human head-and-neck squamous cell carcinoma showed that there was a significant number of proliferating cells, although reduced in comparison to normoxic regions, present in the hypoxic compartment.

The above studies suggest an inverse, though not mutually exclusive, relationship between hypoxia and proliferation [13, 14, 163]. It has also been suggested that brief exposure to hypoxia may not affect cell proliferation at all. In PC-3 prostate cancer cells, exposure to acute hypoxia (1% oxygen for less than 6 h) did not affect cell proliferation, but instead increased cancer aggressiveness in terms of increased motility, clonogenic survival and invasive capacity, whereas exposure to chronic hypoxia (1% oxygen for more than 24 h) decreased cell proliferation and induced cell death [164].

A schematic representation of the contradicting effects of hypoxia on proliferation, summarising the findings discussed above, is presented in Figure 4.2.

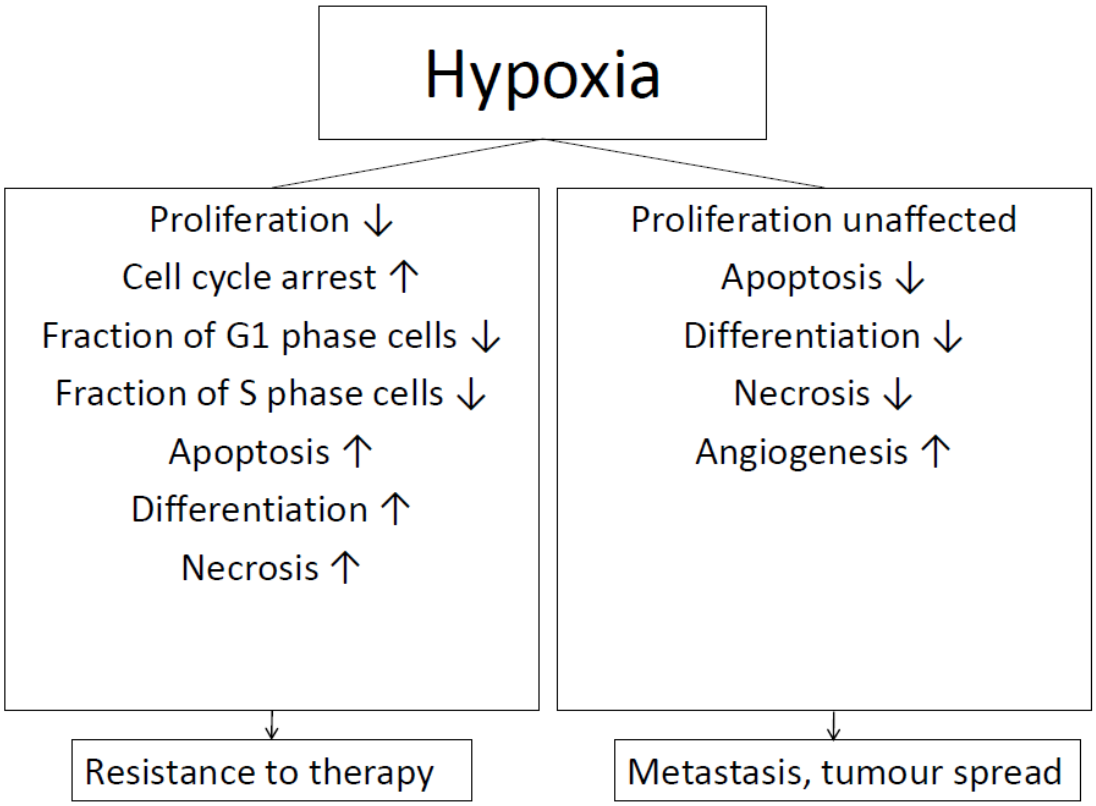


Figure 4.2: Two possible responses to hypoxia. The classical response results in reduction of proliferation and cassation of growth which leads to resistance to therapy and poor therapeutic response. On the contrary, hypoxia can maintain cell proliferation and favour an aggressive tumour phenotype and malignant progression which leads to poor long term prognosis.

A number of gene products that act as check point activators and prevent cell cycle progression if the DNA is damaged are essential in regulation of cell proliferation. The effects of oxygen deprivation resulted in 80-90% inhibition of DNA synthesis in ovarian carcinoma which was associated with an arrest of cell cycle progression (cells were incubated at pO_2 levels below 10 mmHg at increasing periods of hypoxia from 24 h to 48 h) [45].

Exposure of several solid tumour cell lines in monolayer studies to increasing periods of hypoxia (cells were incubated at pO_2 levels below 0.2 mmHg for 3 h, 24 h, and 72 h) demonstrated that hypoxia induces cell cycle arrest [44]. Many studies showed that hypoxia induces G1 phase arrest, resulting in a reduced fraction of active S-phase cells

[44, 159, 160, 165-167]. Hypoxia can block cell cycle progression through inhibition of DNA replication, retinoblastoma protein (pRb)-mediated cell cycle arrest in G1 phase and activation of an oxygen-sensitive restriction point in late G1 phase. All of these processes were thoroughly reviewed by Wouters et al. [153].

The adaptation to hypoxia through promotion of cell cycle arrest was proposed to be regulated by the action of HIF-1α by Goda et al. [16], who demonstrated that HIF-1 upregulates expression of the CDK inhibitors p21 and p27 in the two cell types: murine embryonic fibroblasts and splenic B lymphocytes cultured as monolayers. Loss of HIF-1α abolished hypoxia-induced growth and caused an increased progression into S-phase in hypoxic conditions in both cell lines. Gardner et al. [168] agreed that p27 regulates cell cycle arrest but suggested that this is independent of HIF-1 action. However, the role of p21 and p27 in hypoxia-induced growth arrest was not conclusive. Green et al. [167] showed that despite the fact that these CDK inhibitors are upregulated in hypoxia, they do not affect growth arrest in immortalized fibroblasts cultured as monolayers.

Although HIF-1α is a key regulator of the cellular response to hypoxia, it can be also activated in normoxia in response to a number of growth factors, where it can promote proliferation. A schematic diagram illustrating the impact of oncogene signalling on HIF-1α stabilization is shown in Figure 4.3.

A variety of signalling molecules involved in coordinating the response to extracellular growth factors are involved in HIF-1 activation. These include Ras, Src, PI3K and MAPK [29, 169-171]. Inhibition of the Ras pathway, which activates both the PI3K and MAPK pathways and stimulates proliferation and differentiation, was shown to down-regulate HIF-1α activity in glioblastoma cell lines [172, 173]. HIF-1α was found to be stabilized by p42/p44 MAPK, which regulates cell proliferation in response to extracellular growth factors [174]. PI3K activity is also increased in hypoxia [169]. It was

shown that mutations in the phosphoinositide phosphatase (PTEN), an inhibitor of the PI3K pathway, facilitate induction of HIF-1 regulated genes [175]. PTEN mutations have been found in many human cancers, suggesting that PTEN loss of function can provide a growth advantage by promoting HIF-1 mediated responses [176].

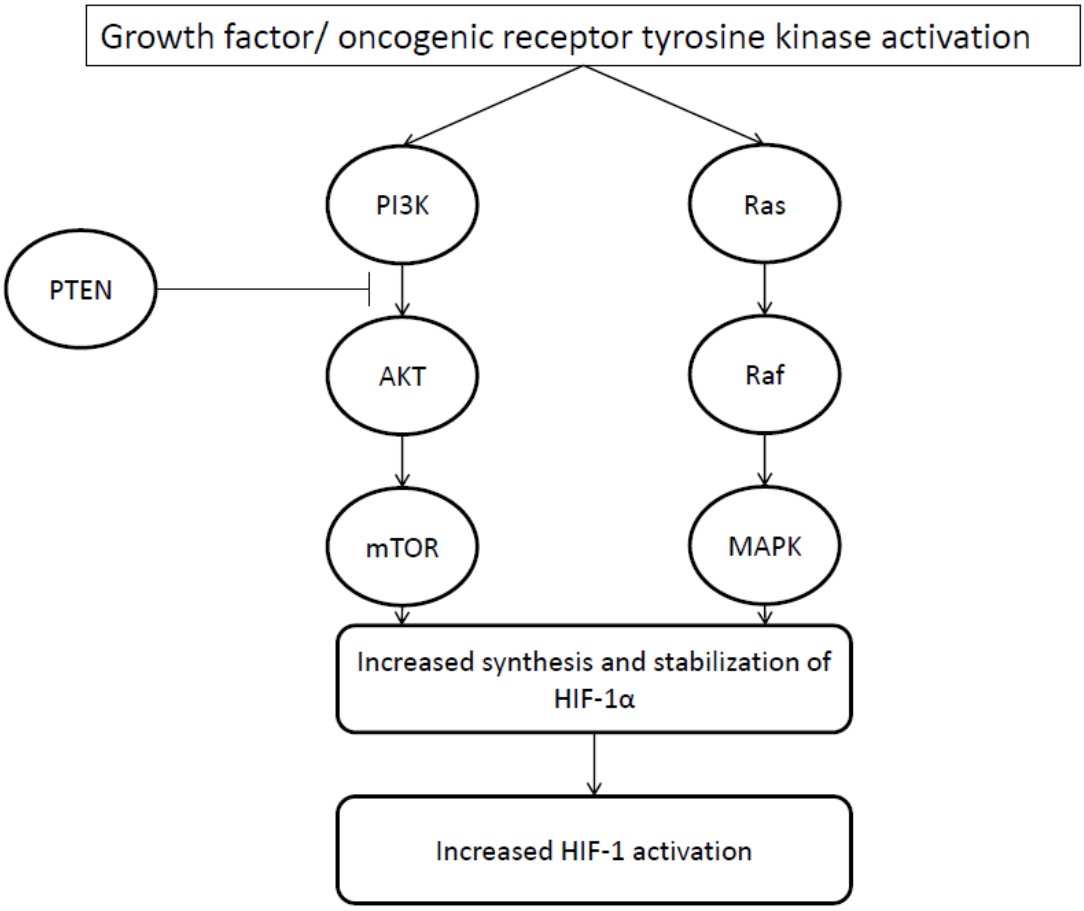


Figure 4.3: Schematic representation of signal transduction pathways involved in activation of HIF-1. Oncogenic and growth signalling can induce a HIF-1 response.

The mammalian target of rapamycin (mTOR), which is a downstream target of AKT, is also involved in the upregulation of HIF-1α. When mTOR is inhibited with rapamycin, accumulation of HIF-1α and HIF-1 modulated gene expression is inhibited in both normoxia and hypoxia [177]. Furthermore, HIF-1α induces production of growth factors, including transforming growth factor-β and platelet-derived growth factor [178, 179].

4.1.4 The TS as a desirable model for investigating the relationship between hypoxia and proliferation

Several experimental models, both *in vitro* and *in vivo*, are available to investigate the effect of hypoxia on proliferation. Standard *in vitro* methods, using cell monolayers or suspension cultures, are most common. These require the ability to control the environment in specifically-designed hypoxic chambers or incubators in which the oxygen concentration in the gas phase in held at a constant level [43]. However, the cellular homogeneity of monolayers is not realistic for solid tumours, which are composed of cells that differ in their proliferative status [180]. Additionally, cells cultured as a monolayer experience the same pO_2 across the entire population, which is not the case for avascular solid tumours where cells are exposed to different oxygen concentrations as the tumour grows.

TSs are composed of cells with varying proliferative status, resulting in a cellular heterogeneity that mimics the multiple cell phenotypes found in the majority of solid tumours. TSs present the most suitable *in vitro* model for studying the development of chronic hypoxia. As the TS grows, proliferating cells located in the inner region of the TS naturally become hypoxic, mimicking chronic hypoxia observed *in vivo*. In general, it has been observed that cells situated towards the centre of a TS, which are more hypoxic than those at the periphery, are less proliferative.

TSs have a long history as a model for investigating hypoxia, particularly with respect to resistance to therapy, as discussed in Section 3.1. LaRue et al. [181] demonstrated that the signals that regulate CDK expression differ in monolayer in comparison to TS culture. The observed reduction in growth fraction in TSs was attributed to up to a 15-fold upregulation of the p27 at the protein level in TSs,

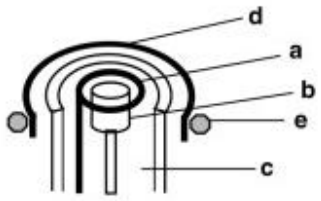
compared to corresponding monolayers [150]. Differential expression of other CDKs with respect to their location within EMT6 (mouse mammary tumour cell line) and MEL28 (human melanoma cell line) derived TSs was found by LaRue et al. [182]. The authors [182] showed that p21waf1/cip1, a cell cycle inhibitor, was surprisingly present in the outer, proliferating cells, whereas expression of CDK inhibitors p18INK4c and p27kip1 was upregulated with increasing distance from the TS periphery. A decrease in proliferation from the TS periphery to the inner core was shown by Takagi et al. [147]. The authors showed that Ki-67 expressing cells were restricted to the peripheral TS layer and absent from the intermediate hypoxic layer and inner necrotic core.

The majority of studies investigating changes in TS oxygenation and proliferative behaviour compare the respiratory activity of TSs of differing maturity (young versus old) or size (small versus large) [35, 58, 59]. The authors [35, 58, 59] relate the observed decrease in proliferation with the development of hypoxia and accumulation of non-proliferating cells in the inner TS region. Other studies have analysed the decrease in proliferation from the TS periphery with the aim of determining the molecular basis of the accumulation of the quiescent cell phenotype in the inner TS region [182] or assessing the reduction in mitochondrial activity in the quiescent phenotype in the inner hypoxic region [103, 183].

Whilst a great amount of data points to an inverse relationship between hypoxia and proliferation in TSs, it is not fully evident how the two develop *temporally*. It is uncertain whether hypoxia forms before a decrease in proliferation is observed, or if the negative effect of hypoxia on proliferation is instantaneous. Additionally, it remains unknown whether all cells stop proliferating over time in hypoxic regions or if proliferative heterogeneity is maintained in hypoxia.

4.1.5 Experimental evaluation of tissue hypoxia

Tumour oxygenation can be estimated clinically using various experimental techniques. For a comprehensive review on the methods of measurement of oxygen concentration in mammalian tissues, please refer to Gallez et al. [184]. Use of oxygen-sensitive electrodes is the most common method [185, 186]. An oxygen-sensitive electrode consists of an anode and a cathode in contact with an electrolyte solution and covered by a semipermeable membrane. Oxygen diffuses through the membrane to the cathode, where it is reduced. The current produced by the electrode is proportional to the oxygen tension in the solution. Figure 4.4 explains the method of oxygen detection with the oxygen-sensitive electrode.



Cathode $O_2 + 4H^+ + 4e^- \longrightarrow 2H_2O$

Anode $4Ag + 4Cl^- \longrightarrow 4AgCl + 4e^-$

Overall: $4Ag + 4Cl^- + 4H^+ + O_2 \longrightarrow 4AgCl + 2H_2O$

Figure 4.4: Schematic adapted from Diepart et al. [187] to explain the mechanism of oxygen detection with the oxygen-sensitive electrode. The electrode consists of a platinum covered cathode (a) which, under the influence of a negative voltage from the anode (a reference Ag/AgCl electrode) (b), in the presence of an electrolyte solution (half-saturated KCl electrolyte) (c), reduces oxygen. The electrode is covered with a semi-permeable membrane (d), through which oxygen diffuses to reach the cathode and generates a current that is proportional to the oxygen concentration in the solution. Removal of electrons from solid silver produces silver ions. The silver ions combine with chloride ions in solution to precipitate silver chloride on the surface of the silver electrode. This leaves potassium ions behind; however, because hydrogen ions are taken out of solution by the consumption of oxygen, the charge remains balanced.

However, using the oxygen-sensitive electrode to measure hypoxia is limited by the invasive nature of the procedure and is restricted to accessible tumours.

The sampling ability of the oxygen-sensitive electrodes is limited as it is not possible to obtain an accurate spatial 'map' of tumour hypoxia, crucial for radiotherapy planning, while the use of HIF-1 expression as an intrinsic marker of hypoxia may not always be valid. Imaging methods, such as positron emission tomography (PET), combined with highly specific imaging markers targeted to hypoxic regions, provide a non-invasive alternative. ^{18}F-labelled fluoro-misonidazole is the most widely used PET imaging agent for hypoxia. For a detailed description of the available imaging markers used to detect tumour hypoxia, please refer to Krohn et al. [188].

From a preclinical perspective IHC methods can be used on *ex vivo* or *in vitro* samples, using hypoxia-selective nitroimidazole compounds such as pimonidazole, CCI-103F or EF5 [14, 73-75]. Systemically administered 2-nitroimidazoles, which undergo irreversible hypoxic bioreduction at pO_2 levels below 10 mm Hg, create intracellular adducts that are detectable by specific antibodies. These exogeneous biomarkers depend on the presence of viable cells with nitroreductase enzymes in order to facilitate binding under hypoxia. The IHC approach method allows for a quantitative assessment of the spatial distribution of hypoxia. Another advantage of bioreductive markers is the fact that they are selectively reduced only in viable hypoxic cells, which is advantageous over using oxygen-sensitive electrodes which show no discrimination between viable and non-viable cells.

pO_2 can be measured in several units: Pascal (Pa) is the accepted unit of pressure used in the international system. Other units include: the bar (1 bar = 100kPa), the atmosphere (1 atm = 101.325 kPa), the Torr (1 torr = 133.322 Pa), the millimetre of mercury (1 mm Hg = 133.322 Pa) and the percentage of oxygen (1% = 1.013 kPa)[189].

The most commonly used units in research describing tissue oxygen concentrations are mmHg and molarity (M = mol/L).

4.1.6 Aim of work

In order to gain a greater understanding of hypoxia, its development and how *temporally* it impacts cell proliferation we develop image analysis tools to enable the simultaneous quantification of hypoxia and cell proliferation in TS cross-sections. Using this approach, we quantify proliferation in different regions of oxygenation in DLD-1 TSs.

4.2 Methods

4.2.1 IHC markers

Methods were outlined in detail in Section 2.5.1. Briefly, three IHC markers were used: 1) EF5, a marker of hypoxia; 2) Ki-67, a marker of proliferation; 3) Hoechst 33342, a non-specific nuclear stain.

4.2.2 Epifluorescent image analysis of TS cross-sections

We perform structure analysis of TS cross-sectional images under the fundamental simplifying assumption that TSs are symmetric spheres with concentrically arranged regions of normoxia, hypoxia and severe hypoxia. In Figure 4.5 we show a schematic view of the 2D cross-sectional geometry of the central section of a TS. A similar approach

was taken by Freyer and Schor [190], Kunz-Schughart et al. [138], Freyer and Walenta et al. [109] among others.

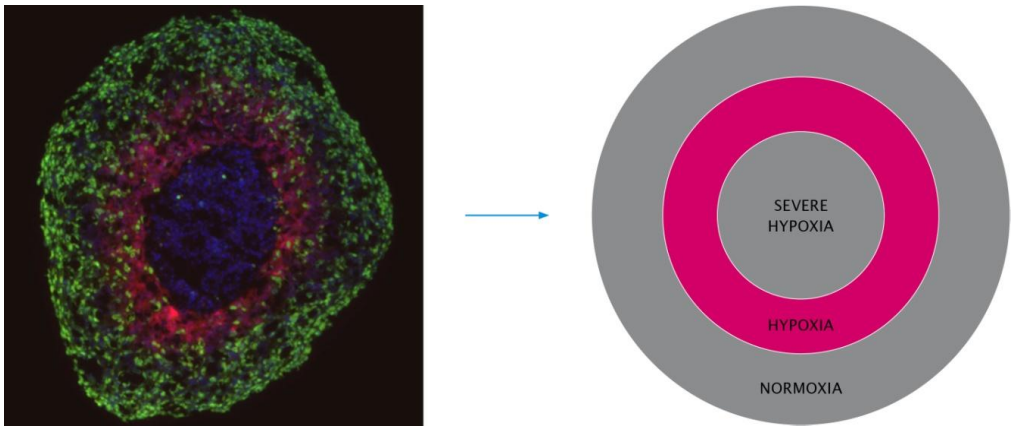


Figure 4.5: A schematic diagram of the method we use to analyse TS images. The existence of concentric regions of normoxia, hypoxia and severe hypoxia is a fundamental assumption that allows us to analyze the epifluorescent images based on hypoxia detection with EF5 marker. We aim to quantify the relationship between proliferative heterogeneity and TS oxygenation status at different TS radii.

Our method of image analysis is dependent on the division of the TS into normoxic, hypoxic and severely hypoxic regions, based on EF5 staining intensity. Koch and Evans [191] defined hypoxic tissue as that which is at 30% of maximum EF5 binding at least. Thus, in the present study we assign regions to be hypoxic above 30% of maximum EF5 binding. The normoxic region is located outside the identified hypoxic region whereas the severely hypoxic region is located inside the identified hypoxic region. The observation that TSs develop a central necrotic region at diameters above 500 µm has been widely accepted [147, 192]. We assume that severe hypoxia corresponds to the necrotic core region detected in the majority of TSs.

All images are pre-processed to separate R, G and B channels, and remove autofluorescence and non-specific background as outlined in Section 2.5.4. We use Matlab to perform the following steps:

1. The B (Hoechst 33342) channel is used to define the mask of the entire TS (Figure 4.6). The image is first smoothed using an averaging filter based on a square matrix to reduce smooth surface irregularities (Figure 4.6A). The image is then converted to a binary image (Figure 4.6B) where white pixels represent TS cells whereas black pixels correspond to non-tissue regions. Finally, a mask of the entire TS is created by filling in small holes in the TS detected in the binary image (Figure 4.6C).

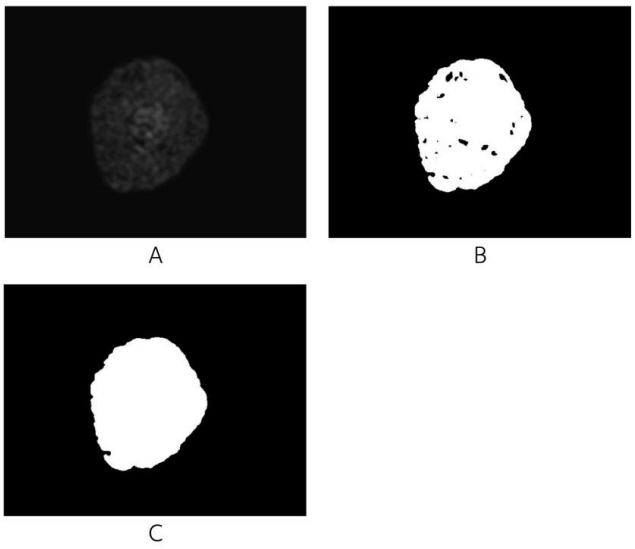


Figure 4.6: The method of creating a mask of the entire TS using the separated B channel. A) The image is smoothed. B) The image is converted to a binary image. C) The mask of the entire TS is created by filling small holes detected in TS region.

2. Next, the R (EF5) channel is used to define the hypoxic region (Figure 4.7). The image is first smoothed (using the same filter as the B channel) to reduce surface irregularities (Figure 4.7A). Pixels are classified as hypoxic if they fall in the range of 30% to 100% of maximal staining intensity of EF5 (Figure 4.7B). In cases of an incomplete or discontinuous hypoxic region, we reconstruct hypoxia by defining the mean inner and outer boundary points according to the assumption that hypoxia forms a concentrically arranged region between normoxia and severe hypoxia to create a mask of hypoxia (Figure 4.7 C).

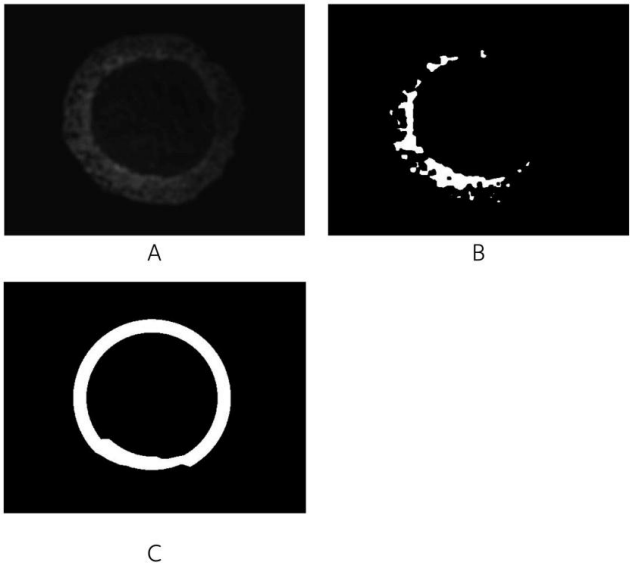


Figure 4.7: The method of creating a mask of hypoxia in a TS image using the separated R channel. A) The image is smoothed. B) All pixels in the range of 30% to 100% of the maximal staining intensity in the R channel are classified as hypoxic. The selected EF5-Cy3 positive pixels are represented as a binary image. C) The hypoxic region is reconstructed by defining the mean inner and outer boundary points according to the assumption that hypoxia forms a concentrically arranged region between normoxia and severe hypoxia to generate a mask of the hypoxia.

3. Having generated a mask of the entire TS and a mask of hypoxia we can obtain the mask of normoxia and the mask of severe hypoxia as presented in Figure 4.8 and Figure 4.9.



Figure 4.8: Example of the normoxic mask calculation. We subtract the 'filled in' hypoxic mask from the mask of the entire TS to obtain the normoxic mask.

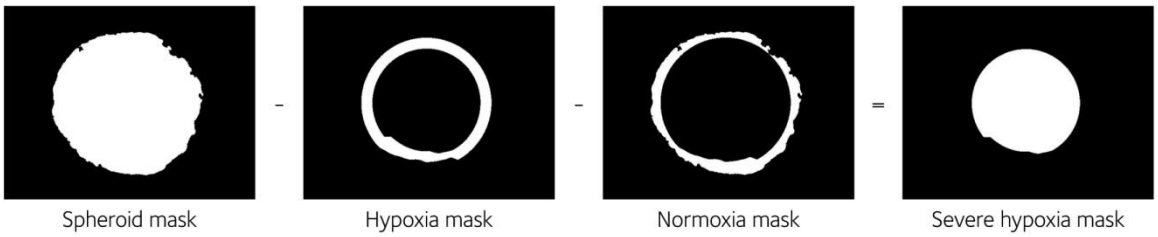


Figure 4.9: Example of the severely hypoxic mask calculation. We subtract the normoxic and hypoxic masks from the mask of the entire TS to obtain the severely hypoxic mask.

4. To quantify the fraction of proliferating cells, the G channel is used. Pixels which are Ki-67 positive are classified as proliferating.
5. To quantify the fraction of non-proliferating cells, the B channel is used. Pixels which are Hoescht 33342-positive, but Ki-67 negative are classified as non-proliferating.
6. Finally, we calculate the total number of proliferating and non-proliferating pixels in normoxia, hypoxia and severe hypoxia based on the defined masks, as shown in Figure 4.10.

In the case of early time points of growth, we are aware that the hypoxic region might not have yet developed. Thus, if we cannot detect hypoxia, then we assume that all cells are normoxic.

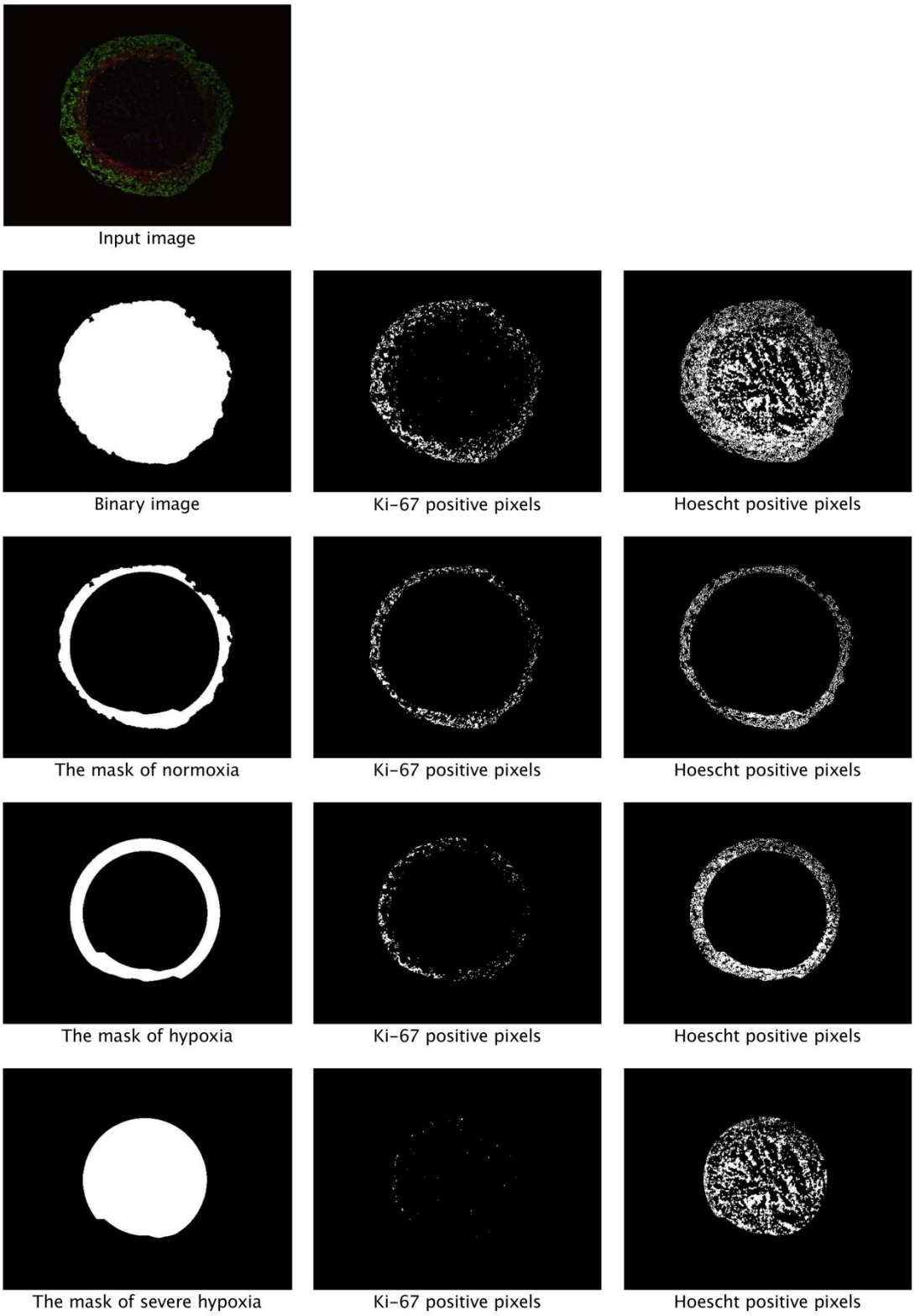


Figure 4.10: Example of division of a TS into regions of normoxia, hypoxia and severe hypoxia using the defined masks. The division of a TS into regions allows for quantification of the number of Ki-67 positive and Hoescht 33343 positive pixels within the normoxic, hypoxic and severely hypoxic regions.

4.3 Results

Example images of TS sections from Days 2-20 are shown in Figure 4.11. We observe that hypoxia (red) develops at day 4 of TS culture time, with the diameter of the hypoxic region increasing initially before plateauing after day 6. Severe hypoxia which corresponds to a non-viable core (predominantly blue) appears at day 6, increasing in size throughout the remainder of culture. Whilst the TS is initially composed primarily of proliferating cells, a non-proliferating cell fraction develops quickly during growth. Proliferating cells, whilst not solely restricted to the normoxic region of the TS, are seen at a lower frequency under hypoxia.

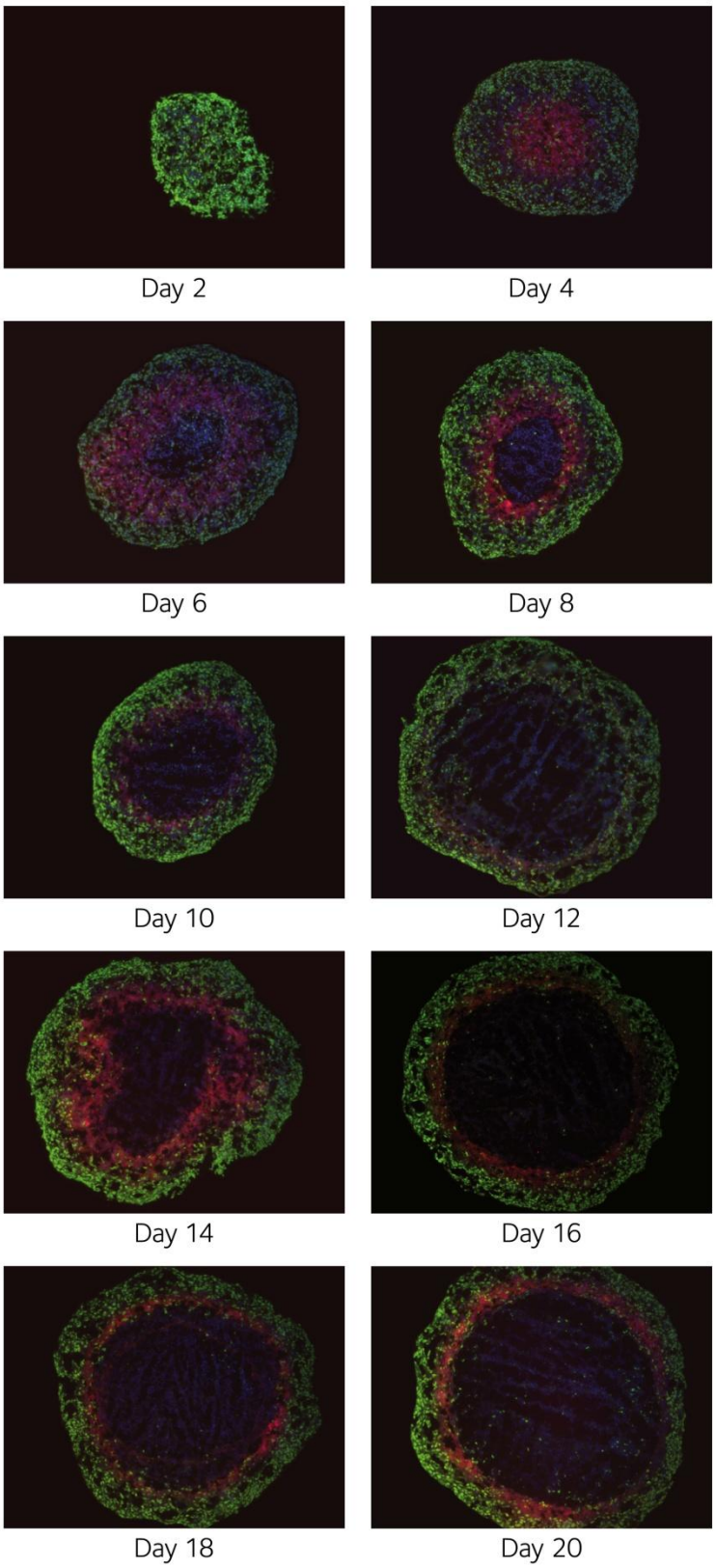


Figure 4.11: Representative images of TS cross-sections stained for proliferation (Ki-67-FITC, green), hypoxia (EF5-Cy3, red) and cell nuclei (Hoechst 33342, blue) over the time course of culture.

4.3.1 Quantitative assessment of changes in normoxia, hypoxia and severe hypoxia during TS development

Figure 4.12 shows the relative contribution of normoxic, hypoxic and severely hypoxic regions extracted from the images using the methods described in Section 4.2.2. We find that the normoxic fraction accounts for the entire TS cross-sectional area in the early period of TS growth (100% at 2 days), after which the hypoxic and severely hypoxic regions develop. Consequently, the fraction of the normoxic region decreases to contain 83% of the total TS cross-sectional area at day 4 and 38% at day 6 and is maintained at approximately the same level until the end of TS culture time. A 1-way ANOVA showed that there was no significant difference in changes in normoxic fraction between time points (P value > 0.05) except day 4 and 10 and day 4 and day 20 (P value < 0.05) as shown by Bonferroni's multiple comparison test.

We detect a hypoxic fraction at the second examined data point (day 4 of TS culture time), at which time it comprises 16% of the total TS cross-sectional area (Figure 4.12). After day 4 the hypoxic fraction comprises between 7-13% of total TS cross-sectional area until the end of culture time. Lack of changes in hypoxic fraction between time points was verified by a 1-way ANOVA which showed that the results were not statistically different (P value > 0.05). The severely hypoxic region is detectable at day 4, but at this time point it contributes a very small fraction (less than 1%) to the total TS cross-sectional area (Figure 4.12). Following day 4, the region of severe hypoxia expands to comprise 56% of the total TS area at day 6, and continues to comprise more than half of the total TS cross-sectional area until the end of TS culture time (up to 64% fraction of total TS cross-sectional area at day 20). A 1-way ANOVA showed that changes in severely hypoxic fraction between time points were significantly different (P value < 0.05) in

comparison to severely hypoxic fraction detected at day 4 as shown by Bonferroni's multiple comparison test.

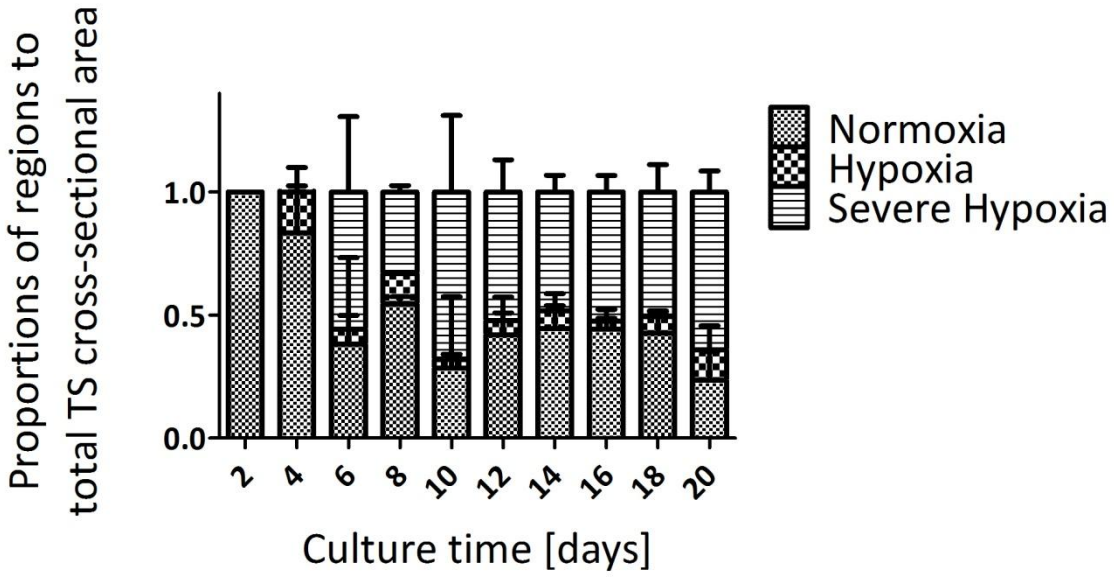


Figure 4.12: Composition of a TS based on mean total number of pixels that make up regions of normoxia, hypoxia and severe hypoxia at different times of TS growth. All data in each column represent the mean pixel values of between two to four TS images and the error bars represent standard deviation.

By using the proportions calculated in Figure 4.12 and the cross-sectional area (calculated by integrating all pixels within a TS obtained in Chapter 3) we obtain radii of normoxia, hypoxia and severe hypoxia. We show the radial contributions of normoxic, hypoxic and severely hypoxic regions in Figure 4.13. Statistical significance for radii measurements was determined using 1-way ANOVA and post-hoc Bonferroni's multiple comparison test and the results were compared to the initial measured data point. We observe that the radius of the normoxic region was equal to 0.12 mm at day 2 and with some variation was maintained of approximately the same size over the course of TS growth. A 1-way ANOVA showed that changes in normoxic radius were not statistically significant (P values > 0.05). The radius of hypoxia equal to 0.09 mm at day 4 decreased throughout TS growth and was equal to 0.05 mm at day 20. A 1-way ANOVA showed that

the observed decrease in hypoxic radius from day 4 to day 20 was not statistically significant (P values > 0.05). The largest increase in radius is of severe hypoxia, which increased by approximately two orders of magnitude (from 7.2 x 10^{-3} mm at day 4 to 0.56 mm at day 20). A 1-way ANOVA showed that the observed increase in severe hypoxic radius taken over culture time was statistically significant (P values < 0.05).

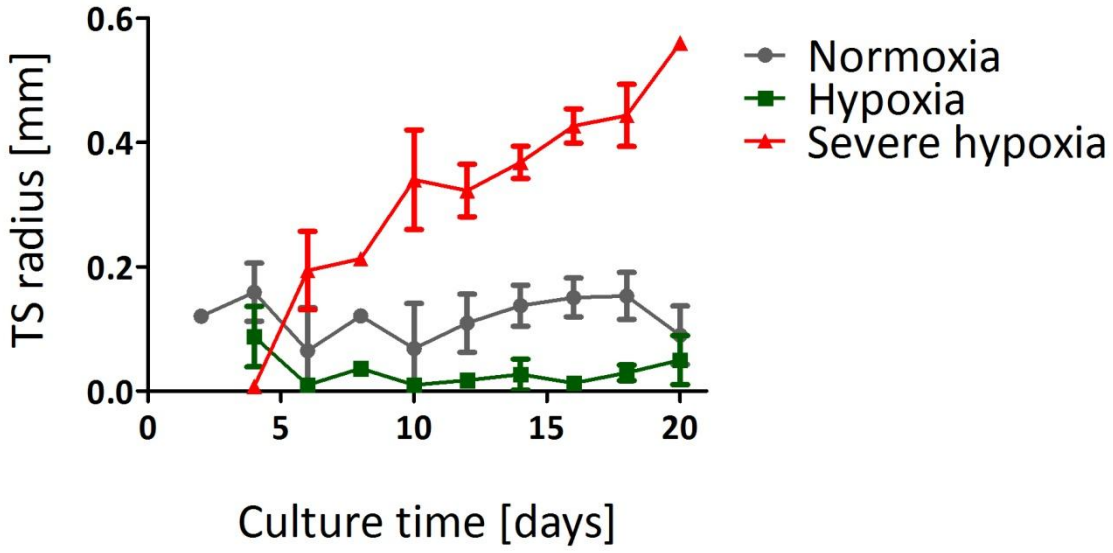


Figure 4.13: Changes in the radii of normoxia, hypoxia and severe hypoxia regions during TS growth. All data were quantified using the proportions of normoxic, hypoxic and severely hypoxic regions shown in Figure 4.12 and the cross-sectional area calculated by integrating all pixels within a TS obtained in Chapter 3. The error bars represent standard deviation from the mean radii.

4.3.2 Proliferation decreases, but is not fully diminished, under hypoxia

From Figure 4.11, it is evident that proliferating cells are located not only in normoxic regions, but also in hypoxic regions. To further analyse and quantify the relationship between hypoxia and proliferating cell behaviour we analyse the mean proportion of the proliferating fraction in each region. Figure 4.14 shows that Ki-67-

positive pixels account for 44% of pixels at day 2 and more than 25% of pixels in the normoxic region throughout TS growth.

Once we detect hypoxia at day 4, proliferation is instantaneously affected by oxygen tension and reduced to comprise 10% of the cross-sectional area of hypoxia (Figure 4.14). At the remaining time points the fraction of proliferative cells is maintained at the same level and comprises approximately 10-16% of cross-sectional area of hypoxia (16% of cross-sectional area at day 20). Our findings show that hypoxia does not fully inhibit proliferation.

In the severely hypoxic region, the proportion of proliferative cells is found to be at a minimum (proliferating cells comprise less than 3% of total cross-sectional area of severe hypoxia at the majority of time points). The remaining large fractions of the normoxic, hypoxic and severely hypoxic regions consist of non-proliferating cells. 2-way ANOVA revealed a significant effect of hypoxia and severe hypoxia on proliferation (P values < 0.0001) and showed that changes in proliferation at different time points of TS growth were not significant (P values > 0.05).

Finally, Figure 4.15 shows that Ki-67-positive population was approximately 80-98% reduced in response to hypoxia and severe hypoxia and these changes were statistically significant (2-way ANOVA, P values < 0.0001). There was some variation in the magnitude of the reduction in Ki-67-positive population in response to hypoxia and severe hypoxia between time points of TS culture which was statistically significant as revealed by 2-way ANOVA (P values < 0.05).

The results were confirmed by manual counting of Ki-67-positive cells and total number of cells in four randomly selected cross-sectional TS images.

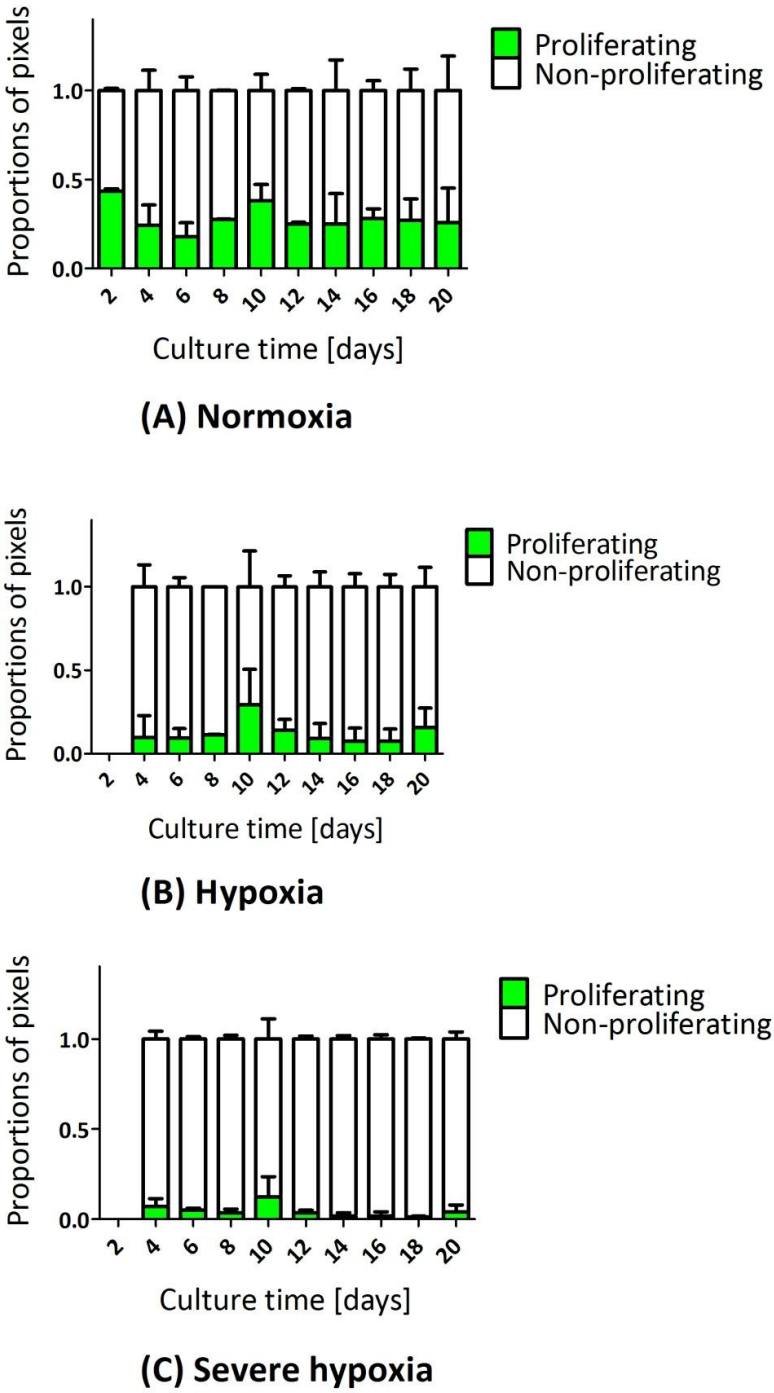


Figure 4.14: Quantification of the fraction of proliferating (the mean number of Ki-67-FITC positive pixels detected in the G channel) and non-proliferating cells (the mean number of Hoescht 33342 positive pixels detected in the B channel) in (A) normoxic, (B) hypoxic and (C) severely hypoxic regions over the time course of TS culture. All data represent the mean number of pixel values for between two and four TS images. For simplicity the results shown in each histogram are normalised to 1. The error bars represent standard deviation from the mean fractions of proliferating and non-proliferating cells.

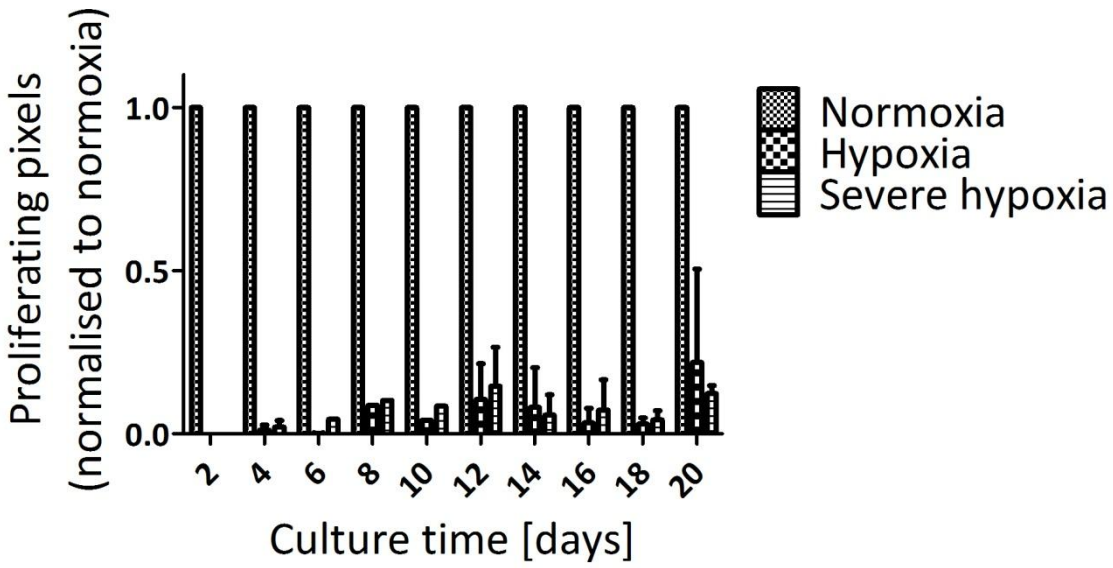


Figure 4.15: Quantification of changes in the fraction of proliferating (the mean number of Ki-67-FITC positive pixels detected in the G channel) pixels in response to hypoxia and severe hypoxia. For simplicity the mean numbers of proliferating pixels in hypoxia and severe hypoxia were normalised to the mean number of proliferating pixels in normoxia which was assumed to be equal to 1. The error bars represent standard deviation from the mean fractions of proliferating pixels in hypoxia and severe hypoxia.

4.4 Discussion

The relationship between oxygenation and proliferation in DLD-1 TSs was similar to that reported in other TS types; i.e. a reduction in proliferation with increasing distance from TS boundary and presence of hypoxia in the inner TS region [103, 109, 116, 138, 193, 194]. The presence of proliferating cells in hypoxic regions was observed throughout the culture time (on the final day of culture, approximately 10-16% of the hypoxic fraction was proliferative).

We detected hypoxia at day 4 (TS radius was equal to 253 μm), which was concomitant with the 98% reduction in proliferation. Our findings show that the negative effect of hypoxia on proliferation occurs within a 48 h time period.

We note that a decrease in the extent of the hypoxic region, as a proportion of the total TS cross-sectional area, coincided with the development of severe hypoxia which took over the majority of the TS region after day 6 (TS radius was equal to 268 μm) of culture time. Ballangrud et al. [130] observed a development of necrotic core in LNCaP prostate cancer TS occurs at a similar size (TS radius of 300 μm) hence, our results support the ones previously reported in the literature. As discussed in Chapter 3, a TS increases in size until the end of TS culture time, when it quickly disintegrates. We showed in this chapter that towards the end of culture, TSs were primarily comprised of severely hypoxic and necrotic cells, which is a probable underlying reason of disintegration.

According to the literature the peripheral oxygen diffusion depleted zone starts at approximately 0.1-0.12 mm from the TS boundary based on experimental results from numerous cell lines [138, 195, 196]. Our results show that oxygen supplies, on average, the outer approximately 0.12 mm of a TS which corresponds to the normoxic radius. Whilst there is a variation in a distance from the TS boundary at which we detect hypoxia these values are within the range of values previously reported [138, 195, 196].

Further work is needed to investigate the distribution of proliferating cells in hypoxia. Firstly, we should determine what fraction of non-proliferating cells is quiescent (for example using a quiescent marker such as p27) and what fraction is apoptotic (for example using an apoptotic marker such as caspase-3) to further investigate the relationship between proliferation and hypoxia. We should also test different hypoxic (such as HIF-1α) and proliferating markers (for example, cyclin E) to determine what is the association between the method of hypoxia detection and the number of proliferating cells present. As hypoxia and proliferation are determinants of a tissue's response to radiation and chemotherapy [197], in order to make our study clinically relevant in future work we need to evaluate the response of DLD-1 TSs to these two most common types of non-

surgical cancer treatment modalities. Further quantitative assessment of hypoxia and proliferation could give us insight on how a combination of these biological properties underlies the development of resistance to radiotherapy in solid tumours. We suggest that these changes should be investigated in multiple standard cancer cell lines.

We note that the sample size in our study is small (minimal number of TS cross-sections analyzed per one time point is two). However, this constraint is not caused by our method of image analysis but is a result of the time-consuming nature of IHC. We have developed a robust method of epifluorescent image analysis of hypoxia and proliferation, which is easily applicable to data as it is generated. Thus, although our limited dataset precludes statistically-verified conclusions, the analysis of further experimental data should be straightforward.

Our findings highlight the important point, often neglected by mathematical models of TS growth, that not all cells located in the hypoxic region of a TS are non-proliferating or quiescent. In Chapter 5 we will exploit the quantitative results we have obtained here and formulate a mathematical model of oxygen distribution in a TS.

Chapter 5 Integrative study of the role of proliferation in defining oxygen gradients in TS

In Chapters 3 and 4, we used image analysis techniques to extract quantitative data on TSs with a view to enabling further analysis. In this chapter we use these data, in combination with simple mathematical models, to ask whether the spatiotemporal changes in proliferative status observed in Chapter 4 have a quantifiable effect on oxygen distribution, through modulation of oxygen consumption.

5.1 Introduction

Oxygen consumption has been shown to approximately follow Michaelis-Menten kinetics [198-202]. Briefly, the Michaelis-Menten model predicts that the velocity of a reaction is given by

$$f(C) = \frac{vC}{C + K}, \tag{5.1}$$

where *v* denotes the maximal rate of oxygen consumption and *K* is an effective Michaelis constant, corresponding to the oxygen concentration at which the consumption rate takes half its maximal value. *f(C)* increases approximately linearly with substrate concentration (*C*) when the substrate concentration is low and saturates when substrate

concentration goes above *K* [68]. For most enzymes, the value of *K* is 10-100 times greater than the typical cellular substrate concentration. As the *K* value for oxygen consumption is lower than the concentration of oxygen detected in most cells, the measured rate of oxygen consumption largely corresponds to *v* [203].

Oxygen consumption rates, whilst varying significantly between cell lines, are generally lower under hypoxic conditions than under normoxia [204, 205]. This is partially attributable to the reduced availability of molecular oxygen, lowering the effective rate of consumption, according to equation (5.1). However, the accumulation of HIF-1 under hypoxic conditions acts via several mechanisms to lower the maximal rate of oxygen consumption [154, 155, 206-208]. Reducing the cellular capacity to consume oxygen when oxygen is sparse may initially seem counterintuitive; however, under hypoxic conditions, the lack of molecular oxygen as the final electron acceptor in the respiratory chain transport is associated with electron leakage, resulting in increased Reactive Oxygen Species (ROS). ROS are extremely toxic, so one HIF-1 target, PDK, suppresses metabolism through the tricarboxylic acid cycle (TCA) by inactivating pyruvate dehydrogenase (PDH), the enzyme which converts pyruvate to acetyl-CoA [26]. ATP production is instead derived from glycolysis (which will be discussed in Chapter 6).

The proliferative status of a cell has also been shown to affect the rate of oxygen consumption, with quiescent cells demonstrating an inherently lower rate of oxygen utilization [58, 59]. V-79 cells cultured as a monolayer have been shown to consume 5-times more oxygen when proliferating vs. non-proliferating, while a reduction in oxygen consumption of almost a half has been observed in non-proliferating EMT6/Ro cells compared with the corresponding proliferating phenotype [58, 59]. As discussed in Section 4.1.3, HIF-1 plays a major role in reducing proliferation, through promotion of quiescent phenotype.

5.1.1 Oxygen consumption in TS

Mean oxygen consumption rates per viable cell, for cells cultured as TSs, have been shown to be lower than for cells cultured as monolayers [59, 209, 210], for example, in the case of the V-79 cell line, oxygen consumption is 20% lower in TSs than in monolayers [59]. Over the course of TS culture, oxygen consumption also declines. Freyer and co-workers [59] observed that the rate of oxygen consumption, measured with the oxygen-sensitive electrode, was reduced in large V-79 TSs (above 400 μm orthogonal diameter) to 25% of that detected in small TSs (below 200 μm orthogonal diameter). Using the EMT6/Ro cells, the authors observed that oxygen consumption in large TSs (1300 μm in diameter) was 40% of that in small TSs (150 μm in diameter). Rodríguez-Enríquez et al. [35] made similar observations using TSs derived from the HeLa and Hek293 cell lines. Taken together, these studies demonstrate that oxygen consumption decreases at some point during TS development.

So, why does oxygen consumption decrease over the course of TS culture? One obvious hypothesis is that the development of hypoxia, and the subsequent activation of HIF-1, results in reduced mitochondrial activity, by shifting metabolism to a glycolytic phenotype. Indeed, the expression of HIF-1α was observed to be approximately 3-fold higher in old vs. young HeLa TSs (14-15 day vs. 11-12 day culture, respectively) [35]. Another hypothesis is that a decline in proliferative fraction reduces oxygen requirement. Bredel-Geissler and colleagues [194] observed that non-proliferating cells within TSs had a reduced cytoplasmic volume with fewer mitochondria.

Mathematical modelling of hypoxia and proliferation has the potential to help understand the dynamic alterations observed in oxygen consumption throughout TS growth. The first model linking the consumption and diffusion of nutrients with tumour

proliferation was proposed by Thomlinson and Grey in 1955 [211]. Greenspan furthered this model by linking cell proliferation and death with the concentration of a single 'generic' nutrient, as well as the action of a cell division inhibitor produced within the tumour [212]. The model predicted that when a tumour is very small, every cell receives an adequate supply of nutrients by simple diffusion, and the entire population is proliferating. Since nutrients are consumed by cells located on the outer rim of the tumour, their concentrations should decrease towards its centre, and below a certain nutrient threshold, cells cease to proliferate. As the TS increases in size, nutrient levels fall below a certain critical value where cells are unable to survive, causing the development of a necrotic centre. This model therefore predicts the three distinct compartments of proliferating, quiescent and necrotic cells we observed in Chapter 4.

Since Greenspan's work, many mathematical models have been developed to describe the diffusion of nutrients from the surrounding microenvironment into TSs. A comprehensive review of the most influential mathematical models in the area of TS growth is given by Roose et al. [117].

Although the majority of models in this area consider the concentration of a single 'generic' nutrient as the crucial determinant of *in vitro* tumour proliferation [212-215], a few recent models have attempted to describe the bioenergetic role of multiple nutrients. The most advanced mathematical models in the area of TS growth and metabolism are those developed by Casciari et al. [53], Bertuzzi et al. [54, 55] and Venkatasubramanian et al. [56]. These complex, multispecies models describe the interaction of various nutrients and other factors with the tumour, showing how tumour heterogeneity develops and how the interaction of different factors promotes or limits tumour proliferation.

Casciari's model describes oxygen consumption using Michaelis-Menten kinetics, with *v* and *K* being functions of the levels of glucose and pH [53]. What is fairly unique about this model is that it is parameterised from experimental data measured in EMT6/Ro cells. Venkatasubramanian et al. [56] present a more sophisticated form for the rate of oxygen consumption, by linking the stoichiometry of cellular metabolism with changes in glucose and lactate levels, quantifying the relationship in terms of ATP production. A similar approach is adopted by Bertuzzi et al. [55]. Although this approach to derivation of the rate of oxygen consumption is undoubtedly more sophisticated than that adopted by Casciari et al. [53], Casciari's more simple approach is parameterised using a single experimental data set, so is potentially more 'robust'.

Although the above models have been very useful in determining how changes in the availability of oxygen (and other nutrients) affect proliferation, none consider that proliferation itself has an impact on oxygen consumption, the distribution of oxygen and the development of hypoxia.

5.1.2 Oxygen consumption rates in the literature

Wagner et al. [203] undertook a comprehensive survey of experimentally-determined oxygen consumption rates in different tissues, with details of the cell lines and methods used to obtain these values. Although the DLD-1 cell line was not included in this review, the authors reported that the value of *K* for cellular oxygen uptake for most cells is on the order of 1 μM or less [202, 218, 219] with the maximal oxygen consumption rate *v* varying in order of magnitude from 10^{-15} to 10^{-17} mol $s^{-1}cell^{-1}$. Consumption rates in mathematical models tend to be reported in units of mM s^{-1}, necessitating a conversion of units from experimental findings. In a recent mathematical model describing

metabolic acidosis in TSs, Tindall et al. [220] use a relatively high constant value for the rate of oxygen consumption, taken to be 2.2×10^{-1} mM s^{-1}, which they justify by referring to the work of Banaji et al. [221]. This is a higher estimate than the value 7.16 x 10^{-2} mMs^{-1} used by Venkatasubramanian et al. [56]. The source of this discrepancy may be that Banaji et al. [221] estimated the oxygen consumption for cerebral tissue, which has high respiratory activity in general. The parameter estimates provided by Banaji et al. [221] suggest that the value given by Tindall et al. [220] is likely to be an overestimate. Therefore, using the parameter estimate of the rate of oxygen consumption given by Tindall at al. [220] in TSs might not fully represent their metabolic requirement and growth state, and lead to uncertainties about the accuracy of the obtained results.

Overall, a wide range of estimates for the rate of oxygen consumption in tissues has been reported in the modelling literature. We summarise the variation in these parameter estimates in Table 5.1. In contrast, there is little variation in estimates for the Michaelis constant and diffusion coefficient of oxygen in tissue.

Reference	Study	*K* [mM]	*v* [mol cell^{-1} s^{-1}]	Oxygen consumption	*D* [cm^2 s^{-1}]
Bertuzzi et al. [55]	Model	4.64 x 10^{-3}	$\varsigma 2f(G) + pL$ *	Michaelis-Menten	–
Buchwald [216]	Experiment	1 x 10^{-3}	3.40 x 10^{-17}	Michaelis-Menten	2.0 x 10^{-5}
Casciari et al. [53]	Model	4.64 x 10^{-3}	$7.16 \times 10^{-17} + \frac{2.02 \times 10^{-21}}{GH^{1.912}}$ **	Michaelis-Menten	–
Grote et al. [195]	Experiment	–	–	–	1.75 x 10^{-5}
Jiang et al. [222]	Experiment	–	–	–	1.65 x 10^{-5}
Lyabakh and Mankovskaya [223]	Experiment	4.35 x 10^{-3}	–	–	1.3 x 10^{-5}
McGoron et al. [201]	Experiment	4.35 x 10^{-5}	–	Michaelis-Menten	
Nichols and Foster [224]	Experiment	–	–	–	1.46 x 10^{-5}
Tindall et al. [220]	Model	–	2.2 x 10^{-16}	Mass action	1.5 x 10^{-5}
Mueller-Klieser & Sutherland [225]	Experiment	–	–	–	1.82 x 10^{-5}

Table 5.1: Summary of estimates for the parameters *K* and *v* in the Michaelis-Menten model of oxygen consumption kinetics and the diffusion coefficient of oxygen in tissue *D*. References include experimental studies and modelling papers. * The notation used here in the functional form, derived by Bertuzzi et al. [55] for the dependence of *v* on other factors, is as follows: **ς** represents the maximal rate of pyruvate oxidation; *G* and *L* denote the extracellular concentrations of glucose and lactate, respectively; *f* denotes the glucose consumption rate which itself is assumed to have a Michaelis-Menten dependence on glucose concentration, and the parameter *p* represents transmembrane lactate transport. ** The notation used here in the functional form, derived by Casciari et al. [53] for the dependence of *v* on other factors, is as follows: *G* and *H* denote the concentrations of glucose and hydrogen ions, respectively.

5.2 Aim of work

Our primary aim is to investigate the relationship between proliferation and oxygen consumption and their role in forming oxygen gradients within TSs. We develop a simple model of oxygen transport and consumption to predict the oxygen thresholds of hypoxia and severe hypoxia. We analyse the impact of considering proliferative status heterogeneity in the context of a biologically realistic reduction in oxygen consumption in non-proliferating cells. Using the results of theoretical simulations, together with our experimental data from Chapter 4, we ask whether consideration of proliferation is needed to accurately predict hypoxia within TSs.

5.3 Model development

In this section we develop a simple mathematical model to describe the distribution of oxygen in a TS of a specified size. We adopt a continuum modelling approach and thus derive a reaction-diffusion equation for the oxygen concentration within the TS. A similar approach has been used in numerous studies on the distribution of oxygen within tissues, such as in the papers by Buchwald [216], Kyle and Minchinton [217], McGoron et al. [201], and Venkatasubramanian et al. [56]. We consider changes in oxygen concentration due to two processes: diffusion into and within the TS; and consumption by cells.

5.3.1 Modelling oxygen diffusion

We model the diffusion of oxygen into a TS using Fick's laws [119], which relate the diffusive flux of a dissolved substance to its concentration. In the case of oxygen transport, Fick's first law states that a flux occurs from regions of high concentration to regions of low concentration, with a flux magnitude that is proportional to the concentration gradient. In one spatial dimension, Fick's first law can be written as

$$J = -D\,\frac{\partial C}{\partial x}, \tag{5.2}$$

where J represents the diffusive flux, C denotes concentration (expressed in mM), x denotes the spatial coordinate, and the constant of proportionality D is termed the diffusion coefficient (expressed in $\mu m^2\ s^{-1}$). Note the minus sign in equation (5.2), which reflects the fact that the flux occurs in the direction of decreasing concentration. In two or more spatial dimensions this relationship has the generalized form

$$\boldsymbol{J} = -D\nabla C, \tag{5.3}$$

where ∇ denotes the gradient operator. Fick's second law states that the rate of change of concentration with time is related to the flux J via the equation

$$\frac{\partial C}{\partial t} = -\nabla \cdot \boldsymbol{J} = \nabla \cdot (D\nabla C), \tag{5.4}$$

where t denotes time (expressed in sec) and the expression $\nabla \cdot \boldsymbol{J}$ denotes the divergence of the flux. Under the common simplifying assumption that the diffusion coefficient is constant, Fick's second law simplifies to

$$\frac{\partial C}{\partial t} = D\nabla^2 C, \tag{5.5}$$

where $\nabla^2 C$ denotes the Laplacian of the concentration. This expression takes different forms depending on the choice of coordinate system. In the idealised case of a radially symmetric TS, spherical polar coordinates (r, θ, φ) are appropriate. In this case, for spherically symmetric initial and boundary conditions, the oxygen concentration varies with the distance from the TS boundary r, but does not vary with polar angle θ or azimuthal angle φ. In this case the Laplacian of the concentration is given by the expression

$$\nabla^2 C = \frac{1}{r^2}\frac{\partial}{\partial r}\left(r^2 \frac{\partial C}{\partial r}\right). \tag{5.6}$$

Thus, the rate of change in oxygen concentration C within the TS, due to diffusion and consumption, is given by

$$\frac{\partial C}{\partial t} = D\nabla^2 C - f(C)\,. \tag{5.7}$$

We now replace the Laplacian operator with its spherically symmetric expression (5.6) to obtain

$$\frac{\partial C}{\partial t} = D\,\frac{1}{r^2}\frac{\partial}{\partial r}\left(r^2 \frac{\partial C}{\partial r}\right) - f(C)\,. \tag{5.8}$$

This partial differential equation (PDE) is satisfied by the oxygen concentration $C(r,t)$ for $t > 0$ and $0 < r < R$, where R denotes the radius of the TS. Since the rate of cell division is much longer than the typical timescale of oxygen diffusion across the TS, we make the simplifying assumption that R is a fixed value.

To close the system we must supply initial and boundary conditions. We supply a spatially uniform initial oxygen profile,

$$C(r,0) \equiv C_0\,, \tag{5.9}$$

for $0 < r < R$. For all $t > 0$ we impose a regularity condition at the centre of the TS:

$$\frac{\partial C}{\partial r}(0,t) = 0\ . \tag{5.10}$$

Finally, we make the standard assumption that the exterior of the TS is well-mixed and that oxygen is in excess there. This is equivalent to assuming a very high mass transfer coefficient of the TS boundary to oxygen, which allows us to approximate the boundary condition for C at $r = R$ by the Dirichlet (fixed value) condition

$$C(R,t) = C_0\ , \tag{5.11}$$

for all $t > 0$.

5.3.2 Modelling oxygen consumption

In the following, we present two different cases of oxygen consumption, one proliferation-independent (Model 1) and one proliferation-dependent (Model 2).

Model 1: Michaelis-Menten description of oxygen consumption

In our first model, we assume that the rate of oxygen consumption, $f(C)$, may be described throughout the tumour, independent of proliferative status, by the Michaelis-Menten function denoted in equation (5.1). We emphasise that in the context of our work the Michaelis-Menten model is phenomenological, rather than rigorously derived, hence our referral to K as an *effective* Michaelis constant.

Model 2: Incorporating proliferative heterogeneity

In our second model of oxygen consumption we introduce an additional degree of complexity to Model 1, by incorporating a term which reduces the rate of oxygen consumption in non-proliferating cells compared to their proliferating counterparts.

To define proliferative status at any given point, we take the results obtained in Chapter 4 and assign different proportions of proliferating and non-proliferating cells to each defined region of normoxia, hypoxia and severe hypoxia. To model the non-homogeneous composition of normoxic, hypoxic and severely hypoxic regions, we introduce different volume fractions of proliferating and non-proliferating cell types in each region. We define seven new parameters: α_N (β_N), α_H (β_H), α_S (β_S), which denote the fractions of proliferating (non-proliferating) cells in normoxic, hypoxic and severely hypoxic regions, respectively; and lastly we assume that non-proliferating cells consume oxygen at a rate that is a constant fraction (δ) of the rate of consumption by proliferating cells. Thus, in our Model 2, we assume an explicit dependence of the rate of oxygen consumption on the radial position (r) in addition to the oxygen concentration (C). Hence, the oxygen consumption $f(C,r)$ takes the functional form

$$f(C,r) = \begin{cases} \dfrac{vC}{C+K}\,(\alpha_N + \beta_N\delta), & if\ \ r > R_1 \\ \dfrac{vC}{C+K}\,(\alpha_H + \beta_H\delta), & if\ \ R_2 < r \le R_1 \\ \dfrac{vC}{C+K}\,(\alpha_S + \beta_S\delta), & if\ \ r \le R_2, \end{cases} \tag{5.12}$$

where R_1 and R_2 represent the experimentally determined radii for hypoxia and severe hypoxia, respectively, with $R_1 > R_2$. A summary of the parameters and units present in equation (5.12) is provided in Table 5.2. We discuss the estimation of these parameter values in Section 5.3.3.

Parameter	Description	Units
v	Maximal rate of oxygen consumption	mM s^{-1}
K	Effective Michaelis constant	mM
δ	Non-proliferating cell oxygen consumption fraction	Dimensionless
α_N, α_H, α_S	Fractions of proliferating cells in normoxic (*N*), hypoxic (*H*) and severely hypoxic (*S*) regions respectively	Dimensionless
β_N, β_H, β_S	Fractions of non-proliferating cells in normoxic (*N*), hypoxic (*H*) and severely hypoxic (*S*) regions	Dimensionless

Table 5.2: Summary of the parameters present in equation (5.12).

In summary, in this model we extend Model 1 by incorporating additional biological information about different proportions of proliferating and non-proliferating cell fractions in regions of normoxia, hypoxia and severe hypoxia, using the experimental data obtained in Chapter 4. The proliferating and non-proliferating cell fractions obtained by quantitative analysis of cross-sectional images are presented in Figure 4.8 in Chapter 4.

5.3.3 Parameter estimation

We note from Section 5.1.2 that not only do estimates of oxygen consumption rates vary significantly, many existing mathematical models of tumour metabolism estimate parameter values by citing other theoretical references [53-56], not experimental studies. Hence, it is difficult to determine *representative* values of the parameters of interest. Thus, when deriving 'baseline' values (from the literature) for our model parameters in the next section, we decide to choose values which are typical values for the TS system.

In order to obtain parameter values in consistent units, we must first perform some conversion. The unit commonly used for tissue oxygen concentration is molarity (M = mol/L). Henry's law [226] may be used to convert oxygen concentration from mmHg to molarity. This law states that the amount of oxygen dissolved in a medium, S_O, is proportional to the pO_2,

$$S_O = pO_2\, s \tag{5.13}$$

where the constant of proportionality s is termed the oxygen solubility constant. For simplicity, we assume that in the RPMI medium used in our experiments, the parameter s takes the constant value 1.45 x 10^{-3} mol m^{-3} $mmHg^{-1}$ (35˚C) [216]. When converting from units of mol $cell^{-1}$ to mM, we estimate the typical DLD-1 cell volume, using a diameter of approximately 13 μm, under the assumption that a cell is perfectly spherical, to be equal to 1.15 x 10^3 μm^3.

Although the magnitude of the reduction in oxygen consumption by non-proliferating cells (δ) is likely to depend on the cell line and experimental setup, the

consensus is that such a reduction occurs. We conclude that typically we can expect a roughly 2- to 5-fold reduction in the rate of oxygen consumption in non-proliferating cells in comparison to their proliferating counterparts [35, 58, 59].

Parameter	Description	Value (original units)	Value (converted units)	References
D	Oxygen diffusion coefficient	1.46×10^{-5} cm^2 s^{-1}	1.46×10^{3} μm^2 s^{-1}	[224]
C_0	Oxygen concentration in medium	145 mmHg	0.21 mM	[193]
v	Maximal rate of oxygen consumption	7.16×10^{-17} mol cell^{-1} s^{-1}	6.22×10^{-2} mM s^{-1}	[57]
K	Effective Michaelis constant	4.64×10^{-3} mM	4.64×10^{-3} mM	[57]
δ	Non-proliferating cell oxygen consumption fraction	0.25	0.25	[59]
T	Typical time for cell division	24 h	86400 s	[227]

Table 5.3: Estimates for the parameters used in Models 1 and 2.

5.3.4 Non-dimensionalisation

Before solving each of our models, we non-dimensionalise them in order to reduce the number of parameters and to ensure that the solution does not vary over several orders of magnitude for ease of numerical solution. We rescale time with the typical time for cell

division *T*, radial coordinate with typical TS radius *R*, and oxygen concentration with its value in the medium, C_0. Substituting

$$t = T\hat{t}, r = R\hat{r}, C = C_0\hat{C} \tag{5.14}$$

into equation (5.8), we obtain

$$\frac{R^2}{DT}\frac{\partial \hat{C}}{\partial \hat{t}} = \frac{1}{\hat{r}^2}\frac{\partial}{\partial \hat{r}}\left(\hat{r}^2\frac{\partial \hat{C}}{\partial \hat{r}}\right) - \frac{R^2}{C_0 D}f(C_0\hat{C})\,. \tag{5.15}$$

Under this rescaling, the initial condition becomes

$$\hat{C}(\hat{r}, 0) \equiv 1, \tag{5.16}$$

for $0 < \hat{r} < 1$, and the boundary conditions become

$$\frac{\partial \hat{C}}{\partial \hat{r}}(0, \hat{t}) = 0, \qquad \hat{C}(1, \hat{t}) = 1, \tag{5.17}$$

for all $\hat{t} > 0$. Introducing new non-dimensional parameters

$$\varepsilon = \frac{R^2}{DT}, \quad \hat{v} = \frac{R^2 v}{DC_0}, \quad \hat{K} = \frac{K}{C_0}, \tag{5.18}$$

we obtain the equation

$$\varepsilon\frac{\partial \hat{C}}{\partial \hat{t}} = \frac{1}{\hat{r}^2}\frac{\partial}{\partial \hat{r}}\left(\hat{r}^2\frac{\partial \hat{C}}{\partial \hat{r}}\right) - \frac{\hat{v}\hat{C}}{\hat{C} + \hat{K}} \tag{5.19}$$

in the case of Model 1, and a similar equation, but with modified reaction term, in the case of Model 2.

Using the parameter estimates listed in Table 5.3, we can compute estimates for the non-dimensional parameters. We find the values ε = 1.98 x 10^{-3}, $\hat{v}$ = 58.382 and $\hat{K}$ = 2.21 x 10^{-2}. Based on these values, we conclude that, as $\varepsilon << 1$, we may apply a quasi-steady state approximation, simplifying equation (5.20) to the steady-state equation

$$\frac{1}{\hat{r}^2}\frac{\partial}{\partial \hat{r}}\left(\hat{r}^2\frac{\partial \hat{C}}{\partial \hat{r}}\right) = \frac{\hat{v}\hat{C}}{\hat{C}+\hat{K}}, \tag{5.20}$$

in the case of Model 1, and similarly for Model 2. This simplification is standard and its validity arises from the fact that the time-scale of oxygen diffusion into the centre of a TS is fast and much shorter than the time-scale of cellular division [53-56, 193, 228].

5.3.5 Numerical solution

In each of our models the PDE contains a reaction term that is nonlinear. We must therefore resort to a numerical method of solution. This involves discretizing in time and space to approximate the solution. As we applied a quasi-steady-state assumption we have a second-order ODE boundary value problem. Therefore, we could attempt to solve it numerically using a collocation method, such as that implemented in the Matlab inbuilt function *bvp4c*. However, such methods might not be accurate or efficient when applied to 'stiff' problems. 'Stiff behaviour', which refers to sharp transitions, occurs in our model because oxygen concentration drops rapidly when oxygen goes into a TS. In particular, such methods do not guarantee positivity of the solution, as is required when considering oxygen concentration and is in fact a property of the model equation for non-negative initial conditions. Therefore, we choose to solve the time-dependent problem to steady state in order to ensure positivity of the solution. We use the Matlab in-built function *pdepe*, which uses a second-order spatial discretization method to convert the PDE to a system of ODEs, which is then solved numerically, as described in [229]. In order to ensure that the solution has reached a steady state, we solve the time-dependent system until the current solution and the solution at the

previous time step differ by less than some small tolerance in magnitude. Having solved the system to steady state, we then re-dimensionalise all variables to visualize the results.

5.4 Results

5.4.1 The effect of cell size

Many of the parameters quoted in the literature differ by up to an order of magnitude. This can have a profound effect on model behaviour and, crucially, interpretation. Figure 5.1 shows the effect of varying cell size on the predicted profile of oxygen tension for a TS radius of 699 μm. Increasing cell size causes the distance from the TS surface at which we detect hypoxia (assumed here to be 10 mmHg [163, 230, 231]) and severe hypoxia (assumed here to be 0.8 mmHg [74]) to increase. Intuitively this makes sense, as we define oxygen consumption on a per cell basis. Thus, fewer cells in a TS will consume less oxygen. DLD-1 cells are approximately 13 μm in diameter [232], which corresponds to the onset of hypoxia, assumed here to be 10 mmHg, occurring at 88 μm from the TS surface.

We note that in order to calculate v, we use a parameter value taken from Casciari et al. [57] that is specified in units of mol $cell^{-1}$ s^{-1}. In order to convert from these to mM s^{-1}, we calculate a typical DLD-1 cell volume under the assumption that cells are perfectly spherical, using an estimate for typical DLD-1 cell diameter. We then divide the value provided by Casciari et al. [57] by our estimate of typical DLD-1 cell volume and use the fact that $1L = 10^{-3}$ m^3 to obtain an estimate for v in units of mM s^{-1}. There are a number of limitations

associated with using an estimate of cell diameter as an indication of the number of cells that are present in the given TS cross-sectional area. For example, cells might not be tightly packed, there might be large volumes of extracellular cell matrix which we neglect, and the size of a cell may not necessarily affect the overall oxygen consumption per unit of cross-sectional area. However, we maintain that using an estimate cell diameter appears the most appropriate way to estimate the value of v for DLD-1 TS in suitable units, as its value was unavailable in the reviewed literature.

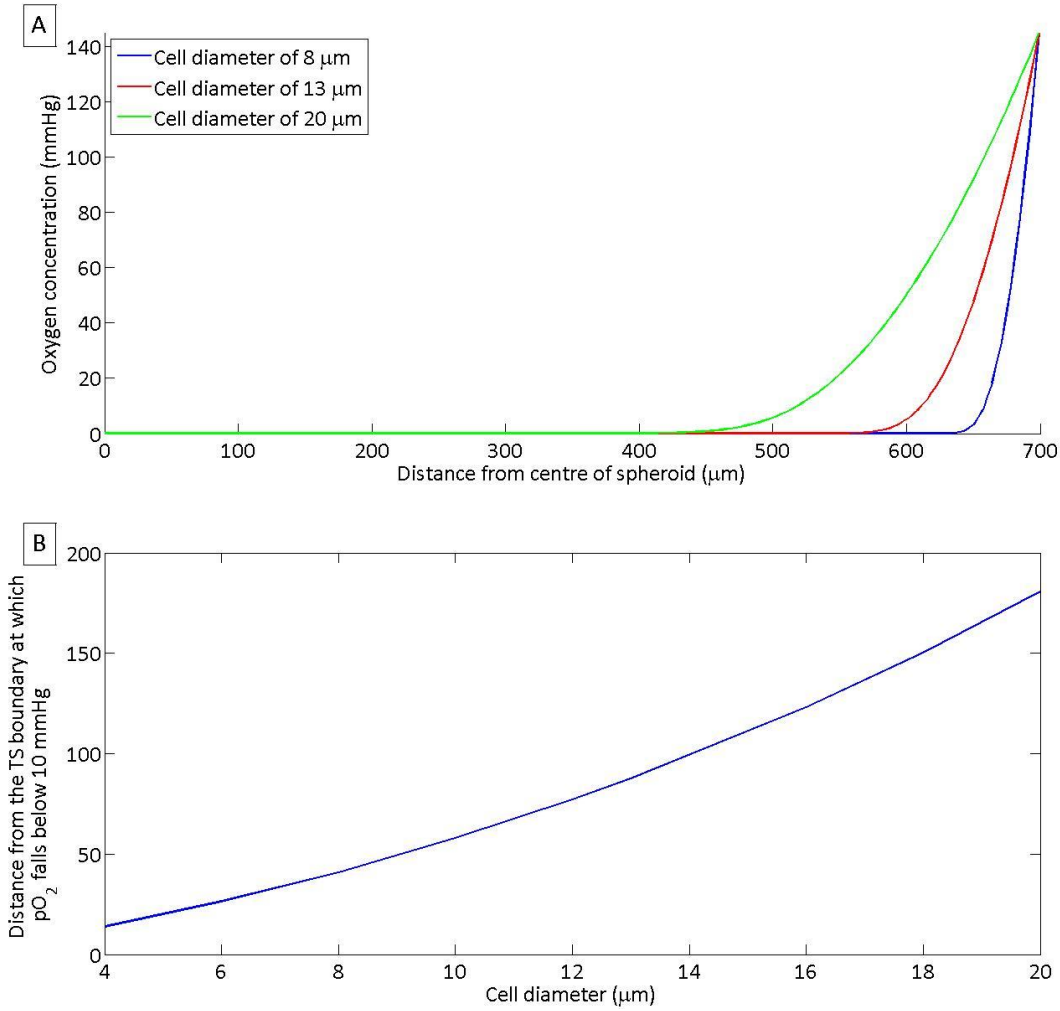


Figure 5.1: The effect of varying cell diameter on oxygen distribution within a TS of 699 µm. A) Oxygen distribution within a TS with a cell diameter of 8 µm, 13 µm and 20 µm. The pO_2 level at which we detect hypoxia (10 mmHg) is shown as a dashed line. B) Distance from the TS boundary in µm at which we detect hypoxia (pO_2 falls below 10 mmHg) increases with increasing cell diameter.

5.4.2 Estimation of parameter values for Model 1 and Model 2 suggests that oxygen consumption decreases during TS culture

To investigate the effect of increasing TS size on oxygen consumption, we estimated v by solving Model 1 and Model 2 with baseline parameter values and minimizing the sum-squared error between residuals of R_1 and R_2. We list the results in Table 5.4.

R [μm]	Model 1 v x 10^{-2} [mM s^{-1}]	Model 2 v x 10^{-2} [mM s^{-1}]
253	23.72	64.26
268	15.40	14.92
370	19.89	48.20
418	7.17	14.34
449	4.30	11.00
531	3.92	10.60
590	3.47	9.04
625	6.50	7.79
699	2.30	5.60

Table 5.4: Estimates for v for Models 1 and 2 and corresponding TS radii. Recall that baseline parameter value from the literature is v = 6.22 x 10^{-2} mM s^{-1}. The baseline parameter values used in Models 1 and 2 are described in Table 5.3.

Model 1 predicts that v decreases as the TS increases in size, in agreement with the experimental observations outlined in Section 5.1.1. We next investigate whether the proliferative heterogeneity which we detected in Chapter 4 would alter predictions of v. We find that Model 2 predictions of v also, in general, show a similar trend of a decrease in v with increasing TS radius. We note that Model 2 predictions of v are higher than corresponding values of v predicted by Model 1. As we allow non-proliferating cell fraction to consume oxygen at a lower rate than the oxygen consumption rate of proliferating cells

Model 2 predicts higher values of *v*. Our results predict a larger decrease in oxygen consumption (approximately 10-fold decrease predicted by Model 1 and approximately 12-fold decrease predicted by Model 2) than other studies reported in the literature. Freyer et al. [59] showed a 4-fold decrease in oxygen consumption rate in V-79 TSs between 100 and 200 µm radius. Mueller-Klieser [209] showed a 3-fold decrease in the rate of oxygen consumption in EMT6/Ro TSs between 195 and 500 µm radius. Both studies [59, 209] showed that cells in larger TSs underwent no further change in the rate of oxygen consumption, although the TSs continued to grow. Here, both Model 1 and 2 predict that TS cells are able to decrease the rate at which they consume oxygen throughout the entire period of TS growth. The predicted decrease in the rate at which TS cells consume oxygen suggest an increase in the oxygen diffusion limit. This would imply that the predicted oxygen gradient becomes shallower, favouring the survival of cells distal to the TS surface, with increasing TS size.

As the fractional decrease (*δ)* is likely to be having an effect on the *v* estimated in Table 5.4, we then hold the *v* constant and estimate *δ* throughout TS growth using Model 2. We list the results in Table 5.5. We find that the mean value of the ratio in oxygen consumption between proliferating and non-proliferating cells, *δ* (equal to 0.83), is higher than the value we selected for *δ* from the literature (equal to 0.25). Hence, Model 2 predicts that non-proliferating cells consume oxygen at approximately 83% of the rate of proliferating cells.

R [μm]	δ
253	1
268	0.85
370	0.99
418	0.99
449	0.62
531	0.6
590	0.47
625	0.99
699	0.99

Table 5.5: Estimates for δ for Model 2 and corresponding TS radii. Recall that the baseline parameter value which we chose from the literature was $\delta = 0.25$. The baseline parameter values used in Model 2 are described in Table 5.3.

5.4.3 Considering the effect of proliferation on oxygen consumption does not improve estimation of hypoxia

Using the image-derived boundaries of hypoxia and severe hypoxia, generated from EF5 staining in Chapter 4 (shown in Figure 5.2), as well as the diameter data from Chapter 3, we can use the model solution to estimate the oxygen tension at which binding occurs.

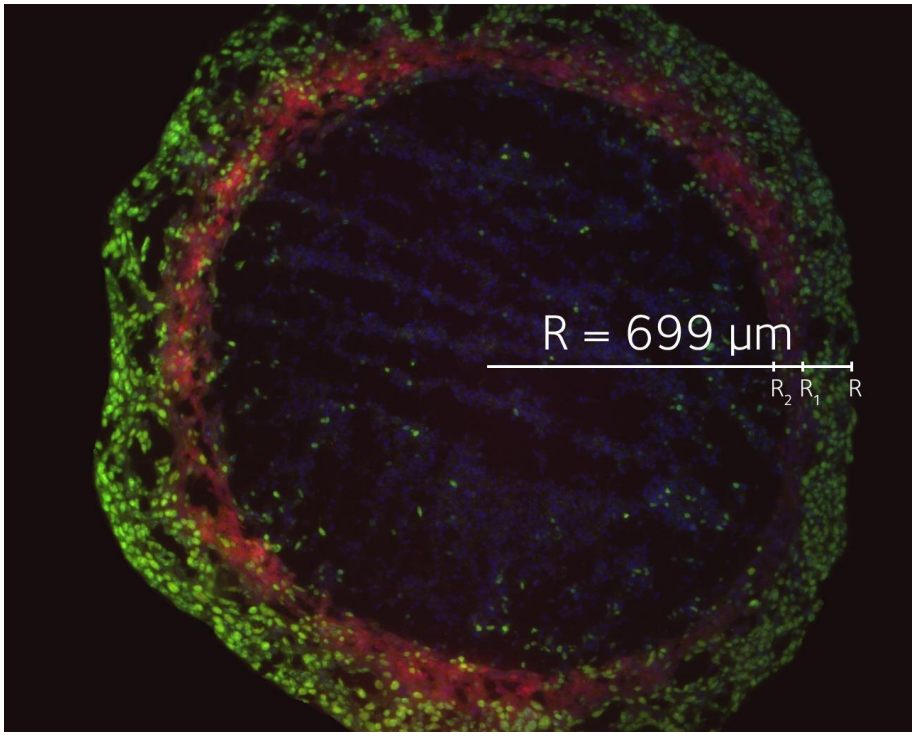


Figure 5.2: An example of a TS of 699 µm radius (R) taken at day 20 of growth. R_1 and R_2 denote radii of hypoxia and severe hypoxia, respectively, calculated using the image analysis methods described in Section 4.2.2.

By solving the model equations, we obtain the distribution of oxygen within a TS of the given radius (R), assign experimentally determined radii of hypoxia (R_1) and severe hypoxia (R_2) to compute the corresponding thresholds of hypoxia (C_1) and severe hypoxia (C_2) for Models 1 and 2.

In order to visualise the general behaviour of the solutions to Models 1 and 2, solutions for a single TS radius (R = 699 µm, day 20) are shown in Figure 5.3 A and B.

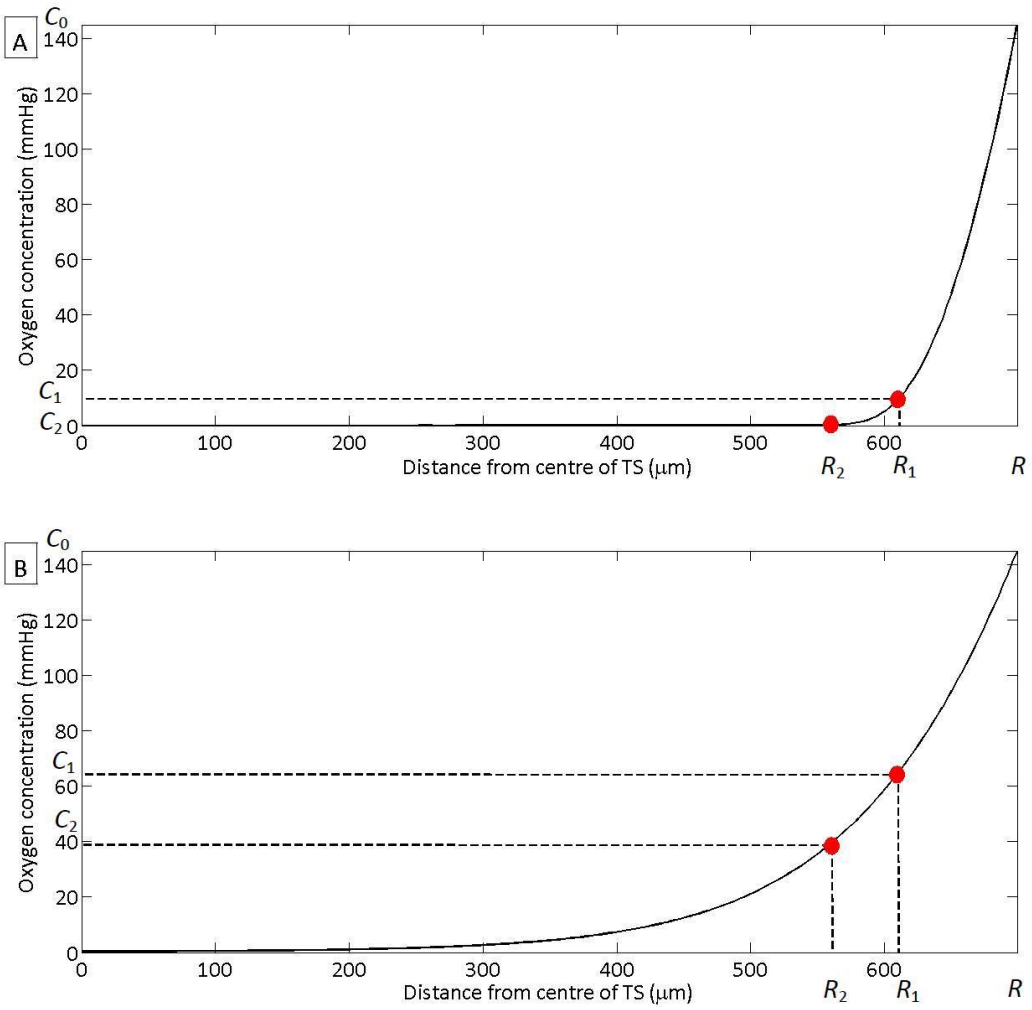


Figure 5.3: Steady-state distribution of oxygen as a function of the distance from the centre of a TS of specified radius 699 μm according to Model 1 (A) and Model 2 (B). A) Dashed lines represent estimated values for C_1 (equal 9.8 mmHg) and C_2 (equal to 0.17 mmHg) calculated for experimentally determined values of R_1 and R_2, according to Model 1 solved with baseline parameter values listed in Table 5.3. B) Dashed lines represent estimated values for C_1 (equal to 65.2 mmHg) and C_2 (equal to 39.3 mmHg) calculated for experimentally determined values of R_1 and R_2 and specified volume fractions $\alpha_N = 0.26$, $\beta_N = 0.74$, $\alpha_H = 0.16$, $\beta_H = 0.84$, $\alpha_S = 0.04$, $\beta_S = 0.96$ according to Model 2 solved using best-fit mean value of $\delta = 0.83$ and baseline parameter values listed in Table 5.3.

The most obvious difference between the two model solutions is that the oxygen gradient is far shallower when non-proliferative cells are assumed to consume less oxygen. This intuitively makes sense, since if the cells are consuming less oxygen, there will be more oxygen present to reach the inner regions of the TS. As the oxygen gradient predicted by

Model 2 is shallower than that predicted by Model 1, we find that the thresholds of hypoxia and severe hypoxia estimated by solving Model 2 are approximately 6-fold and two and a half orders of magnitude higher, respectively, than those thresholds estimated by solving Model 1.

In Figure 5.4 and Figure 5.5 we extend the above evaluation of single TS radius to include all TSs from Day 1 to 20, extracting the estimated thresholds for hypoxia and severe hypoxia for Models 1 and 2, respectively. Whilst there is variation in the thresholds across the time points, the general trend is that the predictions of the hypoxic thresholds (mean value of 11 mmHg $\approx$ 1.59 x 10^{-2} mM) and severely hypoxic thresholds (mean value of 7 mmHg $\approx$ 1.00 x 10^{-2} mM) made by Model 1 are closer to the literature-cited values than the predictions by Model 2 (shown in Figure 5.6). We observe that the Model 1 predictions of severely hypoxic threshold are approximately one order of magnitude higher than the literature-cited values. Hence, the Model 1 predictions imply that DLD-1 TS cells are sensitive to a reduction in oxygen levels and lose their viability at higher oxygen concentrations than those cited in the literature. We find that Model 2 predicts relatively high levels of oxygen at which we detect hypoxia (mean value of 32 mmHg $\approx$ 4.64 x 10^{-2} mM) and severe hypoxia (mean value of 24 mmHg $\approx$ 3.48 x 10^{-2} mM). As we obtained these predictions by solving Model 2 using the parameter values cited in the literature (listed in Table 5.3), and the mean value of δ estimated in Section 5.4.2, we conclude that considering the effect of proliferation on oxygen consumption does not improve the predictions of hypoxia and severe hypoxia in TSs.

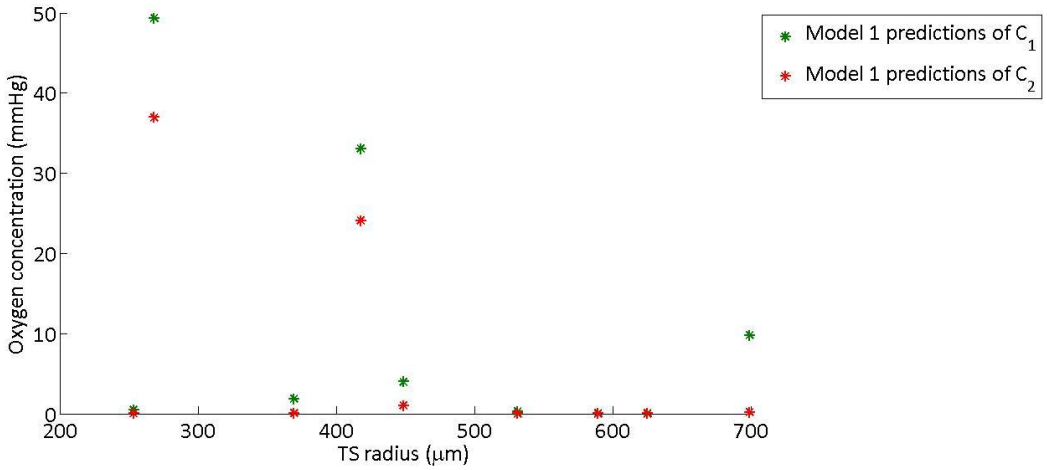


Figure 5.4: Model 1 predictions of the estimates for the oxygen threshold of hypoxia (C_1) and severe hypoxia (C_2) for different TS radii.

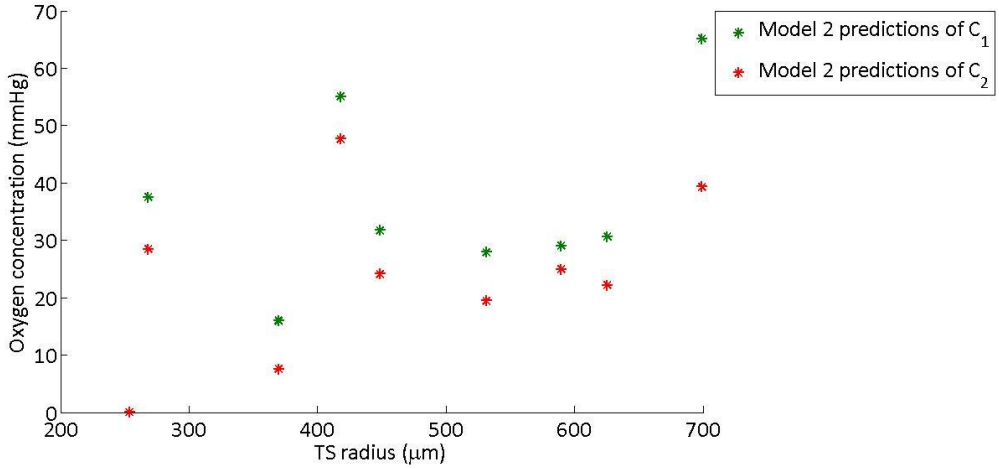


Figure 5.5: Model 2 predictions of the estimates for the oxygen threshold of hypoxia (C_1) and severe hypoxia (C_2) for different TS radii, the specified volume fractions obtained in Chapter 4 using baseline parameter values described in Table 5.3 and the mean best-estimate of δ = 0.83 calculated in Section 5.4.2.

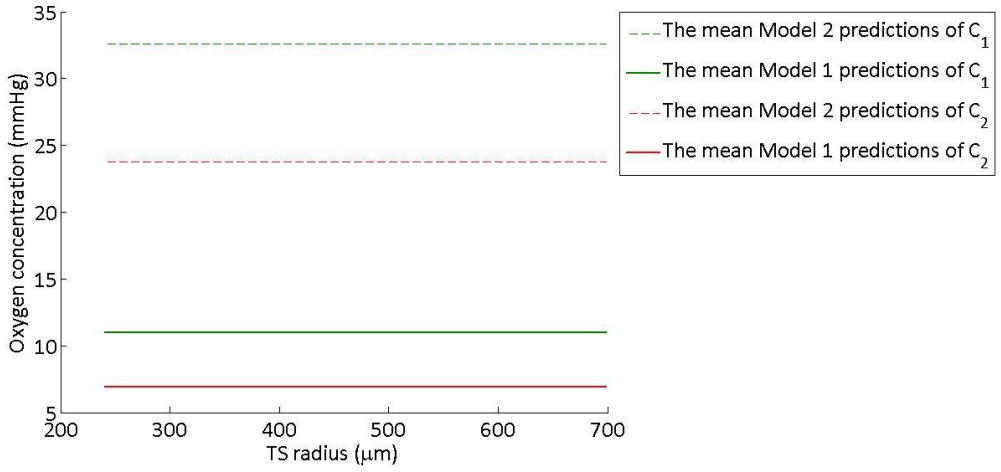


Figure 5.6: The mean Model 1 (solid line) and Model 2 (dashed line) predictions of the estimates for the oxygen threshold of hypoxia (C_1) and severe hypoxia (C_2).

5.5 Discussion

In this chapter, we investigated the role of oxygen consumption in prediction of oxygen distribution within TSs. By fitting a simple model of oxygen consumption (Model 1), which assumes that proliferation is uniform throughout the TS, to the hypoxia data generated in Chapter 4, we predicted a trend of decrease in rate of oxygen consumption (*v)* with increasing TS size. This supports the multiple experimental observations that oxygen consumption decreases as TSs increase in size or age (Section 5.1.1). In Table 5.1 we summarised a variety of estimates of *v* used in recent mathematical models and noted that there is a wide range of reported parameter values. Even though the oxygen consumption rate is frequently used in theoretical work, the fact that it is very variable is not adequately investigated and explained in the literature. Our findings support the need to consider the stage of cellular growth when defining the rate of oxygen consumption. Using oxygen

consumption rates derived from the exponentially growing TS could lead to large underestimations of the oxygen penetration distance.

When we estimated the fractional reduction in oxygen consumption exhibited by non-proliferating cells using Model 2 we showed that the magnitude of reduction selected from the literature (approximately 0.25) is likely to be overestimated. According to the predictions of Model 2, non-proliferating cells consume oxygen at approximately 83% of the rate that proliferating cells do and the magnitude of the reduction in oxygen consumption is maintained at various TS sizes.

Although Model 1 recapitulated experimental findings and detected hypoxia at oxygen levels similar to the ones available in the literature (mean value of hypoxic threshold equal to 11 mmHg) we were interested in understanding whether the proliferative heterogeneity observed within TSs in Chapter 4, could better explain the formation of hypoxia. Model 2 therefore incorporated a reduction in oxygen consumption within the fraction of non-proliferating cells. We showed that the oxygen distribution predicted by Model 2 was much shallower than that predicted with Model 1, suggesting that the reduction in oxygen consumption by non-proliferating cells promotes the oxygenation and survival of cells distal to the TS surface. However, using the chosen baseline parameter values and the best-fit estimated ratio δ of the rate of consumption to solve Model 2 predicted unrealistically high hypoxic (mean value of 32 mmHg) and severely hypoxic thresholds (the mean value of 24 mmHg). As EF5 is known to detect hypoxia at oxygen tensions below 10 mmHg [230, 231] with severe hypoxia developing below 0.8 mmHg [74] our Model 2 predicted much higher oxygen concentrations than those available in the literature. Thus, we conclude that either proliferative heterogeneity does not need to be

considered in predicting oxygen gradients within TSs, or that more sophisticated models are required.

Although the fact that we obtain a worse prediction upon including what would seem a biologically-plausible addition to our model, we must consider that our thresholds of 'hypoxia' and 'severe hypoxia' were defined arbitrarily based on EF5 signal intensity in Chapter 4. However, hypoxia can in fact be multiply defined, depending on the context. Incubation of HeLa cells at physiologically relevant oxygen concentrations in the range from 0 to 152 mmHg showed that HIF-1α and HIF-1β proteins each increased exponentially as cells were exposed to decreasing oxygen concentrations, with a half maximal response between 11 and 15 mmHg oxygen and a maximal response at 4 mmHg oxygen [233]. However, as we discussed in Section 4.1.3, HIF-1 expression can occur also in close proximity to blood vessels at higher than 38 mmHg pO_2 levels. In mice bearing ME180 and SiHa cervical cancer xenografts HIF-1α expression peaked at shorter distances from blood vessels than those detected with EF5 binding [234]. This suggests that HIF-1α regulation occurs at higher pO_2 levels than those required for EF5 binding. In terms of 'severe' hypoxia, Koch et al. [74] proposed that cell death is induced below oxygen concentrations of 0.8 mmHg, where EF5 binding is inhibited. Hammond et al. [235] showed that even though HIF-1α accumulates with similar kinetics at 0.15 mmHg and 15.2 mmHg oxygen in RKO cells (derived from colon carcinoma), p53 protein accumulates only below 0.15 mmHg. The accumulation of p53 protein in response to HIF-1 is suggested to be as a sign of the induction of cell death [236]. In another study Robiolio et al. [237] showed that mitochondrial function is reduced at pO_2 of less than approximately 0.5 mmHg [237] and below this threshold, cells lose their physiological function. Höckel and Vaupel [151] stated

that 0.02 mmHg of oxygen marks a critical oxygen level below which cytochromes are no longer fully oxidised which can lead to accumulation of ROS and ultimately cell death [238].

There are two main routes we can take to proceed with the present investigation. In Section 5.1.1 we briefly discussed the most advanced of the multiphase mathematical models that capture spatio-temporal dynamics of different cell populations within a TS during growth. In Model 2 the fractions of proliferating and non-proliferating cell types were the inputs derived from our experimental data set. If we would like to track the dynamics of changes in different cell types we would need to incorporate growth processes into our model.

The image analysis method developed in Chapter 4 allowed us to determine *discrete* fractions of proliferating and non-proliferating cell types in the specified regions of normoxia, hypoxia and severe hypoxia. Hence, the fractions of proliferating and non-proliferating cell types give no indication of the *continuous* spatial distribution of proliferating and non-proliferating cell types in a TS.

In both models of oxygen consumption considered in this chapter we made the simplifying assumption that oxygen is at steady state (as explained in Section 5.3.4) at any given TS radius. A natural next step emerging from the theoretical work presented in this chapter is to incorporate growth processes into the developed models. We have aimed to maintain an intermediate level of complexity. In Model 2 we defined seven new parameters, of which six were estimated from our own experimentally data (α_N, β_N, α_H, β_H, α_S, β_S) and one was estimated from the literature (δ). We believe that it would be unreasonable to introduce any further parameters into a model that is parameterised by the relatively small data set generated in Chapter 4. Adding more parameters and building a more detailed

mathematical model in this case is likely to result in overfitting, while the more extensive use of data from the literature obtained from other cell lines may not be appropriate as each cell line has unique metabolic characteristics. Hence, in order to progress to build a multiphase growth model that would capture the dynamics of changes in proliferating and non-proliferating cell types and metabolism during TS growth, we require more experimental data.

Overall, our mathematical modelling efforts in this chapter were aimed towards quantifying the relationship between cell proliferation and the rate of oxygen consumption and oxygen concentration. Using the results of TS proliferative heterogeneity we found in Chapter 4, we tested our hypothesis that changes in proliferation would affect TS oxygenation. We demonstrated that whilst this was true, the resulting predictions gave unrealistic results suggesting further refinement of the model is necessary.

Oxygen consumption is only one small piece of the puzzle of TS metabolism. In Section 5.1.1 we highlighted the enhanced contribution of glycolysis to metabolism in hypoxia. Determining changes in glycolysis throughout the entire TS growth process will allow for finer investigation of the association between cell proliferation behaviour and glucose metabolism. In Chapter 6 therefore, we will investigate the development of the glycolytic phenotype in TSs.

Chapter 6 Development of the glycolytic phenotype in TSs

In Chapter 5, mathematical modelling of oxygen distribution within TS showed that oxygen consumption is likely to decrease over the course of TS growth. As proliferation was maintained even in severely hypoxic regions until the end of TS culture, which was shown in Chapter 4, a decrease in oxygen consumption would likely be associated with increased glycolysis. In this chapter, the reliance of TS cells on glucose metabolism over TS growth was experimentally evaluated. The central role of glucose was investigated in the context of changes in glucose and lactate levels in TS medium, expression, activity and regulation of the most important glycolytic enzymes, including HKII, PFK-1, PKM2, and LDH-V. Expression of these enzymes and their relationship with the HIF-1α oxygen sensor was analyzed throughout the entire period of TS growth. Finally, changes in the spatial distribution of HKII and LDHV expression throughout TS growth were analyzed. Figure 6.1 presents a general description of glycolysis and the reactions catalysed by those enzymes that were chosen for this study.

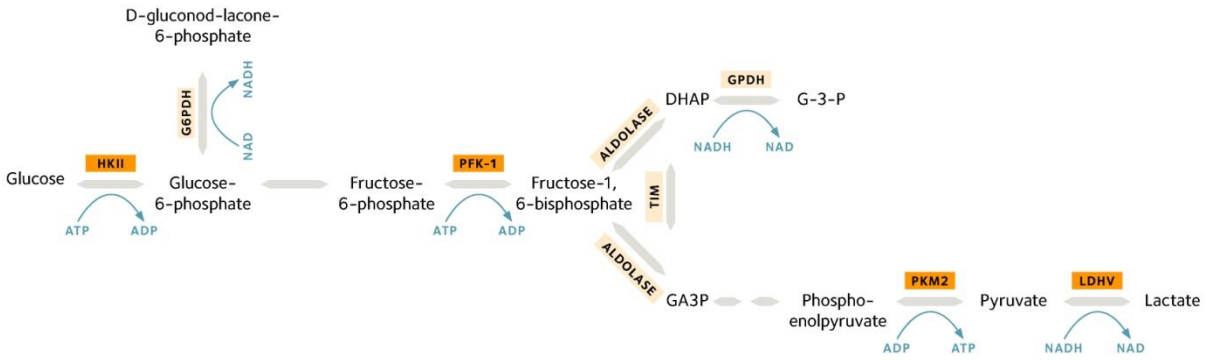


Figure 6.1: General description of the glycolytic pathway. Enzymes that were measured in this study are highlighted in orange. The diagram shows the reactions catalyzed by HKII, PFK-1, PKM2 and LDHV which were described in detail in Section 6.1.3.

6.1 Introduction

6.1.1 The central role of glucose consumption in tumour metabolism

In the 1920s, Otto Warburg famously observed that cancer cells consume approximately 10-times more glucose than normal cells [239]. Initially, Warburg proposed that this was due to dysfunctional mitochondrial function. However, it is now known that the increased reliance on glycolysis exhibited by most cancer cells is not a result of dysfunctional mitochondria, but rather of active metabolic reprogramming directed by the activation of oncogenes, such as Akt and Myc, that are known to support tumour growth [240, 241]. Hence, the Warburg effect, or 'aerobic glycolysis', is now considered an adaptive metabolic phenomenon that has been confirmed to be a common feature of the majority of cancer cells [240].

Activation of the PI3K/Akt pathway is the most common alteration found in human cancers. Activated PI3K/Akt results in enhanced glucose uptake and glycolysis [242, 243]. A schematic representation of the mechanism by which Akt stimulates aerobic glycolysis in cancer cells is shown in Figure 6.2. Akt induces increased expression of the glucose transporter (GLUT-1) on the cell surface, which facilitates glucose uptake and allosterically activates key-glycolytic enzymes to optimise glucose degradation [84, 244, 245]. For example, Akt promotes the association of HKII with mitochondria, which increases its activity [84]; it also directly phosphorylates PFK-2, which enhances the activity of PFK-1 [244].

Akt signalling may also increase glycolytic flux indirectly, by transcriptionally up-regulating the endoplasmic reticulum enzyme ENTPD5 [246]. ENTPD5 promotes proper protein glycosylation and folding through a cycle of reactions coupled to ATP hydrolysis. It was shown that Akt upregulates the expression of ENTPD5, which can increase the cellular ADP:ATP ratio. As ATP is the primary inhibitor of PFK-1, an increase in the ADP:ATP ratio activates PFK-1.

In addition to stimulating aerobic glycolysis, the PI3K/Akt pathway facilitates the flux of glucose carbon in the form of pyruvate towards the biosynthetic pathways, which rely on mitochondrial metabolism. Various biosynthetic reactions require a supply of cytosolic acetyl-CoA, which is the building block required for lipid synthesis, including the production of fatty acids and isopentenyl pyrophosphate. Pyruvate is imported into the mitochondrial matrix, where it is decarboxylated to acetyl CoA and further condensed with oxaloacetate by citrate synthase to form citrate. Citrate can be oxidised through the TCA cycle or exported to the cytosol. ATP-citrate lyase (ACL) can convert the cytosolic citrate to form acetyl CoA and

oxaloacetate. Akt promotes shifting of mitochondrial citrate from the TCA cycle to acetyl-CoA generation by activating ACL [247]. Citrate is a very potent negative allosertic inhibitor of glycolysis, which, for example, inhibits the activity of PFK-1 [248]. Hence, citrate degradation by ACL is crucial for preventing the accumulation of citrate in the cytoplasm, which allows for aerobic glycolysis.

The mTOR protein, which is downstream of PI3K/Akt, is known for enhancing protein synthesis. mTOR assembles into two distinct multiprotein complexes called mTOR complex 1 (mTORC1) and mTORC2. mTOR1 is crucial for tumourigenesis, as the majority of cancers rely on biosynthetic reactions rather than an exogeneous supply of the building blocks needed for protein synthesis. mTORC1 promotes transamination (where an amine group is exchanged for a keto group of the other molecule), which is necessary for *de novo* protein synthesis of mitochondrial intermediates, such as conversion of oxaloacetate to generate aspartate, which is a precursor of asparagine, and conversion of α-ketoglutarate to glutamate, which in turn can be converted to proline, arginine and glutamine. The primary mechanism through which mTORC1 promotes mitochondrial biogenesis is through the transcriptional complex that promotes the function of PGC-1α [249].

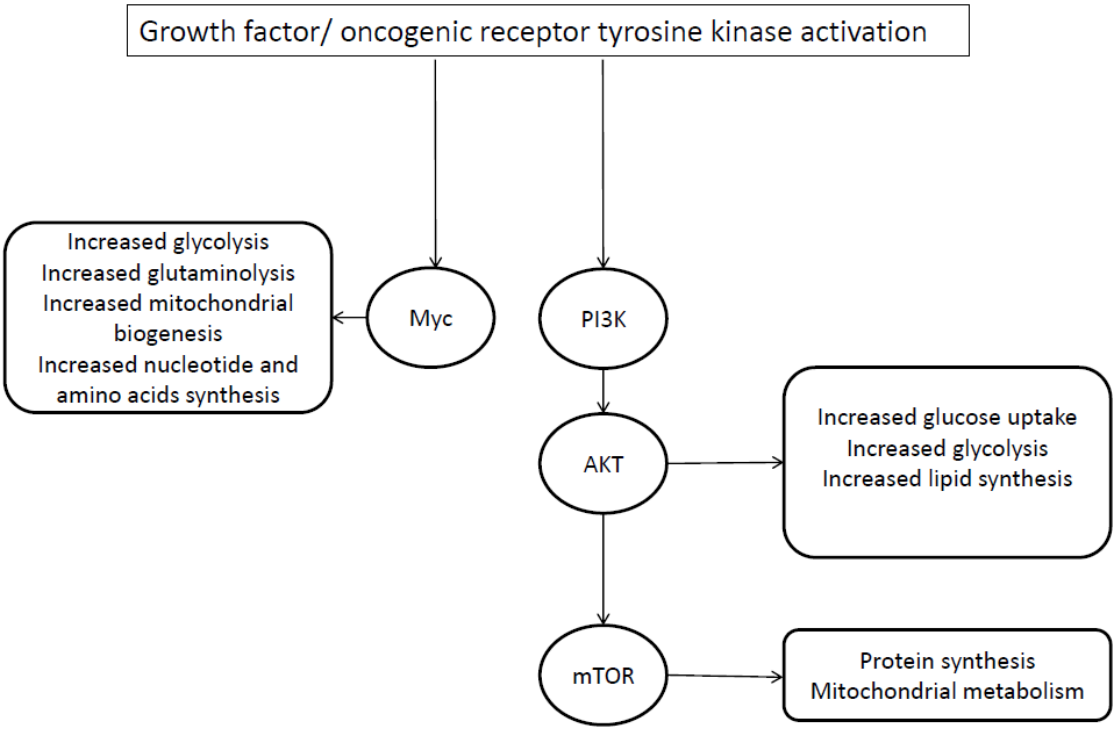


Figure 6.2: Schematic representation of alterations in oncogenes that directly reprogram cell metabolism to increase glucose uptake and increase flux through glycolysis. Akt also promotes the conversion of mitochondria-derived citrate to acetyl-CoA for lipid synthesis. mTOR promotes protein synthesis and mitochondrial metabolism. Myc increases glucose consumption through increased expression of glycolytic enzymes and glutamine uptake and consumption. Myc also promotes mitochondrial biogenesis and nucleotide and amino acid synthesis.

The ATP required for normal cell proliferation and survival comes primarily from two sources. The first is glycolysis, which comprises a series of reactions that metabolizes glucose to pyruvate in the cytoplasm to produce a net of 2 ATP from each molecule of glucose. The other is oxidative phosphorylation which, by using electrons donated by NADH and $FADH_2$ generated during the TCA cycle, generates a proton gradient of which the dissipation through ATP synthase forms 36 ATP per glucose molecule [248, 250]. Even though total energy production in terms of ATP synthesis is low in comparison to oxidative phosphorylation, flux through glycolysis in proliferating cells can be increased to exceed the

energy that is produced via oxidative phosphorylation [251]. An additional possible advantage of using glycolysis as a primary nutrient for proliferation includes independence from oxygen. Moreover, reliance on glycolysis spares the cell from the production of harmful ROS, which are generated during oxidative phosphorylation [26].

The Myc oncogene, which contributes to the genesis of many human cancers, encodes the transcription factor c-Myc, which links altered cellular metabolism to tumourigenesis. c-Myc regulates genes involved in the biogenesis of ribosomes and mitochondria and in the regulation of glucose and glutamine metabolism. In cell culture experiments, when glutamine is withdrawn from the culture medium, cells that express oncogenic Myc undergo apoptosis. Hence, the viability of cells with oncogenic Myc depends on the availability of glutamine as a carbon source for mitochondrial metabolism [252]. Myc increases the expression of genes involved in both glycolysis (such as LDHV) and glutaminolysis (such as glutaminase (GLS) protein) [253].

The reliance of cancer cells on glucose consumption does not mean that other nutrients are not utilised. Cancer cells may use oxidative phosphorylation for ATP production or can readily switch between aerobic and anaerobic metabolism depending on the availability of glucose in their environment. Cancer cells are known to rely on glutamine consumption as a major energy source [254]. Glutaminolysis can generate a sufficient amount of energy in the presence of oxygen, and provide intermediates that can be shifted towards biosynthetic reactions, to ensure cell survival and growth [255]. Lactate has also been proposed to be a source of cellular energy for some cancer cells [256].

6.1.2 Glycolysis and proliferation

Upregulated cell proliferation provides a platform necessary for neoplastic progression [257]. Due to the fact that proliferating cells have to duplicate all their macromolecular components in order to divide, the anabolic demand of proliferating cells for the synthesis of lipids, proteins, nucleic acids and ATP is very high. As glucose can be used to generate cellular bioenergy and its intermediates can stimulate glucose-dependent macromolecular biosynthesis, an increased flux though glycolysis enables proliferation [247].

The Warburg effect is associated with increased proliferation of cancer cells by promoting the accumulation of glycolytic intermediates, which can be shifted towards biosynthetic reactions [25, 27]. The pentose phosphate pathway uses the products of glycolysis to generate ribose-5-phosphate, which is needed for nucleotide synthesis.

The establishment of a proliferative metabolism depends primarily on the reprogramming of mitochondria to serve a synthetic rather than a degradative function. Oncogenic mutations in proto-oncogenes and tumour suppressor genes play a major role in the metabolic regulation of proliferation. For example, activation of oncogenes such as Ras, induces the expression of specific isoforms of metabolic enzymes that favour the proliferating phenotype in cancer cells [258]. Additionally, metabolic enzymes can be alternatively spliced to the isoforms that promote cell proliferation. For example, Mazurek et al. [254] showed that proliferating cells exclusively express the PKM2 isoform of pyruvate kinase. Christofk et al. [259] further analyzed PKM2 expression in the xenograft nude mouse model and showed that PKM2-expressing cells have a growth advantage over PKM1-expressing cells. Cells that expressed the PKM1 isoform were found to have a reduced ability

to form tumours, reduced lactate production and increased oxygen consumption in comparison to PKM2-expressing cells.

Cell proliferation is not only linked to high glucose consumption rates. Studies have shown that some cell lines, such as MDA-MB-453 [260] and HepG2 cells (a hepatoma cell line) [261], are able to proliferate at low glucose levels. This is possible when the reduced amount of glucose available is primarily used for synthetic processes. When Novikoff rat hepatoma cells were cultured at low glucose concentrations (up to 0.5 mM glucose), glucose was used exclusively for macromolecular synthesis without the production of lactate [262]. When the glucose carbons are mainly used for synthesis of cell building blocks another source of energy regeneration is necessary, which, in the case of the proliferating tumour cells, is glutamine. For example, when MDA-MB-453 cells were cultured in reduced glucose concentrations (0.5 mM glucose) there was an 8-fold increase in glutamine consumption rates in comparison to cells cultured in 5 mM glucose [260]. In other work, Rossignol et al. [263] showed that HeLa cells can adapt their mitochondrial network structurally and functionally to derive energy solely through glutaminolysis.

The central role of increased glucose consumption in most tumour types raises the question of how the metabolic flux is distributed between the main bioenergetic pathways in solid tumours. The relative contribution of each pathway to tumour bioenergetics is not easily defined as it is a metabolic characteristic which can vary between tissue types. Full characterisation of the tumour metabolome would require a detailed understanding of gene expression, enzyme kinetics and metabolic flux [264].

6.1.3 Glycolytic enzymes and cancer

The importance of glycolysis for cancer metabolism is manifested by the fact that genes which encode for key glycolytic proteins are overexpressed in more than 70% of human cancers [265]. The glycolytic flux is not controlled by a single enzyme [266]: enhanced glycolysis in tumour cells is a result of the increased expression and multisite modulation of a number of glycolytic enzymes [266]. Enzymes which catalyse irreversible reactions of glycolysis include HK, PFK, PK and LDH [267]. In particular, they catalyse the four irreversible steps of glycolysis (as presented in Figure 6.1), including the initial, intermediate and final steps of the pathway. These enzymes therefore serve as the control sites and determine the rate of glycolytic flux [268-272].

HK

HK catalyses the first step in glycolysis and is greatly overexpressed in the majority of cancer cells [80, 81]. There are four major isoenzymes of HK, named Types I, II, III and IV (the latter also known as glucokinase) [273, 274]. Types I-III have a high affinity for glucose (Km = 0.02-0.03mM) and a similar molecular mass of around 100 kDa [275]. Conversely, the Type IV isoenzyme has a lower affinity for glucose (Km = 5-8mM) and half the molecular mass of types I-III. Sequence analysis of HK isoenzymes has revealed that the most prevalent isoenzyme present in tumours that exhibit increased glycolytic phenotype is HKII [275]. Even though the underlying molecular mechanisms resulting in an increased glycolytic phenotype of solid tumours involve a number of events, one of the most important characteristics of these tumours is the overexpression of HKII [82-84].

The main mechanism by which HKII activity is reduced is via product inhibition. Over-production of glucose-6-phosphate (G-6-P) strongly inhibits HKII activity in fast-growing tumours [80]. The over-expression and enhanced activity of HKII contribute towards a high glycolytic flux and reduced apoptosis, the latter indicating the importance of glycolytic metabolism in promoting cell survival in solid tumours.

PFK

PFK catalyses the phosphorylation of fructose-6-phosphate to fructose-1,6-bisphosphate. There are two main types of PFK, called PFK-1 and PFK-2. PFK-1 activity has been shown to be greatly increased in neoplastic tissues compared to normal tissues of the same type, and is also significantly higher in metastatic tumours than in non-metastatic tumours [276]. In mammalian cells, PFK-1 is a tetramer composed of three isoforms, whose activity is influenced by many allosteric regulators [277, 278].

PFK-1 is allosterically activated by fructose-2,6-bisphosphate (F-2,6-BP) [279]. Hence, the enzymes which control the concentration of F-2,6-BP serve as the most important regulators of PFK-1 activity and glycolysis. The formation of F-2,6-BP is, in turn, regulated by PFK-2. Breakdown of F-2,6-BP to fructose 6-phosphate is hydrolysed by a fructose bisphosphatase 2 (FBPase2). Both the PFK-2 isomer and FBPase2 are present in a single polypeptide chain, which has a bi-functional role: it has the ability to both break down F-2,6-BP (in the phosphatise domain) and induce its formation (in the kinase domain) in the presence of cyclic adenosine monophosphate (cAMP). Hence, if glucose levels are low, increased levels of the hormone glucagon lead to activation of cAMP, which through a cascade of events activates FBPase2 and inhibits PFK-2. Thus, the concentration of fructose-2,6-bisphosphate is lowered, promoting a decrease in the glycolytic rate. When the levels of

glucose increase, PFK-2 is activated and FBPase2 inhibited, leading to an increase in the levels of fructose-2,6-bisphosphate and promotion of glycolysis [267].

In addition, the affinity of PFK-1 for its substrate fructose-6-phosphate is reduced by high levels of ATP. This enables PFK-1 to detect the energetic state of a cell and respond appropriately to meet its bioenergetic needs. AMP reduces the inhibitory effect of ATP by activating PFK-1 to stimulate glycolysis as the energy ratio of ATP/AMP is low. Citrate enhances the inhibitory effect of ATP. Inhibition of PFK-1 by citrate means that carbon from glycolysis is shuttled into various biosynthetic processes instead of feeding oxidative phosphorylation [248].

PK

PK catalyses the third irreversible step in glycolysis, in which pyruvate is formed from phosphoenolpyruvate (PEP). The PK reaction generates one molecule of ATP via substrate-level phosphorylation and is responsible for net ATP production. In contrast to oxidative phosphorylation through pyruvate kinase, glycolysis allows for ATP generation and enables survival independently of oxygen supply. As PEP is the most energy-rich phosphometabolite, the reaction favours dephosphorylation of PEP and production of ATP [254].

There are several isoenzymes of PK, with individual expression dependent on the metabolic requirements of the tissue type. Pyruvate kinase M2 (PKM2) is expressed in lung tissues, tumour cells and other proliferative cells with high rates of nucleic acid synthesis. PKM2 can exist in a highly active tetrameric form, which is expressed in non-malignant tissues (such as lung tissue), and an inactive dimeric form, which is usually a characteristic of malignant cells [280]. Furthermore, the amount of dimeric form in tumour cells is correlated with the degree of tumour malignancy [281]. PKM2 is consistently expressed in tumour

cells, with IHC analysis demonstrating that during tumour formation, tissue-specific PK isoforms disappear and are replaced by PKM2 [282]. PKM2 dimerization is induced by direct interaction of PKM2 with certain oncoproteins [280]. Dimeric and tetrameric PKM2 differ significantly in their kinetic properties. Tetrameric PKM2 has a high affinity for PEP: the PK reaction can readily proceed and formation of pyruvate and ATP is favoured. In contrast, dimeric PKM2 has a low affinity for PEP, which leads to the accumulation of glycolytic intermediates, thus reducing pyruvate formation [34]. The accumulation of glycolytic intermediates, such as PEP, glycerate 3-P, glyceraldehyde 3-P, fructose 1,6-P_2, ribose-5P and 5-ribose-PP, is beneficial for cell division, as these metabolites can be further shuttled into processes such as nucleic acid, amino acid and phospholipid synthesis [281]. Consequently, the presence of the dimeric PK isoform in malignant cells favours a proliferating cancer phenotype.

Although the presence of the dimeric form of PKM2 is beneficial for the accumulation of glycolytic phosphometabolites, constant inhibition of PKM2 activity would lead to nutrient starvation and energy depletion, which would eventually lead to cell death. Therefore, the ratio of tetramers to dimers is not constant, but fluctuates depending on a cell's bioenergetic needs. One of the main factors regulating association of the highly active tetrameric form is fructose-1,6- bisphosphate, the product of the PFK-1 reaction. Above a certain threshold, fructose-1,6- bisphosphate causes PKM2 dimers to associate and form a tetrameric form [280]. Subsequently, glucose can be fully catabolised and converted to lactate until the level of fructose-1,6- bisphosphate falls below a minimum threshold of PKM2 tetramer formation.

In addition to components of the glycolytic pathway, various amino acids play an important role in regulating PKM2 activity. L-serine is an allosteric activator of PKM2, which increases its affinity for PEP and lowers the minimum fructose-1,6- bisphosphate threshold necessary to induce PKM2 tetramerization [281]. In contrast L-alanine, which is a glutaminolytic intermediate, lowers PKM2's affinity for PEP and increases the minimum fructose-1,6- bisphosphate threshold necessary to induce PKM2 tetramerization. In addition to L-serine, various other amino acids such as l-cysteine, l-methionine, l-phenyalanine, l-valine, l-leucine, l-isoleucine and l-proline can allosterically inhibit PKM2 activity [283]. Fatty acids can also inhibit PKM2 activity [284].

Overall, PKM2 acts as a metabolic sensor, which allows for adaptation to varying nutrient supply by shifting between active and inactive forms and, through ATP generation, enables survival in hypoxic conditions.

LDH

LDH catalyses the reduction of pyruvate to lactate, a crucial checkpoint in the switch from aerobic to anaerobic glucose metabolism. LDH isoforms exist as tetramers, composed of two main subunits, M and H proteins, which are encoded by LDH-A and LDH-B genes. An increased number of M subunits over H subunits leads to enhanced efficiency in catalysing the conversion of pyruvate to lactate, thus favouring anaerobic glycolysis [86]. On the other hand, an increase in H subunits favours the conversion of pyruvate to acetylCoA, which subsequently enters the TCA cycle, favouring aerobic metabolism [86]. In humans, five major isoforms of LDH have been found, each made up of different combinations of the two protein subunits. In highly malignant and hypoxic carcinomas, the most prevalent is the LDHV isoform, which is absent from normal epithelia but extensively expressed in cancer

cells and is linked with tumour hypoxia and poor prognosis [22, 86]. The LDHV isoform is the most efficient LDH isoform in catalysing the conversion of pyruvate to lactate [85]. It is made up entirely of M protein subunits, regulated by the LDH-A gene, which favour anaerobic glycolysis over oxidative phosphorylation. Primary regulators of the LDH-A gene include HIF-1 [22], estrogen [285], cyclic AMP [286] and c-Myc [287]. Expression of the LDHV isoform has been directly linked with HIF-1 overexpression in colorectal cancer and its levels have been associated with metastasis, prediction of tumour aggressiveness and post-operative prognosis [85].

Recently, Leite et al. [288] identified lactate as one of the factors that can inhibit activity of HKII and PFK-1. Furthermore, some groups have promoted the hypothesis that lactate is not only a waste-product of anaerobic glycolysis, but can also take part in regulation of metabolism [289, 290].

6.1.4 HIF-1 as a modulator of glycolysis in tumour cells

Hypoxia-inducible genes whose transcription is upregulated by HIF-1 include those encoding glycolytic enzymes. A schematic representation of HIF-1 mediated glycolysis is shown in Figure 6.3. The HIF-1 transcription factor, which is stabilized under hypoxia, is the primary driving force for increased glycolysis in tumour cells, regulated by increased transcription and translation of HKII, PFK-1, PKM2 and LDHV isoforms of key-glycolytic enzymes [154, 155]. HIF-1 also reduces the rate of pyruvate entry into the mitochondria by promoting the expression of the PDK [26, 291]. PDK phosphorylates PDH, inhibiting it from using pyruvate

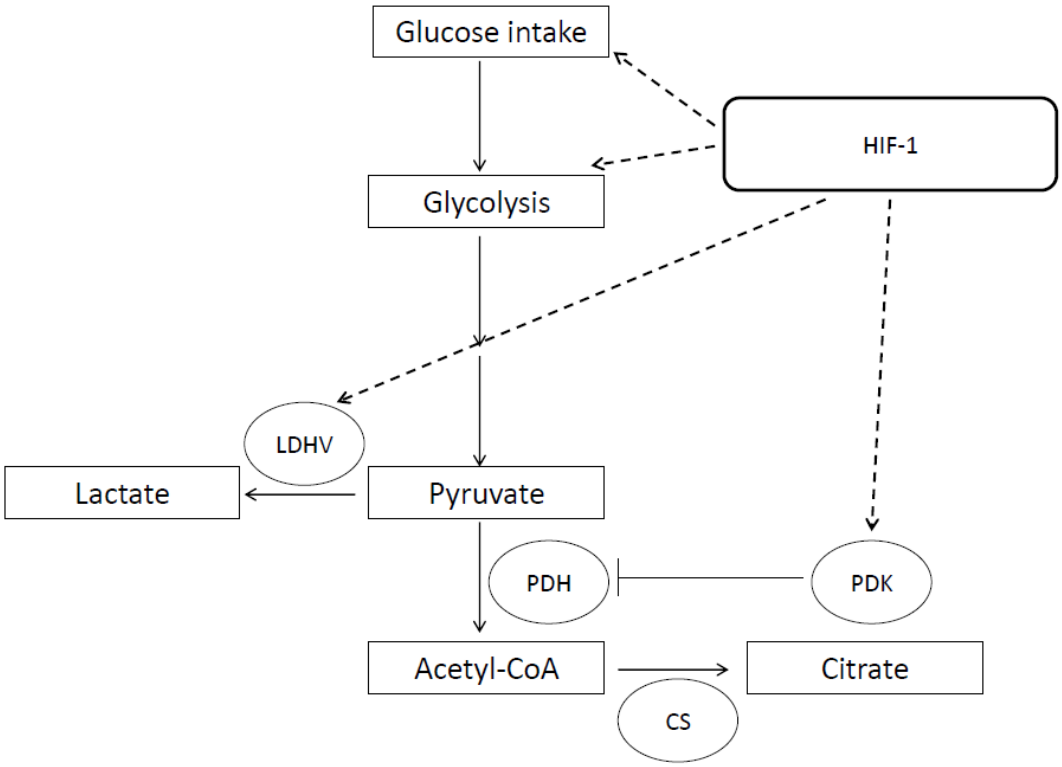


Figure 6.3: Schematic representation of HIF-1 action, which promotes the expression of genes encoding glucose transporters and most enzymes of glycolysis (showed as the dashed lines). HIF-1 also inhibits glucose carbon flow into the mitochondria by promoting the expression of pyruvate dehydrogenase kinase (PDK) which inhibits pyruvate dehydrogenase (PDH). In addition, HIF-1 upregulates LDHV expression to increase the conversion of pyruvate to lactate. This conversion regenerates the ratio of NAD^+/NADH necessary for continued flux through glycolysis. By inhibiting PDH, the level of acetyl-CoA is reduced and the conversion to mitochondrial citrate by citrate synthase (CS) is blocked.

to fuel the mitochondrial TCA cycle. By diverting pyruvate into lactate, HIF-1 blocks glucose carbon incorporation into mitochondrial citrate [33].

Increased metabolic dependence on glucose metabolism for energy production has been suggested to confer a growth advantage for cells located in hypoxic areas of tumours [292]. However, most of the data on the effects of HIF-1α on cell survival come from monolayer cultures [61, 293]. HIF-1α deficient cells had a reduced growth rate and survival when cultured in hypoxic conditions supplied with glucose in monolayer cultures in

comparison to wild type cells [293]. Moreover, it was shown that cells lacking HIF-1α had a reduced growth rate and survival only when glucose supply was limited [293]. This suggests that the HIF-1α-mediated proliferative response is glucose-dependent.

Even though HIF-1α is stabilized in hypoxia and degraded in normoxia, in some cancers it is activated even in well-oxygenated regions [294]. The oxygen-independent mechanisms responsible for upregulation of HIF-1 and HIF-1α were discussed in Section 4.1.3. Studies in monolayers [254, 275, 276, 295] cultured in normoxic conditions showed overexpression of both key-glycolytic enzymes and HIF-1 in cancer cells in contrast to their healthy counterparts. Other studies found that tumour cells become hypersensitised to glycolytic inhibitors when cultured in hypoxic conditions [206, 207] and inhibition of glycolysis can effectively kill cancer cells in reduced oxygen conditions. Whilst the manipulation of single-layer cells is easy, the monolayer culture is not very realistic at reproducing the tumour microenvironment, as described in detail in Section 4.1.4. The multicellular TS model offers an alternative. Kim and Forbes [110] analysed the effects of HIF-1α on TS metabolism by comparing wild-type and HIF-1α deficient TSs. The authors classified TSs into three groups: small wild type TSs (mean diameter of 275 μm), large wild-type TSs (mean diameter of 809 μm) and large HIF-1α deficient TSs (mean diameter of 839 μm). They showed that glucose consumption decreased in large wild-type TSs as measured in terms of reduced extracellular fluxes, and calculated intracellular fluxes in comparison to their small counterparts. Additionally, there was no difference in glucose metabolism in large wild-type and HIF-1α deficient TSs. Making the assumption that small TSs consisted predominantly of proliferating cells and large TSs of both proliferating and quiescent cells, the authors attributed the observed decrease in glucose consumption per viable TS cell in

large TSs to accumulation of non-proliferating cells during TS growth. Thus, the authors showed that glucose gradients limit the effects of HIF-1α. Hence, cell survival and intracellular metabolism were similar in wild-type and HIF-1α deficient TSs. This is in agreement with data from monolayers presented by Seagroves et al. [292].

Working with the EMT6/Ro cells, Freyer and co-workers [58] showed that glucose consumption per viable TS cell was reduced 2.5-fold in TSs of diameter 1300 μm compared with those of up to 150 μm in diameter. Recently, Rodríguez-Enríquez et al. [35] showed that expression of HKII increased 2.5 times in 'old' Hela and Hek293 TSs in comparison to their 'young' counterparts. Additionally, the authors [35] revealed that HIF-1α content increased 3.3-fold in HeLa and Hek293 TSs with TS age. Thus, the authors concluded that glycolysis is the primary pathway in Hela and Hek293 TSs. It should be noted that the authors determined the flux through glycolysis by measuring the overall rate of lactate production, which may be misleading, as increased lactate production might reflect both increased glucose and glutamine consumption [254]. The results presented by Khaitan et al. [293] showed that glucose consumption and lactate production per viable BMG-1 (cerebral glioma cell line) TS cells increased 2-3 times in old TSs and HIF-1α content increased between two examined data points (the magnitude of increase was not specified).

In summary, it has been observed [35, 293] that TSs of different ages vary in glucose metabolism, but how changes in glycolytic and hypoxic markers develop during TS growth remains unclear (the authors in the aforementioned studies analyzed only the end points of TS culture time). Some authors have shown that glycolysis increased with increasing TS size [35, 293], while others observed a decrease in large TSs in comparison to their young counterparts [58, 110].

Increased glycolysis of cancer cells, even in the presence of oxygen, is one of the best-known alterations that enables them to dynamically adjust their metabolism in order to maintain the ability to proliferate, grow, metastasize and survive [27, 294]. While previous experimental investigation of the Warburg effect has been able to associate this with several key prognostic factors of solid tumour description, such as a more aggressive tumour phenotype [295-297], development of resistance to apoptosis [298, 299], the generation of biosynthetic precursors for proliferation [25, 27] and increased metastatic potential [300], no study has yet provided a basic biochemical description of the enzymes that catalyse the key regulatory reactions of glycolysis throughout the entire period of TS growth.

6.2 Aim of this work

Despite almost a century of research since Warburg first proposed his hypothesis of aerobic glycolysis of cancer cells, understanding of the development of the glycolytic phenotype in cancer cells remains limited. Increased glucose consumption and glycolysis could be viewed as a prominent biochemical phenomenon of cancer cells that reflects a fundamental change in their energy metabolism. Large amounts of data from monolayer studies suggest that glycolytic enzymes, including HKII, PFK-1, PKM2 and LDHV, are overexpressed in many cancer types [254, 275, 276, 301]. However, there is little evidence for how HIF-1α affects the activity, expression and spatial distribution of the relevant glycolytic enzymes during TS growth. The data from TS culture are limited and compare TSs of differing maturity at two extreme time points of TS growth [35, 110]. The measurement of glycolytic enzyme expression solely at the start and end points of TS growth does not provide an insight into

how the process of glucose consumption changes throughout avascular tumour development. In order to capture a fuller picture, dynamic changes in glycolytic enzymes need to be investigated.

The aim of this chapter was to characterise changes in glucose metabolism during TS growth. Glucose metabolism was investigated by measuring glucose and lactate levels in DLD-1 TS medium, glucose consumption and lactate production per viable TS cell, activity and expression of HKII, PFK-1, PKM2 and LDHV. In order to determine the metabolic effects of changes in chosen key glycolytic enzymes, expression of their primary regulator in hypoxic conditions, that is, HIF-1α was measured.

6.3 Experimental methods

The experimental techniques and materials used to measure glucose and lactate concentrations in the TS culture medium and activities and expression of HKII, PFK-1, PKM2, LDH-V, HIF-1α expression, and the IF techniques used to detect HKII and PFK-1 distribution in TS cross-sections, were described in detail in Chapter 2.

In order to quantify the number of viable cells in TSs, the cross-sectional area of viable TS region was calculated using the results quantified in Chapter 3 and Chapter 4. Figure 6.4 shows a schematic view of the method of experimental estimation of the viable cross-sectional area and simplified geometry of a TS.

It was assumed that a single DLD-1 cell was a perfect sphere with radius of 6.5 μm. The sum of cross-sectional areas of normoxia and hypoxia was used to calculate the viable cross-sectional area, which was then divided by the cross-sectional area of a single cell to

obtain the number of viable cells per TS. The obtained number of viable cells per TS was used to quantify glucose consumption and lactate production per viable TS cell.

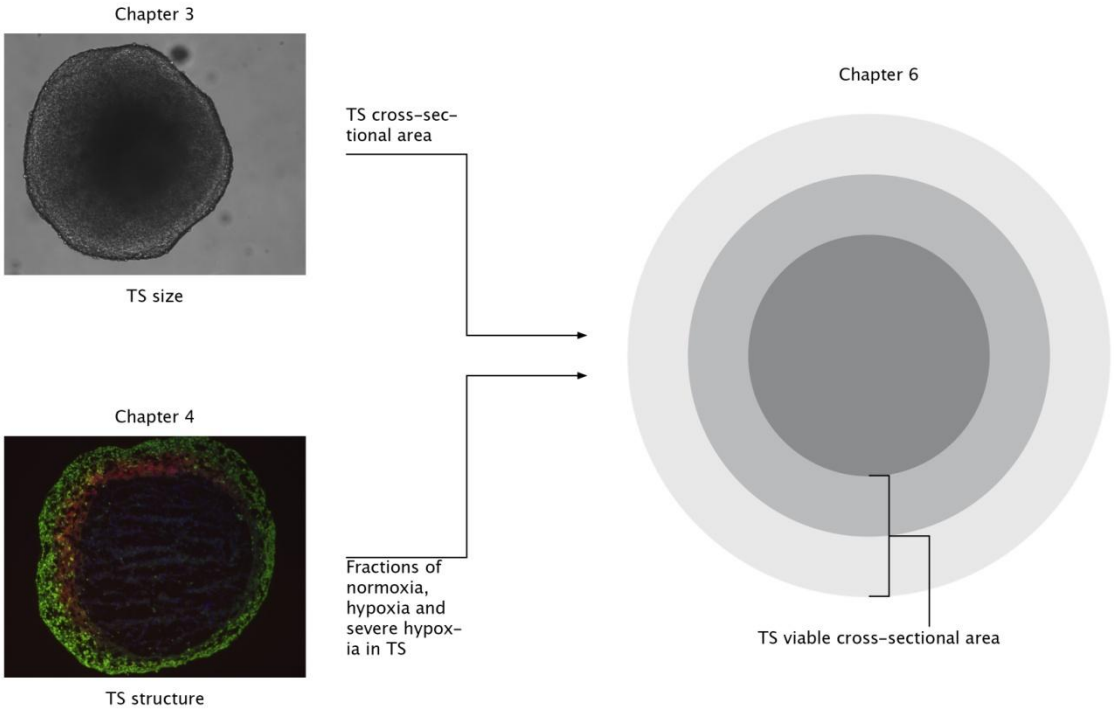


Figure 6.4: Schematic representation of the method of computing the viable cross-sectional area of a TS. The results of Chapter 3 for mean TS cross-sectional area and the results from Chapter 4 for mean fractions of normoxia and hypoxia were used to calculate the viable cross-sectional area. Under the simplifying assumption that a TS was a perfect sphere and regions formed in concentrically arranged shells, cross-sectional areas of normoxia and hypoxia were calculated and summed up to obtain the viable cross-sectional area.

6.4 Results

6.4.1 Changes in glucose and lactate levels in TS medium

Figure 6.5 shows the glucose levels of the culture medium obtained from TS culture. The glucose level in the pure medium was determined to be equal to 12.54 mM. After the initial four days of TS culture, which allowed for aggregate formation, the entire medium was replenished every 48 h. It was therefore assumed that after refreshing the used-up medium, the glucose concentration was raised back to the levels detected in the pure medium.

The 48h period between days 4 and 6 was associated with a decrease of 4.84 mmol/L in glucose concentration in the medium. The rate of change in glucose concentration in the medium gradually increased at a higher rate than that observed between days 4 and 6, with the highest decrease observed between days 16 and 18 of TS culture (7.93 mmol/L). Hence, an increasingly higher rate of glucose consumption by the TSs was clearly visible from day 16 until the end of TS culture time. A 1-way ANOVA and Bonferroni's multiple comparison post-hoc test showed that the mean glucose concentration was statistically different from the initial glucose concentration in the medium at days 18 and 20 of culture time (P value < 0.05), suggesting increased glucose consumption with increasing TS size over culture time.

If the Warburg effect described the energy generation pathways in DLD-1 TSs, then the increased glucose consumption should by reflected by an increase in lactate production. Figure 6.6 shows that lactate concentration in the culture medium noticeably increased over TS culture time. Since glucose was periodically replenished, changes in lactate concentration

in the medium gradually increased from 2.09 mmol/L between days 4 and 6, throughout the entire period of measurement and reached the highest change of 8.65 mmol/L between days 16-18. A 1-way ANOVA and Bonferroni's multiple comparison post-hoc test showed that the mean lactate values were statistically different from the initial lactate levels in the medium from day 16 until the end of TS culture time (significance for $P < 0.05$). Thus, the higher changes in lactate concentrations in the TS medium were correlated with the higher changes in glucose concentrations in the medium during the final days of TS culture time.

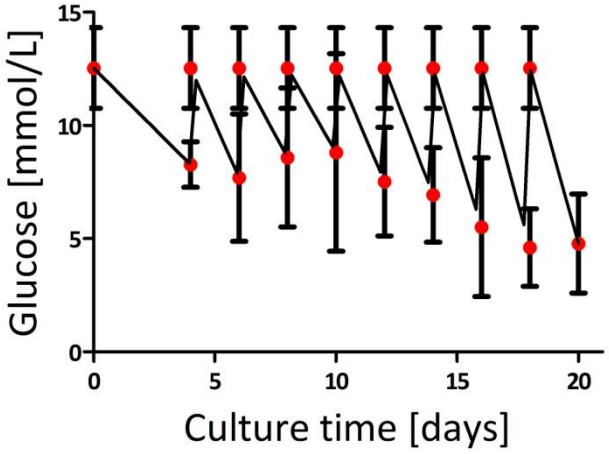


Figure 6.5: Changes in extracellular glucose concentration in TS growth medium. The lines connecting the data points represent medium replenishment, which was initiated at day 4 and performed every 48 h until the end of TS culture time. At each measured time point 1 ml of TS growth medium sample was measured using the Cambridge Bioscience glucose assay kit. The data represent the mean glucose concentration of TS growth medium from three independent experiments. Vertical lines denote standard deviation.

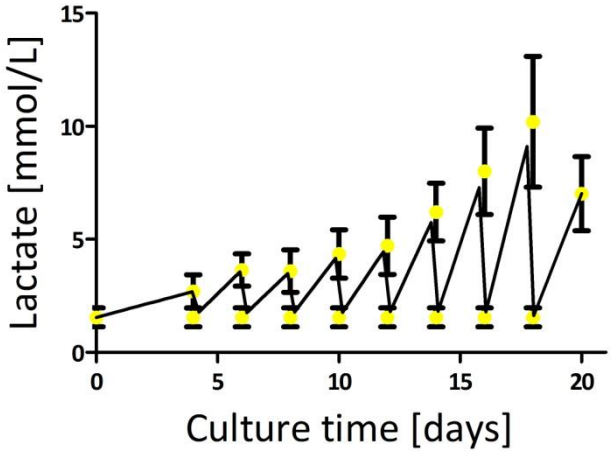


Figure 6.6: Changes in extracellular lactate concentration in TS growth medium. The lines connecting the data points represent medium replenishment, which was initiated at day 4 and performed every 48 h until the end of TS culture time. At each measured time point 1 ml of TS growth medium sample was measured using the Eton Bioscience L-lactate assay kit. The data represent the mean lactate concentration of TS growth medium from three independent experiments. Vertical lines denote standard deviation**.**

6.4.2 Changes in glucose and lactate consumption per viable TS cell

Hypothetically, the results presented in Section 6.4.1 showing a faster decline in glucose and increase in lactate levels in TS culture medium might have been a result of increase in viable cell fraction in TSs not increase in preference for glucose. In order to verify if this was indeed the case, the number viable cells per TS were quantified (using the method explained in Section 6.3) in the first place. Figure 6.7 shows that the number of viable cells per TS increased approximately 3.7-fold in the TS at the final days of growth (day 18) in comparison to the early time points (day 4).

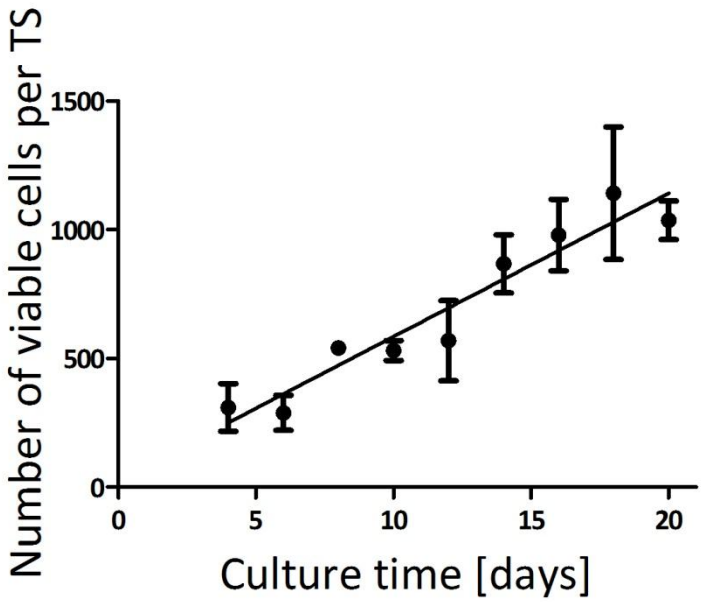


Figure 6.7: Number of viable cells per TS calculated with the method explained in Section 6.3 using the results from Chapter 4 and an assumption that a typical DLD-1 was a perfect sphere with radius of 6.5 μm. Data represent the number of viable cells per TS where error bars denote standard deviation.

Next, changes in glucose and lactate concentration in the medium (showed in Figure 6.5 and 6.6) were divided by the calculated number of viable TS cells showed in Figure 6.7. Figure 6.8 shows changes in glucose consumption rate per viable TS cell during TS growth. The rate of glucose consumption per viable TS cell was highest from the start of TS culture until day 4. Glucose consumption per viable cell decreased approximately 3.7-fold between days 6 and 8 and remained reduced throughout the remaining time points.

Figure 6.9 shows changes in lactate production per viable TS cell during TS culture time. If lactate production was only a result of glucose consumption, then lactate production also should have decreased. Indeed, the results show that lactate production per viable TS cell decreased approximately 2.2-fold between days 10 and 12 and remained reduced until the end of TS growth.

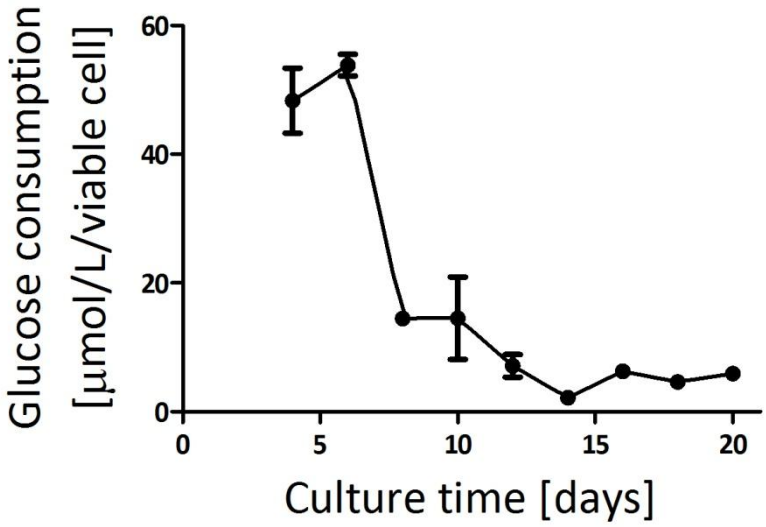


Figure 6.8: Changes in glucose consumption per viable TS cell. The data represent the mean glucose consumption per viable TS cell calculated using the experimental results from Chapters 3 and 4 and the method explained in Section 6.3. Data represent the mean glucose consumption per viable TS cell where error bars denote standard deviation.

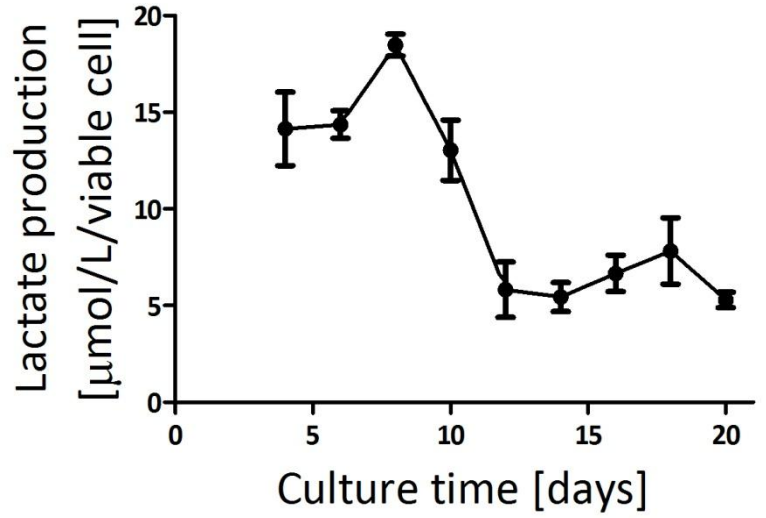


Figure 6.9: Changes in lactate production per viable TS cell. The data represent the mean lactate production per viable TS cell calculated using the experimental results from Chapters 3 and 4 and the method explained in Section 6.3. Data represent the mean lactate production per viable TS cell where error bars denote standard deviation.

6.4.3 Summary of changes in glucose and lactate metabolism

Changes in glucose levels in the medium implied an increased rate of glucose utilization in large TSs. However, when the severely hypoxic region consisting predominantly of necrotic cells, which were not metabolically active, was excluded glucose consumption and lactate production per viable cell number decreased. Thus, the observed change in glucose and lactate levels in the medium was likely to be attributed primarily to the increasing number of viable cells within a TS and not to an increase in glucose consumption.

6.4.4 Characterisation of key-glycolytic enzymes in DLD-1 TS homogenates

As there is a lack of standard protocols to follow, prior to assessment of kinetic properties of enzymes in TS homogenates, enzyme assays were established with commercially-available enzymes. Subsequently, kinetic properties were measured in these enzymes, which were then used to establish optimal reaction conditions. The maximal possible changes in enzyme activity and expression in homogenized TSs were identified for HKII and PFK-1 (Figure 6.10), PKM2 and LDHV (Figure 6.11) (all catalysing key-regulatory steps of glycolysis). Statistical significance for all measurements and results was determined using 1-way ANOVA and post-hoc Bonferroni's multiple comparison test and the results were compared to the initial measured data point.

All the measured enzymes demonstrated dynamic changes in their maximal activities from TS homogenates taken throughout the measured time points. Figure 6.10 shows the

changes in HKII activity in the TS homogenates. The maximal HKII activity remained constant in homogenates taken at days 2 and 4 (of 3.51 x 10^{-2} µmol/min/mg), followed by a rapid 4.2-fold increase to the highest activity measured in homogenates taken at day 10. Subsequently, the irregular pattern of changes in HKII activity was observed for the remaining culture times and the final value of 6.55 x 10^{-2} µmol/min/mg was reached in homogenates taken at the final day of TS culture. A 1-way ANOVA showed that the observed increase in maximal HKII activities in homogenates taken over culture time was not statistically significant (P values > 0.05). To more closely detect changes in HKII activity during TS growth, the HKII content in TS homogenates was evaluated by Western blot. The HKII content was which was in agreement with the observed lack of significant changes in HKII activity during TS growth. The detected molecular mass of approximately 100 kDa was consistent with the predicted molecular mass of human HKII [275].

Figure 6.10 shows changes in the maximal PFK-1 activity and content in DLD-1 TS homogenates. TS growth was associated with an approximate 7.5-fold increase in PFK-1 activity from initial activity measured at day 2 (of 2.51 x 10^{-2} µmol/min/mg) to 1.88 x 10^{-1} µmol/min/mg observed at day 15. During the final days of TS culture time PFK-1 activity markedly dropped to attain its final value of 8.62 x 10^{-2} µmol/min/mg at day 20 of culture time. The observed increase in maximal PFK-1 activity in homogenates taken over TS culture time was statistically significant at majority of TS culture time points (P values < 0.05) except day 2 and 20 where changes in PFK-1 maximal activity were not statistically significant (P values > 0.05).

In order to determine if changes in maximal PFK-1 activity measured in DLD-1 TS homogenates were a result of changes in PFK-1 content, PFK-1 expression was evaluated by

Western blot analysis. The expression levels of PFK-1 were approximately 2-fold higher for the early times of TS culture (between days 2-6) than for the remaining time points of TS growth. The capacity of PFK-1 rose dramatically between days 10-15 and then fell sharply to day 20. Rather surprisingly, this statistically significant increase in maximal PFK-1 activity was concomitant with a marked reduction in PFK-1 expression in the second half of TS culture. Indeed, the overall amount of enzyme dropped when maximal PFK-1 activity was the highest. This may reflect altered post-translational modification or regulation of the PFK-1 enzyme (described in detail in [302]). PFK-1 is one of the most highly regulated enzymes in the glycolytic pathway and responds to various hormonal influences and cellular redox status. Discordance between PFK-1 activity and expression might reflect the altered regulation of enzyme activity to optimize the scavenging of any available glucose. The apparent molecular mass of approximately 80 kDa was consistent with the predicted molecular mass of the human PFK-1 subunit [303, 304].

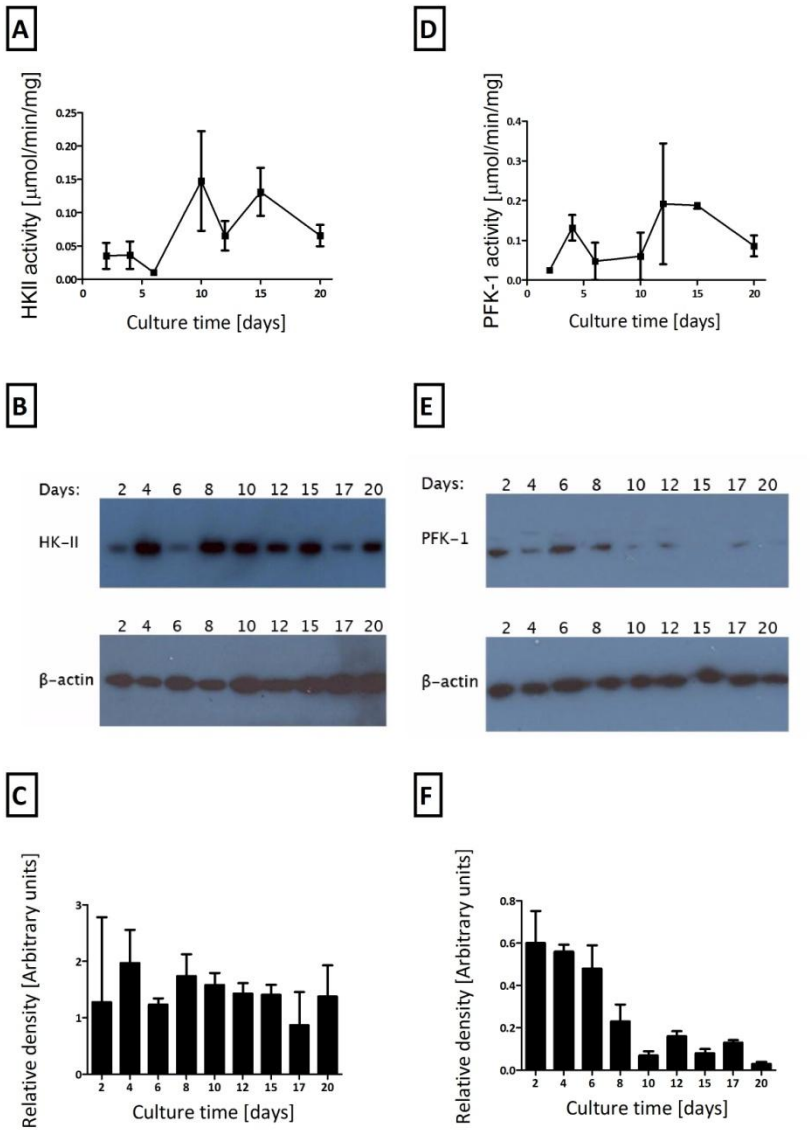


Figure 6.10: Changes in maximal HKII and PFK-1 activity and expression in TS homogenates. (A) Changes in maximal HKII activity in TS homogenates. (B) Representative Western blot of changes in HKII content in DLD-1 TSs and corresponding β-actin used as a loading control. (C) Densitometry analysis of TS homogenates representing the HKII levels normalised to β-actin. (D) Changes in maximal PFK-1 activity in TS homogenates. (E) Representative Western blot of changes in PFK-1 content in DLD-1 TSs and corresponding β-actin which was used as a loading control. (F) Densitometry analysis of TS homogenates representing the PFK-1 levels normalised to β-actin. The relative density represents a cumulative result obtained by densitometry analysis of three Western blots (data not shown). Hence, the representative Western blot does not fully correspond to the presented relative density. All data represent the mean of three experiments where error bars denote standard deviation.

Figure 6.11 shows changes in maximal PKM2 activity in DLD-1 TS homogenates. Maximal PKM2 activity showed a noticeable and approximately 2.1-fold increase in homogenates taken at day 4 (6.92 µmol/min/mg) to maximal enzyme activity detected in homogenates obtained at day 12 (14.3 µmol/min/mg). This was followed by a decline in activity to 9.56 µmol/min/mg at day 20. The observed changes in maximal PKM2 activities from homogenates taken throughout the TS culture time were not statistically significant (P values > 0.05). Lack of significant changes in maximal PKM2 activity in homogenates at different time points of TS culture was correlated with no significant changes observed in PKM2 expression pattern in the TS homogenates studied. According to densitometry analysis, the expression levels of PKM2 remained similar to PKM2 content determined in TS homogenates at day 2. The apparent molecular mass of approximately 60 kDa was consistent with the predicted molecular mass for human PK [305].

LDHV activity determines the outflow of the anaerobic glycolysis pathway and results in the production of lactate, which is the final product of this pathway. Changes in maximal LDHV activity and expression in TS homogenates are presented in Figure 6.11. The results show a gradual increase in maximal LDHV activity in homogenates obtained at day 2 (2.91 µmol/min/mg), with some fluctuations throughout the majority of investigated culture time points increasing by 2.4-fold in homogenates taken at day 20 (6.81 µmol/min/mg). The observed increase in maximal LDHV activities in homogenates taken over TS culture time was statistically significant (P values < 0.05). The maximal LDHV activity in homogenates taken at day 20 of TS culture time was statistically different to the maximal LDHV activity in homogenates taken at day 2 of TS culture time.

In order to determine the correlation between maximal LDHV activity and LDHV expression in DLD-1 homogenates taken at different time points, the LDHV content in DLD-1 TSs was evaluated by Western blot analysis. The results show that the increase in LDHV activity was driven by enhanced LDHV expression. The detected molecular mass of LDHV of approximately 36 kDa was consistent with the predicted molecular mass of mammalian LDHV [306].

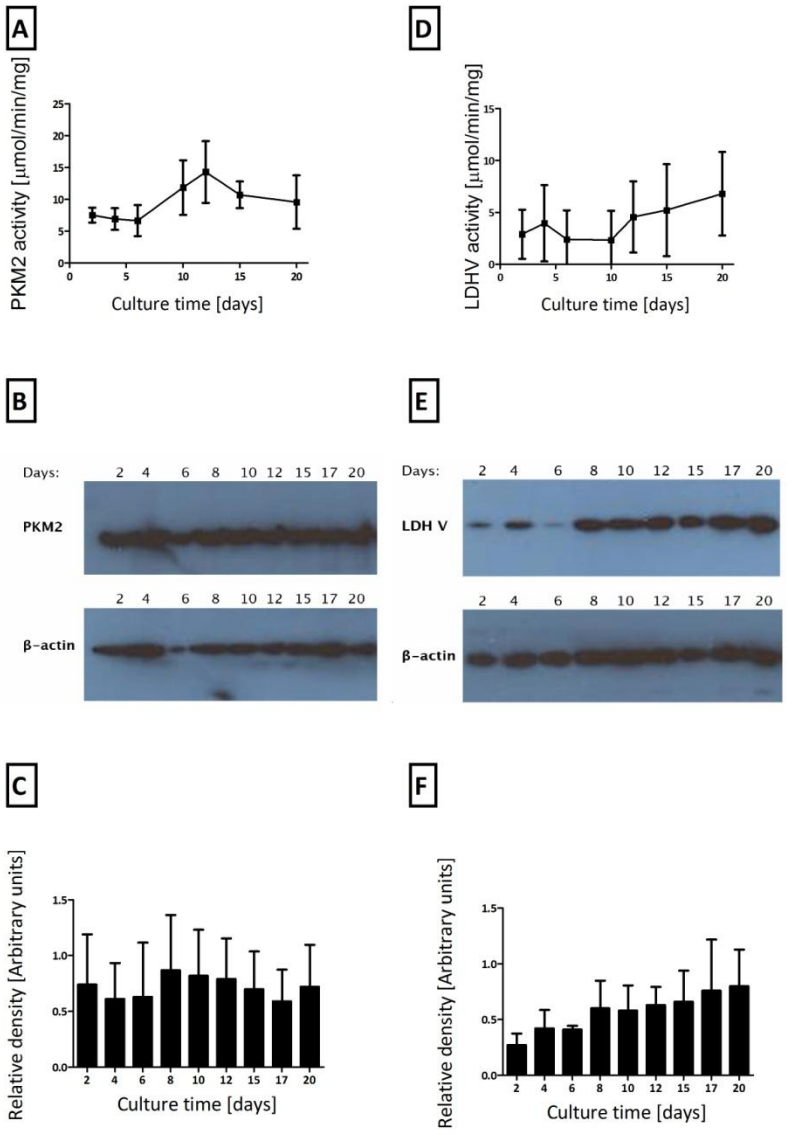


Figure 6.11: Changes in maximal PKM2 and LDHV activity and expression in TS homogenates. (A) Changes in maximal PKM2 activity in TS homogenates. (B) Representative Western blot of changes in PKM2 content in DLD-1 TSs and corresponding β-actin used as a loading control. (C) Densitometry analysis of TS homogenates representing the PKM2 levels normalised to β-actin. (D) Changes in maximal LDHV activity in TS homogenates. (E) Representative Western blot of changes in LDHV content in DLD-1 TSs and corresponding β-actin which was used as a loading control. (F) Densitometry analysis of TS homogenates representing the LDHV levels normalised to β-actin. The relative density represents a cumulative result obtained by densitometry analysis of three Western blots (data not shown). Hence, the representative Western blot does not fully correspond to the presented relative density. All data represent the mean of three experiments where error bars denote standard deviation.

6.4.5 Evaluation of HIF-1α content in DLD-1 TS homogenates

In order to identify changes in HIF-1α content in DLD-1 TSs, analysis of Western blot using densitometry was performed. The results are shown in Figure 6.12. The observed molecular mass of HIF-1α of 120 kDa was in agreement with the predicted molecular mass of human HIF-1α [307]. The results show that HIF-1α content was maintained relatively constant throughout the majority of TS culture. The highest expression was detected at day 4 and was approximately 2-fold higher than HIF-1α expression at the remaining time points.

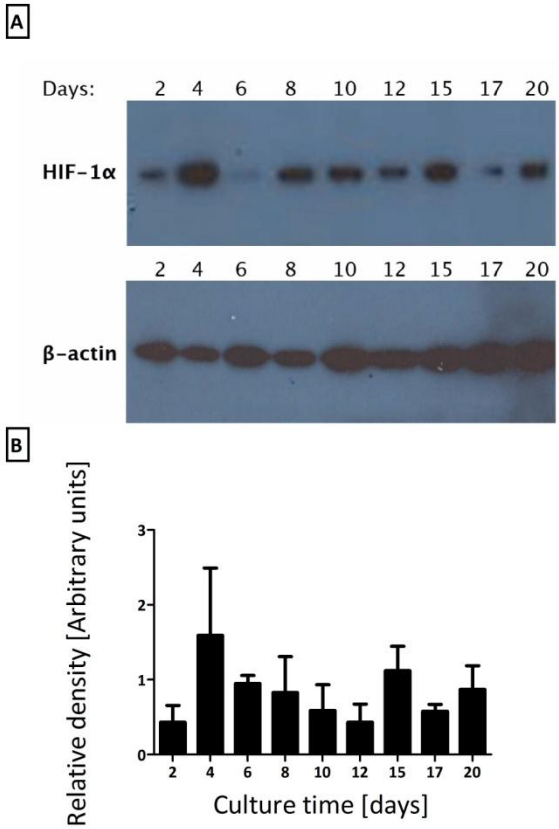


Figure 6.12: Changes in HIF-1α content in TS homogenates. (A) Representative Western blot of changes in HIF-1α content in DLD-1 TSs and corresponding β-actin used as a loading control. (B) The relative densitometry analysis of three Western blots (data not shown) representing the content of HIF-1α normalised to β-actin. The data represent the mean of three experiments where error bars denote standard deviation.

6.4.6 Changes in the spatio-temporal distribution of HKII and LDHV

In order to determine the spatial distribution of the measured glycolytic enzymes, IF techniques were used. The preliminary experiments were performed to determine the distribution of HKII, which catalyses the input of the glycolytic pathway and traps glucose in a cell, and LDHV, which catalyses the final step of anaerobic glycolysis that results in lactate production.

Figure 6.13 (top row) shows representative images of HKII distribution in DLD-1 TS cross-sections. Qualitative evaluation revealed that HKII expression was not restricted to a certain TS region but prevalent throughout the viable area of TS cross-sections. The exception was day 2, when HKII was localised close to the TS boundary. At a single-cell level, as expected, HK II expression was present in the cell cytoplasm. The cytoplasmic enzyme was visible in the analysed images, as it surrounds the cell nuclei, which were visualised with Hoescht 33342.

Figure 6.13 (bottom row) presents changes in the spatial distribution of LDHV in DLD-1 TS cross-sections. At day 2 the distribution of LDHV overlapped with the distribution of HKII and implied that LDHV was localised close to the TS boundary and absent from the inner TS region. Similarly, the LDHV distribution showed a cytoplasmic localisation. In contrast to the HKII distribution, at day 6 of culture LDHV expression was the most intense in the hypoxic region of a TS.

The visual inspection of cross-sectional DLD-1 TS images stained with both HKII and LDHV showed a large amount of non-specific binding of the detecting antibody in the

severely hypoxic region, presumably due to surface tension effects from the fluids used in the IF procedure.

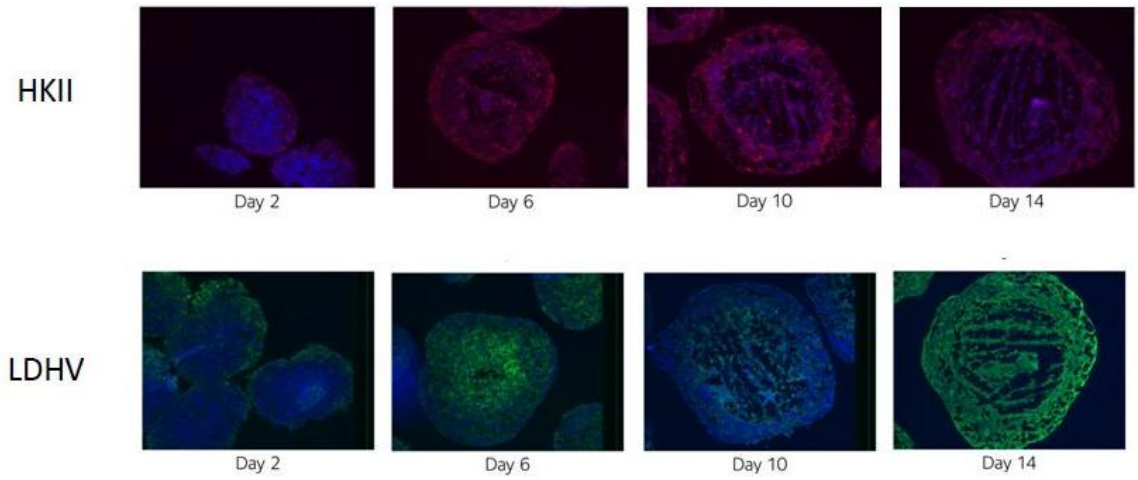


Figure 6.13: Representative images of TS cross-sections stained for HKII (HKII-A594, red and cell nuclei (Hoechst 33342, blue) and LDHV (LDHV-FITC, green) and cell nuclei (Hoechst 33342, blue) over the selected time points of TS culture.

6.5 Discussion

In this chapter the relationship between changes in glucose consumption, in terms of the maximal activity and expression of key glycolytic enzymes, and HIF-1 content were investigated over the course of DLD-1 TS growth. The results presented here were somewhat contradictory. Changes in glucose and lactate levels in the culture medium suggested an increase in glucose consumption over the course of TS growth, whereas changes in glucose metabolism per viable TS cell implied a reduction in glucose consumption. However, the data presented a well-defined increase in maximal LDHV activity

which was elevated in regions of hypoxia, suggested constant adaptation of tumour cells to their microenvironment. Although development of the glycolytic phenotype during TS growth was observed in the form of an elevated maximal activity of the PFK-1 and LDHV enzymes, the activity and expression of other glycolytic enzymes, including HKII and PKM2, was unaltered. Finally, the results showed that the HIF-1α content in DLD-1 TS homogenates, taken at different time points during TS growth, remained relatively constant.

The results presented in Figure 6.5 showed that changes in glucose levels in the medium were 1.6-times lower in the first few days of TS culture than changes in glucose levels in the medium at the later stages. This implied that glucose consumption increased over time, and this was supported by observed changes in the maximal PFK-1 and LDHV activities. PFK-1 and LDHV maximal activities in homogenates taken from the early time points of TS culture were 7.5-fold and 2.4-fold lower respectively, than maximal glycolytic PFK-1 and LDHV activities in homogenates obtained from TSs in the later days of culture time. However, when glucose consumption was quantified per viable TS cell the results showed (Figure 6.8) that glucose consumption decreased by 3.7-fold in TSs of a radius of 268 μm (day 6) and 370 μm (day 8) respectively, and remained reduced throughout the remaining culture time. This was in agreement with a study by Freyer and co-workers [58], who showed that glucose consumption per viable TS cell was reduced by 2.5-fold in TSs of diameter 1300 μm compared with those of up to 150 μm in diameter. Presumably, the reason for the observed reduction in glucose consumption was accumulation of non-proliferating cells in the TSs during growth as it was previously shown that inhibition of cell proliferation correlates with a reduction in glucose consumption [260, 308]. As shown in Figure 4.17 in Chapter 4, viable cells consisted of both proliferating and non-proliferating

cells. As small TSs (at day 2) were primarily composed of proliferating cells, glucose consumption was representative of metabolism of proliferating cells. The detected accumulation of non-proliferating cells led to a decrease in glucose consumption in large TSs. The non-proliferating cells in hypoxic regions had also limited access to glucose, hence were less metabolically active than their proliferating counterpart and there was no increase in the content of HIF-1 α as its effects were dependent on glucose availability.

Overall, the observed increase in LDHV maximal activity throughout TS growth suggest that this enzyme may provide a survival advantage in especially in hypoxic tumour cells (as shown by the preliminary results shown in Section 6.4.6).

Rodríguez-Enríquez et al. [35] suggested that increased glucose consumption in large vs. small TSs was mediated by increased content of HIF-1α. The results in this chapter showed that even though maximal PFK-1 and LDHV activity increased over time, the HIF-1α content in DLD-1 TS homogenates remained relatively constant (Figure 6.12). The lack of increase in expression of HIF-1α could have been caused by nutrient limitations, which result in the development of a non-viable cell fraction that does not express HIF-1α. HIF-1α content is regulated not only by hypoxia but also by other factors such as mutations in the K-Ras oncogene and various oncogenic pathways, such as MAPK and PI3K/Akt pathways. Even though DLD-1 colon adenocarcinoma expresses an activated copy of K-Ras oncogene [60] which is known to induce HIF-1α expression in this cell line [61], presumably the contribution for other signalling pathways inhibited an increase in HIF-1α content.

Despite the fact that studies in monolayers suggested that stabilized HIF-1α provides a growth advantage and mediates metabolic reprogramming by favouring glucose consumption in hypoxic conditions [292], there is no consensus if this is the case in a TS

model. The study by Kim and Forbes [110] showed that HIF-1α did not provide a growth advantage in wild-type TSs compared to HIF-1α-null TSs. Despite the fact that the diffusion coefficient for glucose in tissue is lower than that for oxygen [309], glucose is likely to be consumed by the cells located at the TS periphery. Thus, the hypoxic regions are typically low in glucose concentrations [116, 310]. Hence, metabolic reprogramming mediated by HIF to favouring glycolysis in hypoxic regions might not provide growth or survival advantage as glucose could be depleted there.

It should be mentioned that the analysis of maximal enzyme activities in the TS homogenates used in this study was based on analysis of changes in kinetic properties of selected enzymes (that is, *v* and *K* values). These kinetic properties were measured in pilot assays with commercially-available enzymes in order to obtain optimal reaction conditions and ascertain that the substrate concentration used in assays is at saturation and not limiting. Consequently, the analysis of enzyme activities allowed for comparison of kinetic properties of TSs throughout different time points but is not sufficient to reach conclusions on metabolic control *in vivo*. Whether or not the observed changes in the maximal enzyme activities in TS homogenates correspond to bioenergetic changes in the maximal enzyme activities in avascular tumours *in vivo* depends on the substrate availability and regulation by enzyme physiological activators and inhibitors. As the data from *in vivo* avascular solid tumours are incomplete, TSs provide the most viable system to investigate metabolic changes in tumours during growth *in vitro*.

The analysis of enzymes involved in consumption of other nutrients is needed to fully understand changes in TS metabolism. In particular, investigation of the key enzymes involved in glutaminolysis is a natural next step emerging from this work, which shows a

decrease in glucose consumption. Glutamine, the most abundant amino acid in plasma, is an important metabolic fuel, which in the presence of oxygen is a precursor of nucleic acids and serine synthesis which are required for cell proliferation [311]. In tumour cells that exhibit the high proliferative phenotype, glucose consumption must be balanced with energy production from glutaminolysis which feeds into glycolysis at the level of pyruvate [254]. The primary question that remains to be answered is how the major bioenergetic pathways are synchronised to adjust and direct the metabolic flux to the most favourable pathway that enables the proliferating phenotype and survival of cancer cells.

Increased LDHV activity in the absence of increased glucose consumption and lactate production per viable cell suggested that lactate might have been utilised as an energy source for aerobic metabolism in the normoxic fraction of cells, as recently proposed by Sonveaux et al. [256]. However, it should be noted that in this chapter the number of viable cells per TS was quantified using the results obtained in Chapters 3 and 4, and typical cell volume calculated under the assumption that a cell is perfectly spherical. In future work it would be interesting to experimentally verify changes in the number of viable cells over the course of TS growth through dissociation and conventional cell counting methods.

Presumably the increased levels of lactate in the medium detected in the final days of DLD-1 TS culture time could explain fast TS disintegration (discussed in Chapter 3). The levels of acid in the medium could have provoked an auto-toxic response. The increased acidity of the tumour environment can be attributed not only to the activity of LDHV but also to the activity of carbonic anhydrase 9 (CA9) which, by regulating the hydration of carbon dioxide to carbonic acid, contributes to the extracellular acidification [312]. As acidity plays a crucial role in tumour growth and invasion, in future work changes in CA9 and pH

should be analysed to investigate the topic in more detail and determine if there is a relationship between the observed TS disintegration and acidity of tumour microenvironment. In 2005 Smallbone et al. [139] proposed a mathematical model of a dual role of the acid that can act both as promoter or inhibitor of tumour growth. If the acid concentration was not removed from the tumour and reached a certain threshold a tumour cell became necrotic. On the other hand, the authors suggested that a high acid concentration could be toxic for the nearby healthy cells, which in this case would allow for further tumour expansion and offer a growth advantage. The authors found that an avascular solid tumour always followed a benign growth pattern whereas vascular tumours displayed a benign or invasive growth pattern depending on the cellular sensitivity to acid-induced cell death.

The changes in maximal glycolytic enzyme activities and expression in TS homogenates found in this chapter were not specific to a particular cell type, proliferating or quiescent, but were unified per mg of total protein content (which is the standard method of analysis of enzyme kinetics) in order to compare between different time points. In the final results section (Section 6.4.6) the preliminary work showing spatial distribution of HKII and LDHV in DLD-1 TSs was presented. The results showed a cytoplasmic localisation of the measured enzymes but, in terms of spatial distribution in a TS, HKII was distributed throughout the viable TS region, whereas LDHV expression was increased in the intermediate hypoxic region of a TS. However, in order to validate the preliminarily qualitative observations, quantitative analysis has to be performed. The natural next step is to use the method of image analysis developed in Chapter 4. Before, this can be done, our IHC protocol has to be optimised to co-stain for HKII and LDHV and a chosen hypoxic marker.

The results presented here provided the initial experimental set of data describing changes in glucose metabolism and HIF-1α content in TSs cultured in optimal, nutrient-rich conditions at different time points of TS growth. As the general goal of this work is to investigate the impact of substrate supply on proliferation and induction of cellular quiescence, in future work TSs should be cultured in various closely monitored conditions, such as with depleted glucose or glutamine and reduced oxygen. The future experiments will have to be performed in multiple TS-forming cell lines. Results from such experiments will be crucial to build and validate a basic model of TS metabolism. This understanding is important to develop drugs that could successfully target the weak points in cancer metabolism which could be used for therapeutic purposes [207].

Chapter 7 Summary and further work

In this chapter we summarise the work presented in this thesis and discuss possible avenues for further work.

7.1 Summary

Tumour growth is a complex biological process. In this thesis we have gained insight into the biological processes underlying avascular solid tumour growth by using an *in vitro* system, the multicellular TS, which reproduces many of the characteristics of avascular tumours. TS characteristics are likely to vary considerably with the origin and type of cell line used [293]. Focusing on the DLD-1 human colon adenocarcinoma cell line as an exemplar, we used a combination of experimental and theoretical approaches to characterise changes in TS size and morphology, internal composition, and metabolism throughout the time course of TS growth.

When attempting to describe tumour development, careful thought is required in deciding how to integrate knowledge about phenomena at different scales to formulate a clinically relevant and predictive model. In order to describe the morphological and biochemical development of an avascular solid tumour correctly, spatial and temporal biological mechanisms must be taken into account. In this thesis, we have used an interdisciplinary approach to gain insight into how changes in TS composition and

metabolism regulate cell proliferative status and vice versa. In brief, the key findings of this thesis are:

1. DLD-1 TSs showed a gradual and consistent increase in their cross-sectional area during growth, but the TS surface was very irregular and ragged. Additionally, DLD-1 TSs exhibited a slightly elongated geometry, within 10% deviation from being perfectly spherical.
2. The negative effect of hypoxia on proliferation was observed within the same 48 h period. Despite the fact that the fraction of proliferating cells was reduced in hypoxia, a distinct fraction of proliferating cells was present in hypoxia throughout the entire period of TS growth.
3. Mathematical simulations predicted a decrease in oxygen consumption over the time course of TS growth. Our findings suggest the need to consider the stage of cellular growth when defining the rate of oxygen consumption in theoretical studies.
4. Glucose consumption in DLD-1 TSs decreased whereas LDHV maximal activity increased during TS growth. Increase in maximal LDHV activity, which was elevated in the regions of hypoxia, shows a constant adaptation of tumour cells to their microenvironment.

We began our characterisation of DLD-1 TSs by analysing changes in their size and external structure during growth. Faced with the lack of a reproducible method that could be used to accurately quantify TS size, in Chapter 3 we developed a novel method of analyzing microscopy images, which can be easily used in most laboratory settings for fast and accurate measurement of large numbers of TS images. We found that each TS's perimeter was highly irregular and ragged, and that TSs were of a slightly elongated geometry, within 10% deviation from being perfectly spherical. We determined cross-sectional area to be the most robust method of assessing a TS's size. We observed fast

disintegration of DLD-1 TSs after they reach a maximal size at day 20 of culture time. Fast TS disintegration of DLD-1 TSs has been reported previously, and has been attributed to large central regions of necrosis, but no direct experimental evidence was provided to support this claim [35, 107]. Our quantitative analysis performed in Chapter 4 revealed that, by day 18-20 of culture, DLD-1 TS were mostly severely hypoxic and composed of necrotic cells. This may be one of the primary causes of the fast disintegration discussed in Chapter 3.

We completed our characterisation of DLD-1 TS growth by fitting exponential, logistic and Gompertz models to the volume data obtained from the calculated TS cross-sectional area corrected by the measured deviation from perfect sphericity. We found that the detected growth pattern of DLD-1 TSs can be best described with the logistic model.

Tissue oxygenation is determined by the subtle balance between supply and demand of oxygen. When the demand for oxygen exceeds supply, a tissue falls into hypoxia. During the growth of a TS, cells located in the inner region of the TS naturally become hypoxic. The scientific consensus is that proliferation decreases from the TS periphery towards its inner core, and this coincides with a decrease in oxygen consumption and the formation of a hypoxic core. We showed in Chapter 4 that the spatial heterogeneity in oxygen availability results in a gradual but continuous decrease in oxygenation and leads to development of normoxia, hypoxia and severe hypoxia.

We developed an image analysis method that enables the quantification of fractions of proliferating and non-proliferating cell types in various regions of oxygen concentration. This method is based on hypoxic staining with the EF5 marker, under the primary assumption that TSs are symmetric spherical structures with concentrically arranged regions of severe hypoxia, hypoxia and normoxia. Our method allowed for reproducible

quantification of proliferation, as detected with the marker Ki-67, in the specified regions. We showed that despite the fact that the fraction of proliferating cells was instantaneously reduced in hypoxia, a distinct number of cells remained proliferating in the hypoxic region (approximately 10-16% fraction of hypoxic cells) until the end of TS culture time.

In Figure 7.1 we show a schematic representation of the general changes in TS growth and internal structure that were characterised in Chapters 3 and 4. The accumulation of non-proliferating cells in the hypoxic region of a TS, and the development of a central necrotic core (corresponding to the severely hypoxic region in our schematic representation in Figure 7.1), have both been associated with the formation of nutrient gradients within the TS. The spatial distributions of these regions, and their evolution, have been successfully predicted in various conditions using mathematical models [53-56, 212, 313]. Thus, mathematical modelling has helped to elucidate how a TS interacts with the surrounding environment via diffusion of nutrients and removal of waste products.

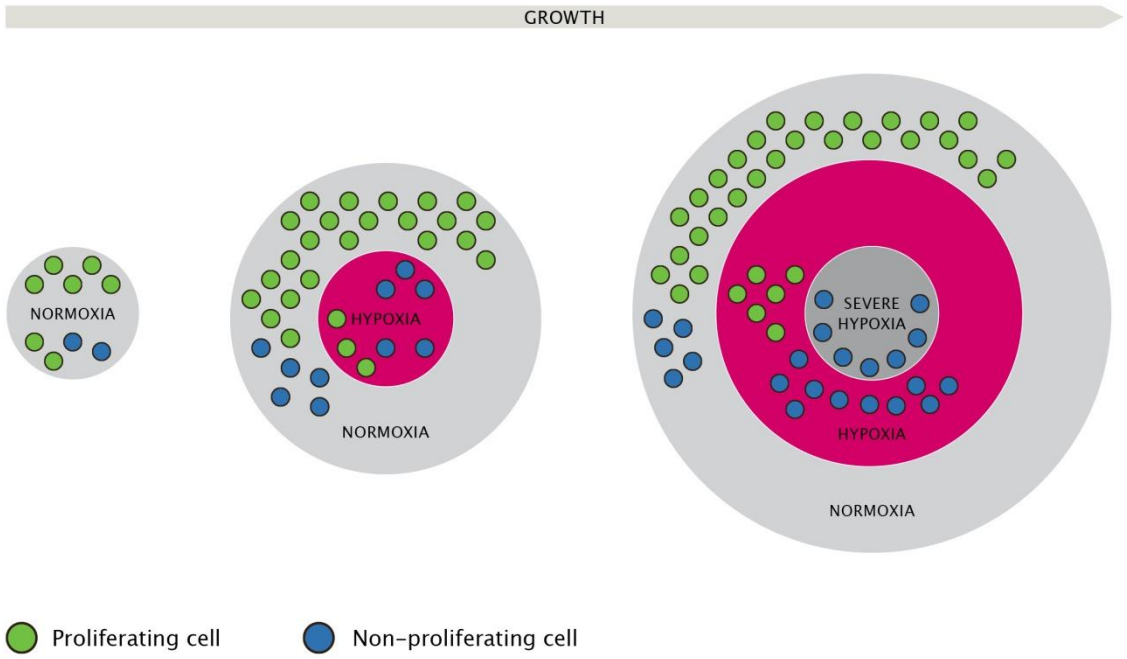


Figure 7.1: Schematic representation of changes in TS size and internal composition during TS growth.

Having quantified the experimental data in a consistent and reproducible manner in Chapter 3 and Chapter 4, we used our data further in Chapter 5. We formulated a mathematical model of oxygen transport in a TS that incorporated Fickian diffusion. The model was used to investigate the process of proliferation under two hypotheses concerning oxygen consumption. In the first hypothesis, termed Model 1, we assumed that proliferation occurs throughout the TS and that the oxygen consumption rate varies only with oxygen concentration. In the second hypothesis, termed Model 2, we considered a more realistic scenario in which the rate of oxygen consumption is allowed to vary between proliferating and non-proliferating cell types. This more detailed model allowed us to incorporate the fractions of proliferating and non-proliferating cell types quantified in Chapter 4.

Model 1 predicted that the onset of hypoxic binding occurs at pO_2 levels similar to those reported in the literature, however the onset of necrosis was overestimated. The oxygen gradient predicted by Model 2 was shallower, favouring the survival of cells distal to the TS surface. Although the oxygen thresholds predicted by Model 2 overestimated the pO_2 levels at which we expected to detect hypoxia and severe hypoxia, both models predicted a decrease in maximal rate of oxygen consumption during TS culture. Hence, a decrease in oxygen consumption throughout TS growth predicted by Model 1 and 2 supports the need to consider the stage of cellular growth when defining the rate of oxygen consumption. Moreover, the predictions of Model 2 show that non-proliferating cells consume oxygen at approximately 83% of the rate that proliferating cells do and the magnitude of the reduction in oxygen consumption is maintained at various TS sizes. In summary, in Chapter 5 we showed that tissue proliferative heterogeneity impacts oxygen distribution within TSs. However, either proliferative heterogeneity does not need to be considered in predicting oxygen gradients within TSs, or that more sophisticated models are required.

Finally, in Chapter 6, we turned our metabolic focus from hypoxia and oxygen consumption to glycolysis. This is the primary mechanism enabling enhanced proliferation and survival of cancer cells in hypoxic conditions. We first analysed changes in the TS microenvironment over the time course of culture by measured changes in glucose and lactate levels in the culture medium. We observed a faster decline in glucose levels and an increase in lactate levels in the culture medium in the latter stages of culture, indicative of an increased glycolysis. However, when we quantified the number of viable cells in a TS using the results from Chapters 3 and 4 we found that, in reality, glucose consumption and lactate production decreased with increasing number of viable cells in a TS.

In contrast to these findings we observed increased maximal activity of LDHV, which was elevated in hypoxic regions, and increased maximal activity of PFK-1 in TS homogenates taken at majority of time points. Hence, we conclude that we observed development of glycolytic phenotype, but not across all of the examined enzymes as maximal activities of HKII and PKM2 were unaltered throughout TS growth. These findings suggest a constant adaptation of tumour cells to their microenvironment and a plausible use of energy sources other than oxygen or glucose to maintain proliferation throughout the period of TS growth.

7.2 Further work

In each chapter we have discussed possible directions of further work; here therefore, we will discuss more general areas for development.

Although in this thesis we have only analysed a single TS-forming cell line, the platforms we have developed to quantify TS size, geometry and internal composition can easily be applied to other cell lines. In the context of mathematical modelling, we aim towards building a mathematical model of TS growth and metabolism that is grounded in the large and statistically significant data set that would be generated from such further studies. In order to do so, the natural next step is to generate the experimental data needed to parameterise the model. The key limitation faced is that generation of the necessary experimental data is costly and time-consuming. In the following text we discuss the possible routes of further experimental investigation which emerged from the work in this thesis.

In the context of characterising TS size and morphology during growth, it would be interesting to determine if the irregularities we detected in TS boundaries are a consequence of increased metastatic potential of cancer cells located at the periphery of a DLD-1 TS. This could be determined by using IHC methods to identify expression of the markers associated with a more aggressive biological phenotype, including angiogenic cytokines such as VEGF. We could quantify their fractions in each region of TS oxygenation using the image analysis tool presented in Chapter 4. As our image analysis allows us to characterise changes in TS morphology with high sensitivity, it would be interesting to determine how the TS external structure changes when TSs are cultured in different environments, for example using a tissue culture medium supplemented with additional glucose or depleted from glutamine [314].

A natural next step in the work emerging from Chapter 4 is to gather more experimental data, not only from the DLD-1 TS cell line, but from other TS-forming cell lines. Large data sets could be easily analysed using the image analysis method we developed in Chapter 4, which would allow a more detailed investigation of the relationship between proliferation and hypoxia over the time course of TS growth. Additionally, we note that in Chapter 4 we used only one marker to detect proliferation and one marker to detect hypoxia. Even though the combination of these markers has been previously shown to successfully detect both proliferation and hypoxia [163, 315-317], further work should verify to what extent the distributions of other markers, such as HIF-1α to detect hypoxia and cyclin E to mark proliferation, match our experimental data. In Chapter 4 we specifically detected a proliferating cell type; in order to complete the characterisation of each TS region, the fractions of apoptotic and quiescent cell types should be quantified using specific

cellular markers, such as the apoptotic marker caspase-3 and the quiescent marker p27 (an inhibitor of cyclin-dependent kinase).

Tumour metabolism is a complex process. In order to describe it we must integrate information from both experimental work, in particular in the context of multiple metabolic and cellular signalling pathways, and theoretical studies, to help limit our investigations to those processes that are crucial. We used a theoretical approach in Chapter 5 to describe changes in oxygen consumption in the context of changes in proliferation in regions of normoxia, hypoxia and severe hypoxia. We note that we used our relatively small sample size from which we derived the fractions of proliferating and non-proliferating cell types in Chapter 4. A natural next step is to gather a larger, statistically significant number of images that can be quantified for proliferation and hypoxia in TSs to obtain more realistic estimates of the model parameters.

The reduction in oxygen consumption at increasing TS sizes, which we predicted with mathematical simulations in Chapter 5, can prioritise energy utilizing processes in terms of importance for survival. Changes in gene expression, regulated mainly by HIF-1, aim to optimize energy supply, improve tissue oxygenation and find alternative methods to generate energy. The most prevalent bioenergetic change observed in cancer cell lines is an increased rate in glucose consumption, which we analysed in Chapter 6. In that chapter we investigated changes in HIF-1α and the expression of key glycolytic proteins throughout TS growth. Although protein synthesis is usually reduced in hypoxic conditions [318], we hypothesise that the glycolytic proteins must be expressed in order to optimize anaerobic energy production. Our results showed increased activity of LDHV and PFK-1 in the final days of TS culture time. It would be interesting to verify if the observed changes in glucose

consumption and lactate production per viable TS cell, which we quantified using the results from Chapters 3 and 4, are in agreement with experimentally obtained numbers of viable and non-viable cells within a TS. This can be done by dissociating the TSs using 0.5% Trypsin-EDTA solution and quantifying the number of viable cells.

The natural next step emerging from the work presented in Chapter 4 is to determine the spatial distributions of the key-regulatory glycolytic enzymes analyzed in Chapter 6. In the final results section of Chapter 6 we showed preliminary data on the distribution of HKII and LDHV in TS cross-sections. These preliminary results lack EF5 staining, hence, we cannot analyse them yet using the image analysis we developed in Chapter 4. The IF techniques needs to be optimised in order to obtain high quality images (similar to the ones we presented in Chapter 4) which consist of co-staining of EF5 with each of the key glycolytic enzymes discussed in Chapter 6.

From a more general point of view, a natural next step is to analyse the Warburg effect in terms of changes in other metabolic pathways, to ultimately determine if an increased glycolytic phenotype develops. The results presented in Chapter 6 show an increased LDHV activity, which is concomitant with a decrease in glucose consumption in the final days of TS culture time. As the LDHV catalyses the conversion of pyruvate to lactate, which is a product of both glycolysis and glutaminolysis, the next step is to analyse activities and expression of crucial enzymes of glutaminolysis. Recently, Sonveaux et al. [256] proposed that lactate might also be utilised as an energy source for aerobic metabolism in some cancer cells. Our findings showed that both oxygen and glucose consumption decreased over the time course of TS growth. We would like to measure spatial distribution of monocarboxylate transporter 1 (MCT1), which allows lactate uptake and promotes its

preferential utilisation in some cancer cells, to determine if DLD-1 TS cells use it as an energy source.

The tumour microenvironment is determined by nutrient consumption, waste production and transport. We began to characterise changes in TS environment by assessing changes in glucose and lactate concentration in TS culture medium in Chapter 6. The heterogeneous structure of avascular solid tumours, described in the context of proliferating and non-proliferating cells and regions of different oxygenation, limits the response of tumour cells to chemotherapy and radiotherapy. Hence, the impact of varying external nutrient supply should be taken into account in order to more accurately predict the nutrient distribution in solid tumours. Thus, further work should closely monitor how changes in nutrient concentration in the medium, including specifically defined levels of glucose, oxygen, glutamine and lactate, impact TS size, gross morphology, internal composition and metabolism.

In general, the proliferating cell fraction in a solid tumour drives growth, which leads to the development of hypoxic regions. In order to make our study clinically relevant in future work, changes in proliferation should be evaluated, in the context of oxygen distribution within TS as a response to radiation and chemotherapy. This could provide insights about the underlying metabolic mechanisms and cell dynamics that lead to the development of resistance to chemotherapy in solid tumours.

We highlight the fact that our work is a pilot study, which has provided a detailed characterisation of a single TS-forming cell line in optimal growth conditions. A larger, statistically significant sample size, must now be gathered in order to improve our baseline mathematical model to account for the changes in distribution of different cell types in a

growing TS. This would allow investigation of more biologically and clinically interesting changes in growth, morphology, internal composition and metabolism as a response to various treatment modalities which then can be used in treatment of solid tumours. This could eventually lead to generation and evaluation of possible new tumour therapies. For example, one would be able to assess what is the impact of the inhibitors of the selected glycolytic enzymes on more general changes in TS size, morphology, internal composition and metabolism.

Acronyms

2D two-dimensional

3D three-dimensional

A cross-sectional area

a major axis length of a spheroid

ACL adenosine-5'-triphosphate-citrate lyase

ADP adenosine diphosphate

ANOVA analysis of variance

ATP adenosine-5'-triphosphate

B blue

b minor axis length of a spheroid

BrdU bromodeoxyuridine

BSA bovine serum albumin

C Celsius

CO_2 carbon dioxide

C_0 oxygen concentration in the medium

C_1 oxygen threshold of hypoxia

C_2 oxygen threshold of severe hypoxia

cAMP cyclic adenosine monophosphate

CDK cyclin-dependent kinase

CS citrate synthase

CT computerized tomography

Cu copper

CV corrected volume

D diffusion coefficient

DLD-1 human colon adenocarcinoma cell line

DNA deoxyribonucleic acid

DT doubling time

DU-145 prostate cancer cells

EDTA ethylenediaminetetraacetic acid

EF5 (2-(2-Nitro-1*H*-imidazol-1-yl)-*N*-(2,2,3,3,3-pentafluoropropyl)acetamide)

EGF epidermal growth factor

EMT-6 human breast cancer cells

EMT6 mouse mammary tumour cell line

EMT6/Ro mouse mammary tumour cell line

ENTPD5 endoplasmic reticulum enzyme

ET cells pluripotent neural stem cells

FBPase2 fructose bisphosphatase 2

FBS fetal bovine serum

F-2,6-BP fructose-2,6-bisphosphate

G geometric mean

G green

G0-phase quiescent phase of cell cycle

G1-phase gap 1 phase of the cell cycle

G2-phase gap 2 phase of the cell cycle

G-6-P glucose-6-phosphate

h hour

HCL hydrogen chloride

Hek293 human embryonic kidney cells

HeLa human cervical cancer cells

HepG2 hepatoma cell line

HIF-1 hypoxia-inducible factor-1

HKII hexokinase II

HRP horseradish peroxidise

IF immunofluorescent

IHC Immunohistochemical

K_c carrying capacity

K Michaelis constant

L litre

LDHV lactate dehydrogenase-V

ln natural logarithm

LNCaP human prostate cancer cells

M Molarity

M-phase mitosis

MAPK mitogen-activated protein kinase

MCF-7 human breast cancer cells

MDA-MB-231 human breast cancer cells

MEL28 human melanoma cell line

$MgSO_4$ magnesium sulphate

min minute

MRI magnetic resonance imaging

mRNA messenger ribonucleic acid

mTOR mammalian target of rapamycin

N tumour spheroid volume

NAD+ nicotinamide adenine dinucleotide oxidized form

NADH nicotinamide adenine dinucleotide reduced form

NADP+ nicotinamide adenine dinucleotide phosphate oxidized form

NADPH nicotinamide adenine dinucleotide phosphate reduced form

OCT optimal cutting temperature compound

ODE ordinary differential equation

P cross-sectional perimeter

p21 cyclin-dependent kinase inhibitor

p27 cyclin-dependent kinase inhibitor

p53 tumour suppressor protein

PBS phosphate buffered saline

PC-3 prostate cancer cells

PCNA proliferating cell nuclear antigen

PDE partial differential equation

PDH pyruvate dehydrogenase

PDK pyruvate dehydrogenase kinase

PKM2 pyruvate kinase M2

PET positron emission tomography

PFA paraformaldehyde

PFK-1 phosphofructokinase-1

PFK-2 phosphofruktokinase-2

PI propidium iodide

PI3K phosphatidylinositol 3-OH kinase

PKM2 pyruvate kinase M2

PO2 oxygen partial pressure (tension)

pRb retinoblastoma protein

PTEN phosphoinositide phosphatase

PVDF polyvinylidene fluoride

pVHL von Hippel–Lindau tumour suppressor protein

r linear growth rate

R radius of the spheroid

R red

$\boldsymbol{R_1}$ radius of hypoxia

$\boldsymbol{R_2}$ radius of severe hypoxia

RECIST Response Evaluation Criteria In Solid Tumors

RKO colon carcinoma cells

ROS Reactive Oxygen Species

rpm revolutions per minute

s oxygen solubility constant

SDS-PAGE sodium dodecyl sulphate-polyacrylamide gel electrophoresis

sec second

S_O amount of oxygen dissolved in the medium

S-phase DNA synthesis phase of the cell cycle

t time

T typical time for cell division

TCA tricarboxylic acid cycle

Tris tris(hydroxymethyl)aminomethane

TS tumour spheroid

UV ultraviolet

v maximal rate of oxygen consumption

V volume

V79-171b Chinese hamster lung fibroblasts

α alpha

β beta

δ non-proliferating cell oxygen consumption fraction

J diffusive flux

∇ gradient operator

γ sphericity

λ lambda (wavelength)

μ micro

m mili

n nano

ø diameter

Bibliography

1. Jemal, A., F. Bray, M.M. Center, J. Ferlay, E. Ward, and D. Forman, *Global cancer statistics.* CA: Cancer J. Clin., 2011. **61**(2): p. 69-90.
2. Siegel, R., D. Naishadham, and A. Jemal, *Cancer statistics, 2012.* CA: Cancer J. Clin., 2012. **62**(1): p. 10-29.
3. Ma, X. and H. Yu, *Global burden of cancer.* Yale J. Biol. Med., 2006. **79**(3-4): p. 85-94.
4. Kinzler, K.W. and B. Vogelstein, *Lessons from hereditary colorectal cancer.* Cell, 1996. **87**(2): p. 159-170.
5. Delattre, O., D.J. Law, Y. Remvikos, X. Sastre, A.P. Feinberg, S. Olschwang, T. Melot, R.J. Salmon, P. Validire, and G. Thomas, *Multiple genetic alterations in distal and proximal colorectal cancer.* Lancet., 1989. **334**(8659): p. 353-356.
6. Weinberg, R.A., *The biology of cancer*. 2007: Garland Science. 796.
7. Hanahan, D. and R.A. Weinberg, *The hallmarks of cancer.* Cell, 2000. **100**(1): p. 57-70.
8. Brown, J.M., *Tumor hypoxia in cancer therapy.* Methods Enzymol., 2007. 435: p. 297-321.
9. Oosterhuis, J.W.A., R.F.M. Schapers, M.L.G. Janssen-Heijnen, A.W.G.B. Smeets, and R.P.E. Pauwels, *MIB-1 as a proliferative marker in transitional cell carcinoma of the bladder: Clinical significance and comparison with other prognostic factors.* Cancer, 2000. **88**(11): p. 2598-2605.
10. Bussink, J., J.H.A.M. Kaanders, and A.J. van der Kogel, *Tumor hypoxia at the micro-regional level: clinical relevance and predictive value of exogenous and endogenous hypoxic cell markers.* Radiother. Oncol., 2003. **67**(1): p. 3-15.
11. Koshiji, M., Y. Kageyama, E.A. Pete, I. Horikawa, C. Barrett, and L.E. Huang, *HIF-1α induces cell cycle arrest by functionally counteracting Myc.* EMBO J., 2004. **23**(9): p. 1949–1956.
12. Bussink, J., J.H.A.M. Kaanders, P.F.J.W. Rijken, J.P.W. Peters, R.J. Hodgkiss, H.A.M. Marres, and A.J. van der Kogel, *Vascular architecture and microenvironmental parameters in human squamous cell carcinoma xenografts: Effects of carbogen and nicotinamide.* Radiother. Oncol., 1999. **50**(2): p. 173-184.
13. Hoskin, P.J., A. Sibtain, F.M. Daley, M.I. Saunders, and G.D. Wilson, *The immunohistochemical assessment of hypoxia, vascularity and proliferation in bladder carcinoma.* Radiother. Oncol., 2004. **72**(2): p. 159-168.
14. Wijffels, K.I.E.M., H.A.M. Marres, J.P.W. Peters, P.F.J.W. Rijken, A.J. van der Kogel, and J.H.A.M. Kaanders, *Tumour cell proliferation under hypoxic conditions in human head and neck squamous cell carcinomas.* Oral Oncol., 2008. **44**(4): p. 335-344.
15. Morgan, D.O., *Principles of CDK regulation.* Nature, 1995. **374**(6518): p. 131-134.
16. Goda, N., H.E. Ryan, B. Khadivi, W. McNulty, R.C. Rickert, and R.S. Johnson, *Hypoxia-inducible factor 1α is essential for cell cycle arrest during hypoxia.* Mol. Cell. Biol., 2003. **23**(1): p. 359-369.

17. Okuyama, H., H. Endo, T. Akashika, K. Kato, and M. Inoue, *Downregulation of c-MYC protein levels contributes to cancer cell survival under dual deficiency of oxygen and glucose.* Cancer Res., 2010. **70**(24): p. 10213-10223.
18. Semenza, G.L., P.H. Roth, H.M. Fang, and G.L. Wang, *Transcriptional regulation of genes encoding glycolytic enzymes by hypoxia-inducible factor 1.* J. Biol. Chem., 1994. **269**(38): p. 23757-23763.
19. Chen, C., N. Pore, A. Behrooz, F. Ismail-Beigi, and A. Maity, *Regulation of glut1 mRNA by hypoxia-inducible factor-1. Interaction between H-ras and hypoxia.* J. Biol. Chem., 2001. **276**(12): p. 9519-9525.
20. Bos, R., J.J.M. van der Hoeven, E. van der Wall, P. van der Groep, P.J. van Diest, E.F.I. Comans, U. Joshi, G.L. Semenza, O.S. Hoekstra, A.A. Lammertsma, and C.F.M. Molthoff, *Biologic correlates of 18 fluorodeoxyglucose uptake in human breast cancer measured by positron emission tomography.* J. Clin. Oncol., 2002. **20**(2): p. 379-387.
21. Dang, C.V., B.C. Lewis, C. Dolde, G. Dang, and H. Shim, *Oncogenes in tumor metabolism, tumorigenesis, and apoptosis.* J. Bioenerg. Biomembr., 1997. **29**(4): p. 345-354.
22. Semenza, G.L., B.-H. Jiang, S.W. Leung, R. Passantino, J.-P. Concordet, l, P. Maire, and A. Giallongo, *Hypoxia response elements in the aldolase A, enolase 1, and lactate dehydrogenase a gene promoters contain essential binding sites for hypoxia-inducible factor 1.* J. Biol. Chem., 1996. **271**(51): p. 32529-32537.
23. Liu, H., D. Huang, D.L. McArthur, L.G. Boros, N. Nissen, and A.P. Heaney, *Fructose induces transketolase flux to promote pancreatic cancer growth.* Cancer Res., 2010. **70**(15): p. 6368-6376.
24. Locasale, J. and L. Cantley, *Altered metabolism in cancer.* BMC Biol., 2010. **8**(1): p. 88.
25. DeBerardinis, R.J., J.J. Lum, G. Hatzivassiliou, and C.B. Thompson, *The biology of cancer: metabolic reprogramming fuels cell growth and proliferation.* Cell Metab., 2008. **7**(1): p. 11-20.
26. Kim, J.-W., I. Tchernyshyov, G.L. Semenza, and C.V. Dang, *HIF-1-mediated expression of pyruvate dehydrogenase kinase: A metabolic switch required for cellular adaptation to hypoxia.* Cell Metab., 2006. **3**(3): p. 177-185.
27. Vander Heiden M.G., Cantley L.C., and Thompson C.B., *Understanding the Warburg effect: the metabolic requirements of cell proliferation.* Science, 2009. **324**(5930): p. 1029–1033.
28. Ward, P.S. and C.B. Thompson, *Signaling in control of cell growth and metabolism.* Cold Spring Harb Perspect Biol., 2012 Jul 1; **4**(7).
29. Jiang, B.-H., F. Agani, A. Passaniti, and G.L. Semenza, *V-SRC Iiduces expression of hypoxia-inducible factor 1 (HIF-1) and transcription of genes encoding vascular endothelial growth factor and enolase 1: involvement of HIF-1 in tumor progression.* Cancer Res., 1997. **57**(23): p. 5328-5335.
30. Semenza, G.L., *Targeting HIF-1 for cancer therapy.* Nat. Rev. Cancer, 2003. **3**(10): p. 721-732.
31. Jiang, B.-H., G. Jiang, J.Z. Zheng, Z. Lu, T. Hunter, and P.K. Vogt, *Phosphatidylinositol 3-kinase signaling controls levels of hypoxia-inducible factor 1.* Cell Growth Differ., 2001. **12**(7): p. 363-369.
32. Richard, D.E., E. Berra, E. Gothié, D. Roux, and J. Pouysségur, *p42/p44 Mitogen-activated protein kinases phosphorylate hypoxia-inducible factor 1α (HIF-1α) and enhance the transcriptional activity of HIF-1.* J. Biol. Chem., 1999. **274**(46): p. 32631-32637.
33. Lum, J.J., T. Bui, M. Gruber, J.D. Gordan, R.J. DeBerardinis, K.L. Covello, M.C. Simon, and C.B. Thompson, *The transcription factor HIF-1α plays a critical role in the growth factor-dependent regulation of both aerobic and anaerobic glycolysis.* Genes Dev., 2007. **21**(9): p. 1037-1049.

34. Baggetto, L.G., *Deviant energetic metabolism of glycolytic cancer cells.* Biochimie, 1992. **74**(11): p. 959-974.
35. Rodríguez-Enríquez, S., J.C. Gallardo-Pérez, A. Avilés-Salas, A. Marín-Hernández, L. Carreño-Fuentes, V. Maldonado-Lagunas, and R. Moreno-Sánchez, *Energy metabolism transition in multi-cellular human tumor spheroids.* J. Cell. Physiol., 2008. **216**(1): p. 189-197.
36. Semenza, G.L., *Tumor metabolism: cancer cells give and take lactate.* J. Clin. Invest., 2008. **118**(12): p. 3835-3837.
37. Colozza, M., E. Azambuja, F. Cardoso, C. Sotiriou, D. Larsimont, and M.J. Piccart, *Proliferative markers as prognostic and predictive tools in early breast cancer: where are we now?* Ann. Oncol., 2005. **16**(11): p. 1723-1739.
38. Betge, J., M.J. Pollheimer, R.A. Lindtner, P. Kornprat, A. Schlemmer, P. Rehak, M. Vieth, G. Hoefler, and C. Langner, *Intramural and extramural vascular invasion in colorectal cancer: prognostic significance and quality of pathology reporting.* Cancer, 2012. **118**(3): p. 628-638.
39. Caretti, V., I. Zondervan, D.H. Meijer, S. Idema, W. Vos, B. Hamans, M. Bugiani, E. Hulleman, P. Wesseling, W.P. Vandertop, D.P. Noske, G. Kaspers, C.F.M. Molthoff, and T. Wurdinger, *Monitoring of tumor growth and post-irradiation recurrence in a diffuse intrinsic pontine glioma mouse model.* Brain Pathol., 2011. **21**(4): p. 441-451.
40. Erlichman, C. and D. Vidgen, *Cytotoxicity of adriamycin in MGH-U1 cells grown as monolayer cultures, spheroids, and xenografts in immune-deprived mice.* Cancer Res., 1984. **44**(11): p. 5369-75.
41. Schuh, J.C.L., *Trials, tribulations, and trends in tumor modeling in mice.* Toxicol. Pathol., 2004. **32**(1 suppl): p. 53-66.
42. Brurberg, K.G., J.V. Gaustad, C.S. Mollatt, and E.K. Rofstad, *Temporal heterogeneity in blood supply in human tumor xenografts.* Neoplasia, 2008. **10**(7): p. 727–735.
43. Lash, G.E., T.E. Fitzpatrick, and C.H. Graham, *Effect of hypoxia on cellular adhesion to vitronectin and fibronectin.* Biochem. Biophys. Res. Commun., 2001. **287**(3): p. 622-629.
44. Zölzer, F. and C. Streffer, *Increased radiosensitivity with chronic hypoxia in four human tumor cell lines.* Int. J. Radiat. Oncol. Biol. Phys., 2002. **54**(3): p. 910-920.
45. Krtolica, A. and J.W. Ludlow, *Hypoxia arrests ovarian carcinoma cell cycle progression, but invasion is unaffected.* Cancer Res., 1996. **56**(5): p. 1168 –1173.
46. Mansbridge, J.N., W.A. Ausserer, M.A. Knapp, and R.M. Sutherland, *Adaptation of EGF receptor signal transduction to three-dimensional culture conditions: Changes in surface receptor expression and protein tyrosine phosphorylation.* J. Cell. Physiol., 1994. **161**(2): p. 374-382.
47. Olive, P.L. and R.E. Durand, *Drug and radiation resistance in spheroids: cell contact and kinetics.* Cancer Metastasis Rev., 1994. **13**(2): p. 121-138.
48. Bauman, G.S., B.J. Fisher, W. McDonald, V.R. Amberger, E. Moore, and R.F. Del Maestro, *Effects of radiation on a three-dimensional model of malignant glioma invasion.* Int. J. Dev. Neurosci., 1999. **17**(5–6): p. 643-651.
49. Monazzam, A., R. Josephsson, C. Blomqvist, J. Carlsson, B. Langstrom, and M. Bergstrom, *Application of the multicellular tumour spheroid model to screen PET tracers for analysis of early response of chemotherapy in breast cancer.* Breast Cancer Res., 2007; **9**(4):R45.
50. Herrmann, R., W. Fayad, S. Schwarz, M. Berndtsson, and S. Linder, *Screening for compounds that induce apoptosis of cancer cells grown as multicellular spheroids.* J. Biomol. Screen., 2008. **13**(1): p. 1-8.
51. Sutherland, R.M., J.A. McCredie, and W.R. Inch, *Growth of multicell spheroids in tissue culture as a model of nodular carcinomas.* J. Natl. Cancer. Inst., 1971. **46**(1): p. 113-120.

52. Grizzi, F. and M. Chiriva-Internati, *Cancer: looking for simplicity and finding complexity.* Cancer Cell Int., 2006 Feb 15;6:4.
53. Casciari, J.J., S.V. Sotirchos, and R.M. Sutherland, *Mathematical modelling of microenvironment and growth in EMT6/Ro multicellular tumour spheroids.* Cell Prolif., 1992. **25**(1): p. 1-22.
54. Bertuzzi, A., A. Fasano, A. Gandolfi, and C. Sinisgalli, *ATP production and necrosis formation in a tumour spheroid model.* Math. Model. Nat. Phenom., 2007. **2**(3): p. 30-46.
55. Bertuzzi, A., A. Fasano, A. Gandolfi, and C. Sinisgalli, *Necrotic core in EMT6/Ro tumour spheroids: Is it caused by an ATP deficit?* J. Theor. Biol., 2010. **262**(1): p. 142-150.
56. Venkatasubramanian, R., M.A. Henson, and N.S. Forbes, *Incorporating energy metabolism into a growth model of multicellular tumor spheroids.* J. Theor. Biol., 2006. **242**(2): p. 440-453.
57. Casciari, J.J., S.V. Sotirchos, and R.M. Sutherland, *Variations in tumor cell growth rates and metabolism with oxygen concentration, glucose concentration, and extracellular pH.* J. Cell. Physiol., 1992. **151**(2): p. 386-394.
58. Freyer, J.P. and R.M. Sutherland, *A reduction in the in situ rates of oxygen and glucose consumption of cells in EMT6/Ro spheroids during growth.* J. Cell. Physiol., 1985. **124**(3): p. 516-524.
59. Freyer, J.P., E. Tustanoff, A.J. Franko, and R.M. Sutherland, *In situ oxygen consumption rates of cells in V-79 multicellular spheroids during growth.* J. Cell. Physiol., 1984. **118**(1): p. 53-61.
60. Sarthy, A.V., S.E. Morgan-Lappe, D. Zakula, L. Vernetti, M. Schurdak, J.C.L. Packer, M.G. Anderson, S. Shirasawa, T. Sasazuki, and S.W. Fesik, *Survivin depletion preferentially reduces the survival of activated K-Ras-transformed cells.* Mol. Cancer Ther., 2007. **6**(1): p. 269-276.
61. Kikuchi, H., M.S. Pino, M. Zeng, S. Shirasawa, and D.C. Chung, *Oncogenic KRAS and BRAF differentially regulate hypoxia-inducible factor-1α and -2α in colon cancer.* Cancer Res., 2009. **69**(21): p. 8499-8506.
62. Bos, J.L., *ras oncogenes in human cancer: a review.* Cancer Res., 1989. **49**(17): p. 4682-4689.
63. Wang, J., Y. Liu, Z. Li, Z. Wang, L.X. Tan, M.J. Ryu, B. Meline, J. Du, K.H. Young, E. Ranheim, Q. Chang, and J. Zhang, *Endogenous oncogenic Nras mutation initiates hematopoietic malignancies in a dose- and cell type-dependent manner.* Blood, 2011. **118**(2): p. 368-379.
64. Dexter, D.L., J.A. Barbosa, and P. Calabresi, *N,N-dimethylformamide-induced alteration of cell culture characteristics and loss of tumorigenicity in cultured human colon carcinoma cells.* Cancer Res., 1979. **39**(3): p. 1020-1025.
65. Shah, D., M. Naciri, P. Clee, and M. Al-Rubeai, *NucleoCounter—An efficient technique for the determination of cell number and viability in animal cell culture processes.* Cytotechnology, 2006. **51**(1): p. 39-44.
66. Hanahan, D. and R.A. Weinberg, *Hallmarks of cancer: the next generation.* Cell, 2011. **144**(5): p. 646-674.
67. Smith, P.K., R.I. Krohn, G.T. Hermanson, A.K. Mallia, F.H. Gartner, M.D. Provenzano, E.K. Fujimoto, N.M. Goeke, B.J. Olson, and D.C. Klenk, *Measurement of protein using bicinchoninic acid.* Anal. Biochem., 1985. **150**(1): p. 76-85.
68. Jackson, M.B., *Molecular and Cellular Biophysics*. 2006, New York: Cambridge University Press.
69. Bergmeyer, H.U., *Methods of Enzymatic Analysis*. Vol. 2. 1983, Weinheim: Verlag Chemie.
70. Gore, M.G., *Spectrophotometry and Spectrofluorimentry: A Practical Approach* 2000, Oxford: Oxford University Press.

71. Gerdes, J., H. Lemke, H. Baisch, H.H. Wacker, U. Schwab, and H. Stein, *Cell cycle analysis of a cell proliferation-associated human nuclear antigen defined by the monoclonal antibody Ki-67.* J. Immunol., 1984. **133**(4): p. 1710-1715.
72. Evans, S.M., S. Hahn, D.R. Pook, W.T. Jenkins, A.A. Chalian, P. Zhang, C. Stevens, R. Weber, G. Weinstein, I. Benjamin, N. Mirza, M. Morgan, S. Rubin, W.G. McKenna, E.M. Lord, and C.J. Koch, *Detection of hypoxia in human squamous cell carcinoma by EF5 binding.* Cancer Res., 2000. **60**(7): p. 2018-2024.
73. Koch, C.J., *Measurement of absolute oxygen levels in cells and tissues using oxygen sensors and 2-nitroimidazole EF5.* Method. Enzymol., 2002; **352**: p. 3-31.
74. Koch, C.J., S.M. Evans, and E.M. Lord, *Oxygen dependence of cellular uptake of EF5 [2-(2-nitro-1H-imidazol-1-yl)-N-(2,2,3,3,3-pentafluoropropyl)a cet amide] : analysis of drug adducts by fluorescent antibodies vs bound radioactivity.* Br. J. Cancer, 1995. **72**(4): p. 869–874.
75. Koch, C.K., S.H. Hahn, K.R. Rockwell, J.C. Covey, W.G. McKenna, and S.E. Evans, *Pharmacokinetics of EF5 [2-(2-nitro-1H-imidazol-1-yl)-N-(2,2,3,3,3-pentafluoropropyl)a cet amide] in human patients: implications for hypoxia measurements in vivo by 2-nitroimidazoles.* Cancer Chemother. Pharmacol., 2001. **48**(3): p. 177-187.
76. Marotta, D., J. Karar, W.T. Jenkins, M. Kumanova, K.W. Jenkins, J.W. Tobias, D. Baldwin, A. Hatzigeorgiou, P. Alexiou, S.M. Evans, R. Alarcon, A. Maity, C. Koch, and C. Koumenis, *In vivo profiling of hypoxic gene expression in gliomas using the hypoxia marker EF5 and laser-capture microdissection.* Cancer Res., 2011. **71**(3): p. 779-789.
77. Goodson, W.H., D.H. Moore, B.-M. Ljung, K. Chew, C. Florendo, B. Mayall, H.S. Smith, and F.M. Waldman, *The functional relationship between in vivo bromodeoxyuridine labeling index and Ki-67 proliferation index in human breast cancer.* Breast Cancer Res. Treat., 1998. **49**(2): p. 155-164.
78. Schlüter, C., M. Duchrow, C. Wohlenberg, M.H. Becker, G. Key, H.D. Flad, and J. Gerdes, *The cell proliferation-associated antigen of antibody Ki-67: a very large, ubiquitous nuclear protein with numerous repeated elements, representing a new kind of cell cycle-maintaining proteins.* J. Cell Biol., 1993. **123**(3): p. 513-522.
79. Perou, C.M., S.S. Jeffrey, M. Van De Rijn, C.A. Rees, M.B. Eisen, D.T. Ross, A. Pergamenschikov, C.F. Williams, S.X. Zhu, J.C.F. Lee, D. Lashkari, D. Shalon, P.O. Brown, and D. Botstein, *Distinctive gene expression patterns in human mammary epithelial cells and breast cancers.* Proc. Natl. Acad. Sci. USA, 1999. **96**(16): p. 9212-9217.
80. Marín-Hernández, A., S. Rodríguez-Enríquez, P.A. Vital-González, F.L. Flores-Rodríguez, M. Macías-Silva, M. Sosa-Garrocho, and R. Moreno-Sánchez, *Determining and understanding the control of glycolysis in fast-growth tumor cells.* FEBS J., 2006. **273**(9): p. 1975-1988.
81. Pedersen, P.L., S. Mathupala, A. Rempel, J.F. Geschwind, and Y.H. Ko, *Mitochondrial bound type II hexokinase: a key player in the growth and survival of many cancers and an ideal prospect for therapeutic intervention.* Biochim Biophys Acta., 2002. **1555**(1-3): p. 14-20.
82. Nakashima, R.A., P.S. Mangan, M. Colombini, and P.L. Pedersen, *Hexokinase receptor complex in hepatoma mitochondria: evidence from N,N'-dicyclohexlycarbodiimide-labeling studies for the involvement of the pore-forming protein VDAC.* Biochemistry., 1986. **25**(5): p. 1015-1021.
83. Pastorino, J.G., N. Shulga, and J.B. Hoek, *Mitochondrial binding of hexokinase II inhibits Bax-induced cytochrome c release and apoptosis.* J. Biol. Chem., 2002. **277**(9): p. 7610-7618.
84. Gottlob, K., N. Majewski, S. Kennedy, E. Kandel, R.B. Robey, and N. Hay, *Inhibition of early apoptotic events by Akt/PKB is dependent on the first committed step of glycolysis and mitochondrial hexokinase.* Genes Dev., 2001. **15**(11): p. 1406-1418.

85. Koukourakis, M.I., A. Giatromanolaki, E. Sivridis, K.C. Gatter, T. Trarbach, G. Folprecht, M.M. Shi, D. Lebwohl, T. Jalava, D. Laurent, G. Meinhardt, and A.L. Harris, *Prognostic and predictive role of lactate dehydrogenase 5 (LDH5) expression in colorectal cancer patients treated with PTK787/ZK 222584 (Vatalanib) anti-angiogenic therapy.* Clin. Cancer Res., 2011. **17**(14): p. 4892-4900.
86. Koukourakis, M.I., A. Giatromanolaki, E. Sivridis, K.C. Gatter, and A.L. Harris, *Lactate dehydrogenase 5 expression in operable colorectal cancer: strong association with survival and activated vascular endothelial growth factor pathway--a report of the Tumour Angiogenesis Research Group.* J. Clin. Oncol., 2006. **24**(26): p. 4301-4308.
87. Latt, S.A. and G. Stetten, *Spectral studies on 33258 Hoechst and related bisbenzimidazole dyes useful for fluorescent detection of deoxyribonucleic acid synthesis.* J. Histochem. Cytochem., 1976. **24**(1): p. 24-33.
88. Olive, P.L., D.J. Chaplin, and R.E. Durand, *Pharmacokinetics, binding and distribution of Hoechst 33342 in spheroids and murine tumours.* Br. J. Cancer, 1985. **52**(5): p. 739-746.
89. Santini, M.T., G. Rainaldi, and P.L. Indovina, *Multicellular tumour spheroids in radiation biology.* Int. J. Radiat. Biol., 1999. **75**(7): p. 787-799.
90. Kunz-Schughart, L.A., *Multicellular tumor spheroids: intermediates between monolayer culture and in vivo tumor.* Cell Biol. Int., 1999. **23**(3): p. 157-161.
91. Bartelink, H., A. Begg, J. Coco M., M. van D., L. van 't Veer, P. van der Vaart, and M. Verheij, *Towards prediction and modulation of treatment response.* Radiother. Oncol., 1999. **50**(1): p. 1-11.
92. Kostis, W.J., D.F. Yankelevitz, A.P. Reeves, S.C. Fluture, and C.I. Henschke, *Small pulmonary nodules: reproducibility of three-dimensional volumetric measurement and estimation of time to follow-up CT1.* Radiology., 2004. **231**(2): p. 446-452.
93. Eisenhauer, E.A., P. Therasse, J. Bogaerts, L.H. Schwartz, D. Sargent, R. Ford, J. Dancey, S. Arbuck, S. Gwyther, M. Mooney, L. Rubinstein, L. Shankar, L. Dodd, R. Kaplan, D. Lacombe, and J. Verweij, *New response evaluation criteria in solid tumours: Revised RECIST guideline (version 1.1).* Eur. J. Cancer, 2009. **45**(2): p. 228-247.
94. Therasse, P., E.A. Eisenhauer, and J. Verweij, *RECIST revisited: A review of validation studies on tumour assessment.* Eur. J. Cancer, 2006. **42**(8): p. 1031-1039.
95. Honegger, J., S. Zimmermann, T. Psaras, M. Petrick, M. Mittelbronn, U. Ernemann, M. Reincke, and K. Dietz, *Growth modelling of non-functioning pituitary adenomas in patients referred for surgery.* Eur. J. Endocrinol., 2008. **158**(3): p. 287-294.
96. Nishino, M., D.M. Jackman, H. Hatabu, B.Y. Yeap, L.-A. Cioffredi, J.T. Yap, P.A. Jänne, B.E. Johnson, and A.D. Van den Abbeele, *New Response Evaluation Criteria in Solid Tumors (RECIST) guidelines for advanced non–small cell lung cancer: comparison with original RECIST and impact on assessment of tumor response to targeted therapy.* AJR Am. J. Roentgenol. , 2010. **195**(3): p. W221-W228.
97. Partridge, S.C., J.E. Gibbs, Y. Lu, L.J. Esserman, D. Tripathy, D.S. Wolverton, H.S. Rugo, E.S. Hwang, C.A. Ewing, and N.M. Hylton, *MRI measurements of breast tumor volume predict response to neoadjuvant chemotherapy and recurrence-free survival.* AJR Am. J. Roentgenol., 2005. **184**(6): p. 1774-1781.
98. Cross, S.S., J.P. Bury, P.B. Silcocks, T.J. Stephenson, and D.W.K. Cotton, *Fractal geometric analysis of colorectal polyps.* J. Pathol., 1994. **172**(4): p. 317-323.
99. Martin, M., *Comparing invasive species to metastatic cancers inspires new insights for modelers.* J. Natl. Cancer Inst., 2008. **100**(2): p. 88-89.

100. Begg, A.C., N.J. McNally, D.C. Shrieve, and H. Kärche, *A method to measure the duration of DNA syntheses and the potential doubling time from a single sample.* Cytometry, 1985. **6**(6): p. 620-626.
101. Zhang, X., W. Wang, W. Yu, Y. Xie, X. Zhang, Y. Zhang, and X. Ma, *Development of an in vitro multicellular tumor spheroid model using microencapsulation and its application in anticancer drug screening and testing.* Biotechnol. Prog., 2005. **21**(4): p. 1289-1296.
102. Hall, M.D., C. Martin, D.J.P. Ferguson, R.M. Phillips, T.W. Hambley, and R. Callaghan, *Comparative efficacy of novel platinum(IV) compounds with established chemotherapeutic drugs in solid tumour models.* Biochem. Pharmacol., 2004. **67**(1): p. 17-30.
103. Freyer, J.P., *Decreased mitochondrial function in quiescent cells isolated from multicellular tumor spheroids.* J. Cell. Physiol., 1998. **176**(1): p. 138-149.
104. Frieboes, H.B., X. Zheng, C.-H. Sun, B. Tromberg, R. Gatenby, and V. Cristini, *An integrated computational/experimental model of tumor invasion.* Cancer Res., 2006. **66**(3): p. 1597-1604.
105. Kunz-Schughart, L.A., M. Kreutz, and R. Knuechel, *Multicellular spheroids: a three-dimensional in vitro culture system to study tumour biology.* Int. J. Exp. Pathol., 1998. **79**(1): p. 1-23.
106. Deisboeck, T.S., M.E. Berens, A.R. Kansal, S. Torquato, A.O. Stemmer-Rachamimov, and E.A. Chiocca, *Pattern of self-organization in tumour systems: complex growth dynamics in a novel brain tumour spheroid model.* Cell Prolif., 2001. **34**(2): p. 115-134.
107. Mellor, H.R., D.J.P. Ferguson, and R. Callaghan, *A model of quiescent tumour microregions for evaluating multicellular resistance to chemotherapeutic drugs.* Br. J. Cancer, 2005. **93**(3): p. 302-309.
108. Kelly, C.J., K. Hussien, and R.J. Muschel, *3D tumour spheroids as a model to assess the suitability of [18F]FDG-PET as an early indicator of response to PI3K inhibition.* Nucl. Med. Biol., 2012. **39**(7): p. 986-992.
109. Walenta, S., J. Doetsch, W. Mueller-Klieser, and L.A. Kunz-Schughart, *Metabolic imaging in multicellular spheroids of oncogene-transfected fibroblasts.* J. Histochem. Cytochem., 2000. **48**(4): p. 509-522.
110. Kim, B.-J. and N.S. Forbes, *Flux analysis shows that hypoxia-inducible-factor-1-alpha minimally affects intracellular metabolism in tumor spheroids.* Biotechnol. Bioeng., 2007. **96**(6): p. 1167-1182.
111. Kelm, J.M., N.E. Timmins, C.J. Brown, M. Fussenegger, and L.K. Nielsen, *Method for generation of homogeneous multicellular tumor spheroids applicable to a wide variety of cell types.* Biotechnol. Bioeng., 2003. **83**(2): p. 173-180.
112. Monazzam, A., P. Razifar, O. Lindhe, R. Josephsson, B. Langstrom, and M. Bergstrom, *A new, fast and semi-automated size determination method (SASDM) for studying multicellular tumor spheroids.* Cancer Cell Int., 2005 Nov 14;5:32
113. Landry, J., J.P. Freyer, and R.M. Sutherland, *A model for the growth of multicellular spheroids.* Cell Prolif., 1982. **15**(6): p. 585-594.
114. Durand, R.E., *Cell cycle kinetics in an in vitro tumor model.* Cell Prolif., 1976. **9**(5): p. 403-412.
115. Folkman, J. and M. Hochberg, *Self-regulation of growth in three dimensions.* J. Exp. Med., 1973. **138**(4): p. 745-753.
116. Freyer, J.P. and R.M. Sutherland, *Regulation of growth saturation and development of necrosis in EMT6/Ro multicellular spheroids by the glucose and oxygen supply.* Cancer Res., 1986. **46**(7): p. 3504-3512.
117. Roose, T., S.J. Chapman, and P.K. Maini, *Mathematical models of avascular tumor growth.* SIAM Rev., 2007. **49**(2): p. 179-208.

118. Laird, A.K., *Dynamics of tumour growth.* Br. J. Cancer 1964. **18**(3): p. 490-502.
119. Murray, J., *Mathematical Biology I. An Introduction*. Biomathematics. Vol. 17. 2002, New York: Springer-Verlag
120. Collins, V.P., R.K. Loeffler, and H. Tivey, *Observations on growth rates of human tumors.* Am. J. Roentgenol., 1956. **76**(5): p. 988-1000.
121. Chojniak, R. and R.N. Younes, *Pulmonary metastases tumor doubling time: assessment by computed tomography.* Am. J. Clin. Oncol., 2003. **26**(4): p. 374-377.
122. El Sharouni, S.Y., H.B. Kal, and J.J. Battermann, *Accelerated regrowth of non-small-cell lung tumours after induction chemotherapy.* Br. J. Cancer, 2003. **89**(12): p. 2184-2189.
123. Kuroishi, T., S. Tominaga, T. Morimoto, H. Tashiro, S. Itoh, H. Watanabe, M. Fukuda, J. Ota, T. Horino, T. Ishida, T. Yokoe, K. Enomoto, Y. Kashiki, and M. Ogita, *Tumor growth rate and prognosis of breast cancer mainly detected by mass screening.* Cancer Sci., 1990. **81**(5): p. 454-462.
124. Shackney, S.E., G.W. McCormack, and G.J. Cuchural, *Growth rate patterns of solid tumors and their relation to responsiveness to therapy.* Ann. Intern. Med., 1978. **89**(1): p. 107-121.
125. Spratt, J.S. and T.L. Spratt, *Rates of growth of pulmonary metastases and host survival.* Ann. Surg., 1964. **159**(2): p. 161-171.
126. Usuda, K., Y. Saito, M. Sagawa, M. Sato, K. Kanma, S. Takahashi, C. Endo, Y. Chen, A. Sakurada, and S. Fujimura, *Tumor doubling time and prognostic assessment of patients with primary lung cancer.* Cancer, 1994. **74**(8): p. 2239-2244.
127. Schmid, H.-P., J.E. McNeal, and T.A. Stamey, *Observations on the doubling time of prostate cancer. The use of serial prostate-specific antigen in patients with untreated disease as a measure of increasing cancer volume.* Cancer, 1993. **71**(6): p. 2031-2040.
128. Schwartz, M., *A biomathematical approach to clinical tumor growth.* Cancer, 1961. **14**(6): p. 1272-1294.
129. Marušić, M., Ž. Bajzer, J.P. Freyer, and S. Vuk-Pavlović, *Analysis of growth of multicellular tumour spheroids by mathematical models.* Cell Prolif., 1994. **27**(2): p. 73-94.
130. Ballangrud, Å.M., W.-H. Yang, A. Dnistrian, N.M. Lampen, and G. Sgouros, *Growth and characterization of LNCaP prostate cancer cell spheroids.* Clin. Cancer Res., 1999. **5**(10): p. 3171-3176.
131. Verhulst, P.F., *Notice sur la loi que la population suit dans son accroissement.* Corr. Math. Physics 1838. **10**(113).
132. Cramer, J.S., *The early origins of the logit model.* Stud. Hist. Philos. Sci., 2004. **35**(4): p. 613-626.
133. Dumont, T.M., A.I. Rughani, and B.I. Tranmer, *Prediction of symptomatic cerebral vasospasm after aneurysmal subarachnoid hemorrhage with an artificial neural network: Feasibility and comparison with logistic regression models.* World Neurosurg., 2011. **75**(1): p. 57-63.
134. Weedon-Fekjaer, H., B. Lindqvist, L. Vatten, O. Aalen, and S. Tretli, *Breast cancer tumor growth estimated through mammography screening data.* Breast Cancer Res., 2008. **10**(3): p. R41.
135. Sharon, K., *The refractory model: The logistic curve and the history of population ecology.* Q. Rev. Biol., 1982. **57**(1): p. 29-52.
136. Waliszewski, P., *A principle of fractal-stochastic dualism and Gompertzian dynamics of growth and self-organization.* Biosystems., 2005. **82**(1): p. 61-73.
137. Steel, G.G., *Growth Kinetics of Tumours*. 1977, Oxford: Clarendon Press.
138. Kunz-Schughart, L.A., K. Groebe, and W. Mueller-Klieser, *Three-dimensional cell culture induces novel proliferative and metabolic alterations associated with oncogenic transformation.* Int. J. Cancer, 1996. **66**(4): p. 578-586.

139. Smallbone, K., D.J. Gavaghan, R.A. Gatenby, and P.K. Maini, *The role of acidity in solid tumour growth and invasion.* J. Theor. Biol., 2005. **235**(4): p. 476-484.
140. Horas, J.A., O.R. Olguin, and M.G. Rizzotto, *On the surviving fraction in irradiated multicellular tumour spheroids: calculation of overall radiosensitivity parameters, influence of hypoxia and volume effects.* Proc. R. Soc. B, 2005. **50**(8): p. 1689-1701.
141. Wein, L., J. Cohen, and J. Wu, *Dynamic optimization of a linear-quadratic model with incomplete repair and volume-dependent sensitivity and repopulation.* Int. J. Radiat. Oncol., 1999. **47**(4): p. 1073-83.
142. Pettet, G., C. Please, M. Tindall, and D. McElwain, *The migration of cells in multicell tumor spheroids.* Bull. Math. Biol., 2001. **63**(2): p. 231-257.
143. Chignola, R. and R.I. Foroni, *Estimating the growth kinetics of experimental tumors from as few as two determinations of tumor size: implications for clinical oncology.* IEEE Trans. Biomed. Eng., 2005. **52**(5): p. 808-815.
144. Brunton, G.F. and T.E. Wheldon, *The Gompertz equation and the construction of tumour growth curves.* Cell Prolif., 1980. **13**(4): p. 455-460.
145. Ota, D.M. and B. Drewinko, *Growth kinetics of human colorectal carcinoma.* Cancer Res., 1985. **45**(5): p. 2128-2131.
146. Lawlor, E.R., C. Scheel, J. Irving, and P.H. Sorensen, *Anchorage-independent multi-cellular spheroids as an in vitro model of growth signaling in Ewing tumors.* Oncogene, 2002. **21**(2): p. 307-18.
147. Takagi, A., M. Watanabe, Ishii. Y., J. Morita, Y. Hirokawa, T. Matsuzaki, and T. Shiraishi, *Three-dimensional cellular spheroid formation provides human prostate tumor cells with tissue-like features.* Anticancer Res., 2007. **27**(1A): p. 45-53.
148. Graham, C.H., H. Kobayashi, K.S. Stankiewicz, S. Man, S.J. Kapitain, and R.S. Kerbel, *Rapid acquisition of multicellular drug resistance after a single exposure of mammary tumor cells to antitumor alkylating agents.* J. Natl. Cancer Inst., 1994. **86**(13): p. 975-982.
149. Olive, P.L., J.P. Banáth , and H.H. Evans, *Cell killing and DNA damage by etoposide in Chinese hamster V79 monolayers and spheroids: influence of growth kinetics, growth environment and DNA packaging.* Br. J. Cancer, 1993. **67**(3): p. 522-30.
150. St Croix, B., V.A. Flørenes, J.W. Rak, M. Flanagan, N. Bhattacharya, J.M. Slingerland, and R.S. Kerbel, *Impact of the cyclin-dependent kinase inhibitor p27Kip1 on resistance of tumor cells to anticancer agents.* Nat. Med. , 1996. **2**(11): p. 1204-10.
151. Höckel, M. and P. Vaupel, *Tumor hypoxia: definitions and current clinical, biologic, and molecular aspects.* J. Natl. Cancer Inst., 2001. **93**(4): p. 266-276.
152. Vaupel, P. and L. Harrison, *Tumor hypoxia: causative factors, compensatory mechanisms, and cellular response.* Oncologist, 2004. **9**(Suppl 5): p. 4-9.
153. Wouters, A., B. Pauwels, F. Lardon, and J.B. Vermorken, *Review: implications of in vitro research on the effect of radiotherapy and chemotherapy under hypoxic conditions.* Oncologist, 2007. **12**(6): p. 690-712.
154. Ma, N., *HIF-1 is the commander of gateways to cancer.* J. Cancer. Sci. Ther., 2011. **3**(2): p. 35-40.
155. Kim, J.W. and C.V. Dang, *Multifaceted roles of glycolytic enzymes.* Trends Biochem. Sci., 2005. **30**(3): p. 142-150.
156. Aebersold, D.M., P. Burri, K.T. Beer, J. Laissue, V. Djonov, R.H. Greiner, and G.L. Semenza, *Expression of hypoxia-inducible factor-1α.* Cancer Res., 2001. **61**(7): p. 2911-2916.
157. Birner, P., M. Schindl, A. Obermair, C. Plank, G. Breitenecker, and G. Oberhuber, *Overexpression of hypoxia-inducible factor 1α is a marker for an unfavorable prognosis in early-stage invasive cervical cancer.* Cancer Res., 2000. **60**(17): p. 4693-4696.

158. Durand, R.E. and J.A. Raleigh, *Identification of nonproliferating but viable hypoxic tumor cells in vivo.* Cancer Res., 1998. **58**(16): p. 3547-3550.
159. Amellem, O., M. Loffler, and E.O. Pettersen, *Regulation of cell proliferation under extreme and moderate hypoxia: the role of pyrimidine (deoxy)nucleotides.* Br. J. Cancer, 1994. **70**(5): p. 857-866.
160. Pettersen, E.O. and T. Lindmo, *Inhibition of cell-cycle progression by acute treatment with various degrees of hypoxia: Modifications induced by low concentrations of misonidazole present during hypoxia.* Br. J. Cancer, 1983. **48**(6): p. 809-817.
161. Varia, M.A., D.P. Calkins-Adams, L.H. Rinker, A.S. Kennedy, D.B. Novotny, W.C. Fowler Jr, and J.A. Raleigh, *Pimonidazole: A novel hypoxia marker for complementary study of tumor hypoxia and cell proliferation in cervical carcinoma.* Gynecol. Oncol., 1998. **71**(2): p. 270-277.
162. Ljungkvist, A.S.E., J. Bussink, P.F.J.W. Rijken, J.H.A.M. Kaanders, A.J. van der Kogel, and J. Denekamp, *Vascular architecture, hypoxia, and proliferation in first-generation xenografts of human head-and-neck squamous cell carcinomas.* Int. J. Radiat. Oncol. Biol. Phys., 2002. **54**(1): p. 215-228.
163. Kennedy, A., J. Raleigh, G. Perez, D. Calkins, D. Thrall, D. Novotny, and M. Varia, *Proliferation and hypoxia in human squamous cell carcinoma of the cervix: first report of combined immunohistochemical assays.* Int. J. Radiat. Oncol. Biol. Phys., 1997. **37**(4): p. 897-905.
164. Dai, Y., K. Bae, and D.W. Siemann, *Impact of hypoxia on the metastatic potential of human prostate cancer cells.* Int. J. Radiat. Oncol. Biol. Phys., 2011. **81**(2): p. 521-528.
165. Box, A.H. and D.J. Demetrick, *Cell cycle kinase inhibitor expression and hypoxia-induced cell cycle arrest in human cancer cell lines.* Carcinogenesis, 2004. **25**(12): p. 2325-2335.
166. Amellem, O. and E. Pettersen, *Cell inactivation and cell cycle inhibition as induced by extreme hypoxia: the possible role of cell cycle arrest as a protection against hypoxia-induced lethal damage.* Cell Prolif., 1991. **24**(2): p. 127-141.
167. Green, S.L., R.A. Freiberg, and A.J. Giaccia, *p21Cip1 and p27Kip1 regulate cell cycle reentry after hypoxic stress but are not necessary for hypoxia-induced arrest.* Mol. Cell. Biol., 2001. **21**(4): p. 1196–1206.
168. Gardner, L.B., Q. Li, M.S. Park, W.M. Flanagan, G.L. Semenza, and C.V. Dang, *Hypoxia inhibits G1/S transition through regulation of p27 expression.* J. Biol. Chem., 2001. **276**(11): p. 7919-7926.
169. Chen, E.Y., N.M. Mazure, J.A. Cooper, and A.J. Giaccia, *Hypoxia activates a platelet-derived growth factor receptor/phosphatidylinositol 3-kinase/Akt pathway that results in glycogen synthase kinase-3 inactivation.* Cancer Res., 2001. **61**(6): p. 2429-2433.
170. Mazure, N.M., E.Y. Chen, K.R. Laderoute, and A.J. Giaccia, *Induction of vascular endothelial growth factor by hypoxia is modulated by a phosphatidylinositol 3-kinase/Akt signaling pathway in Ha-ras-transformed cells through a hypoxia inducible factor-1 transcriptional element.* Blood, 1997. **90**(9): p. 3322-3331.
171. Gleadle, J.M. and P.J. Ratcliffe, *Induction of hypoxia-inducible factor-1, erythropoietin, vascular endothelial growth factor, and glucose transporter-1 by hypoxia: evidence against a regulatory role for src kinase.* Blood, 1997. **89**(2): p. 503-509.
172. Blum, R., J. Jacob-Hirsch, N. Amariglio, G. Rechavi, and Y. Kloog, *Ras inhibition in glioblastoma down-regulates hypoxia-inducible factor-1α, causing glycolysis shutdown and cell death.* Cancer Res., 2005. **65**(3): p. 999-1006.
173. Castellano, E. and J. Downward, *RAS interaction with PI3K.* Genes Cancer, 2011. **2**(3): p. 261-274.

174. Berra, E., J. Milanini, D.E. Richard, M. Le Gall, F. Viñals, E. Gothié, D. Roux, G. Pagès, and J. Pouysségur, *Signaling angiogenesis via p42/p44 MAP kinase and hypoxia.* Biochem. Pharmacol., 2000. **60**(8): p. 1171-1178.
175. Zundel, W., C. Schindler, D. Haas-Kogan, A. Koong, F. Kaper, E. Chen, A.R. Gottschalk, H.E. Ryan, R.S. Johnson, A.B. Jefferson, D. Stokoe, and A.J. Giaccia, *Loss of PTEN facilitates HIF-1-mediated gene expression.* Genes Dev., 2000. **14**(4): p. 391-396.
176. Cantley, L.C. and B.G. Neel, *New insights into tumor suppression: PTEN suppresses tumor formation by restraining the phosphoinositide 3-kinase/AKT pathway.* Proc. Natl. Acad. Sci., 1999. **96**(8): p. 4240-4245.
177. Hudson, C.C., M. Liu, G.G. Chiang, D.M. Otterness, D.C. Loomis, F. Kaper, A.J. Giaccia, and R.T. Abraham, *Regulation of hypoxia-inducible factor 1α expression and function by the mammalian target of rapamycin.* Mol. Cell. Biol., 2002. **22**(20): p. 7004-7014.
178. Koong, A.C., N.C. Denko, K.M. Hudson, C. Schindler, L. Swiersz, C. Koch, S. Evans, H. Ibrahim, Q.T. Le, D.J. Terris, and A.J. Giaccia, *Candidate genes for the hypoxic tumor phenotype.* Cancer Res., 2000. **60**(4): p. 883-887.
179. Lal, A., H. Peters, B. St. Croix, Z.A. Haroon, M.W. Dewhirst, R.L. Strausberg, J.H.A.M. Kaanders, A.J. van der Kogel, and G.J. Riggins, *Transcriptional response to hypoxia in human tumors.* J. Natl. Cancer Inst., 2001. **93**(17): p. 1337-1343.
180. Kim, J.B., *Three-dimensional tissue culture models in cancer biology.* Semin. Cancer Biol., 2005. **15**(5): p. 365-377.
181. LaRue, K.E.A., E.M. Bradbury, and J.P. Freyer, *Differential regulation of cyclin-dependent kinase inhibitors in monolayer and spheroid cultures of tumorigenic and nontumorigenic fibroblasts.* Cancer Res., 1998. **58**(6): p. 1305-1314.
182. LaRue, K.E.A., M. Khalil, and J.P. Freyer, *Microenvironmental regulation of proliferation in multicellular spheroids is mediated through differential expression of cyclin-dependent kinase inhibitors.* Cancer Res., 2004. **64**(5): p. 1621-1631.
183. Kunz-Schughart, L.A., R.C. Habbersett, and J.P. Freyer, *Mitochondrial function in oncogene-transfected rat fibroblasts isolated from multicellular spheroids.* Am. J. Physiol., 1997. **273**(5 Pt 1): p. C1487-C1495.
184. Gallez, B., C. Baudelet, and B.F. Jordan, *Assessment of tumor oxygenation by electron paramagnetic resonance: principles and applications.* NMR Biomed., 2004. **17**(5): p. 240-262.
185. Höckel, M., K. Schlenger, C. Knoop, and P. Vaupel, *Oxygenation of carcinomas of the uterine cervix: evaluation by computerized O2 tension measurements.* Cancer Res., 1991. **51**(22): p. 6098-6102.
186. Vaupel, P., K. Schlenger, C. Knoop, and M. Höckel, *Oxygenation of human tumors: evaluation of tissue oxygen distribution in breast cancers by computerized O2 tension measurements.* Cancer Res., 1991. **51**(12): p. 3316-3322.
187. Diepart, C., J. Verrax, P.B. Calderon, O. Feron, B.F. Jordan, and B. Gallez, *Comparison of methods for measuring oxygen consumption in tumor cells in vitro.* Anal. Biochem., 2010. **396**(2): p. 250-256.
188. Krohn, K.A., J.M. Link, and R.P. Mason, *Molecular imaging of hypoxia.* J. Nucl. Med., 2008. **49**(Suppl 2): p. 129S-148S.
189. Carreau, A., B.E. Hafny-Rahbi, A. Matejuk, C. Grillon, and C. Kieda, *Why is the partial oxygen pressure of human tissues a crucial parameter? Small molecules and hypoxia.* J. Cell Mol. Med., 2011. **15**(6): p. 1239-1253.
190. Freyer, J.P. and P.L. Schor, *Automated selective dissociation of cells from different regions of multicellular spheroids.* In Vitro Cell. Dev. Biol., 1989. **25**(1): p. 9-19.

191. Evans, S.M. and C.J. Koch, *Prognostic significance of tumor oxygenation in humans.* Cancer Lett., 2003. **195**(1): p. 1-16.
192. Hirschhaeuser, F., C. Dittfeld, J. West, W. Mueller-Klieser, and L.A. Kunz-Schughart, *Multicellular tumor spheroids: An underestimated tool is catching up again.* J. Biotechnol., 2010. **148**(1): p. 3-15.
193. Mueller-Klieser, W.F. and R.M. Sutherland, *Oxygen tensions in multicell spheroids of two cell lines.* Br. J. Cancer, 1982. **45**(2): p. 256-264.
194. Bredel-Geissler, A., U. Karbach, S. Walenta, L. Vollrath, and W. Mueller-Klieser, *Proliferation-associated oxygen consumption and morphology of tumor cells in monolayer and spheroid culture.* J. Cell. Physiol., 1992. **153**(1): p. 44-52.
195. Grote, J., R. Süsskind, and P. Vaupel, *Oxygen diffusivity in tumor tissue (DS-Carcinosarcoma) under temperature conditions within the range of 20–40°C.* Pflügers Arch., 1977. **372**(1): p. 37-42.
196. Schroeder, T., H. Yuan, B.L. Viglianti, C. Peltz, S. Asopa, Z. Vujaskovic, and M.W. Dewhirst, *Spatial heterogeneity and oxygen dependence of glucose consumption in R3230Ac and fibrosarcomas of the fischer 344 rat.* Cancer Res., 2005. **65**(12): p. 5163-5171.
197. Vaupel, P., F. Kallinowski, and P. Okunieff, *Blood flow, oxygen and nutrient supply, and metabolic microenvironment of human tumors: A review.* Cancer Res., 1989. **49**(23): p. 6449-6465.
198. Ganfield, R., P. Nair, and W. Whalen, *Mass transfer, storage, and utilization of O2 in cat cerebral cortex.* Am. J. Physiol., 1970. **219**(3): p. 814-821.
199. Buerk, D.G. and G.M. Saidel, *Local kinetics of oxygen metabolism in brain and liver tissues.* Microvasc. Res., 1978. **16**(3): p. 391-405.
200. Longmuir, I.S., D.C. Martin, H.J. Gold, and S. Sun, *Nonclassical respiratory activity of tissue slices.* Microvasc. Res., 1971. **3**(2): p. 125-141.
201. McGoron, A., P. Nair, and R. Schubert, *Michaelis-Menten kinetics model of oxygen consumption by rat brain slices following hypoxia.* Ann. Biomed. Eng., 1997. **25**(3): p. 565-572.
202. Wilson, D.F., M. Erecińska, C. Drown, and I.A. Silver, *The oxygen dependence of cellular energy metabolism.* Arch. Biochem. Biophys., 1979. **195**(2): p. 485-493.
203. Wagner, B.A., S. Venkataraman, and G.R. Buettner, *The rate of oxygen utilization by cells.* Free Radical Bio. Med., 2011. **51**(3): p. 700-712.
204. Allalunis-Turner, M.J., A.J. Franko, and M.B. Parliament, *Modulation of oxygen consumption rate and vascular endothelial growth factor mRNA expression in human malignant glioma cells by hypoxia.* Br. J. Cancer, 1999. **80**(1-2): p. 104-109.
205. Braems, G. and A. Jensen, *Hypoxia reduces oxygen consumption of fetal skeletal muscle cells in monolayer culture.* J. Dev. Physiol., 1991. **16**(4): p. 209-15.
206. Liu, H., N. Savaraj, W. Priebe, and T.J. Lampidis, *Hypoxia increases tumor cell sensitivity to glycolytic inhibitors: a strategy for solid tumor therapy (Model C).* Biochem. Pharmacol., 2002. **64**(12): p. 1745-1751.
207. Xu, R.-H., H. Pelicano, Y. Zhou, J.S. Carew, L. Feng, K.N. Bhalla, M.J. Keating, and P. Huang, *Inhibition of glycolysis in cancer cells: a novel strategy to overcome drug resistance associated with mitochondrial respiratory defect and hypoxia.* Cancer Res., 2005. **65**(2): p. 613-621.
208. Dang, D.T., F. Chen, L.B. Gardner, J.M. Cummins, C. Rago, F. Bunz, S.V. Kantsevoy, and L.H. Dang, *Hypoxia-inducible factor-1α promotes nonhypoxia-mediated proliferation in colon cancer cells and xenografts.* Cancer Res., 2006. **66**(3): p. 1684-1693.

209. Mueller-Klieser, W.F., *Method for the determination of oxygen consumption rates and diffusion coefficients in multicellular spheroids.* Biophys. J., 1984. **46**(3): p. 343-348.
210. Hystad, M.E. and E.K. Rofstad, *Oxygen consumption rate and mitochondrial density in human melanoma monolayer cultures and multicellular spheroids.* Int. J. Cancer, 1994. **57**(4): p. 532-537.
211. Thomlinson, R.H. and L.H. Gray, *The histological structure of some human lung cancers and the possible implications for radiotherapy.* Br. J. Cancer, 1955. **9**(4): p. 539-549.
212. Greenspan, H.P., *Models for the growth of a solid tumor by diffusion.* Stud. Appl. Math., 1972. **52**(3): p. 317-340.
213. Ward, J.P. and J.R. King, *Mathematical modelling of avascular-tumour growth.* Math. Med. Biol., 1997. **14**(1): p. 39-69.
214. Sherratt, J.A. and M.A.J. Chaplain, *A new mathematical model for avascular tumour growth.* J. Math. Biol., 2001. **43**(4): p. 291-312.
215. Ward, J.P. and J.R. King, *Mathematical modelling of drug transport in tumour multicell spheroids and monolayer cultures.* Math. Biosci., 2003. **181**(2): p. 177-207.
216. Buchwald, P., *FEM-based oxygen consumption and cell viability models for avascular pancreatic islets.* Theor. Biol. Med. Model., 2009 Apr 16;6:5.
217. Kyle, A.H. and A.I. Minchinton, *Measurement of delivery and metabolism of tirapazamine to tumour tissue using the multilayered cell culture model.* Cancer Chemother. Pharmacol., 1999. **43**(3): p. 213-20.
218. Balis, U.J., K. Behnia, B. Dwarakanath, S.N. Bhatia, S.J. Sullivan, M.L. Yarmush, and M. Toner, *Oxygen consumption characteristics of porcine hepatocytes.* Metab. Eng., 1999. **1**(1): p. 49-62.
219. Gerd, F., *The respiration of ascites tumour cells at low oxygen concentrations.* Biochim. Biophys. Acta, 1962. **57**(1): p. 509-519.
220. Tindall, M.J., L. Dyson, K. Smallbone, and P.K. Maini, *Modelling acidosis and the cell cycle in multicellular tumour spheroids.* J. Theor. Biol., 2012 Apr 7;298: p. 107-115.
221. Banaji, M., I. Tachtsidis, D. Delpy, and S. Baigent, *A physiological model of cerebral blood flow control.* Math. Biosci., 2005. **194**(2): p. 125-173.
222. Jiang, Y., J. Pjesivac-Grbovic, C. Cantrell, and J.P. Freyer, *A multiscale model for avascular tumor growth.* Biophys. J., 2005. **89**(6): p. 3884-3894.
223. Lyabakh, K.G. and I.N. Mankovskaya, *Oxygen transport to skeletal muscle working at VO2max in acute hypoxia: theoretical predictions.* Comp. Biochem. Phys. A, 2002. **132**(1): p. 53-60.
224. Nichols, M.G. and T.H. Foster, *Oxygen diffusion and reaction kinetics in the photodynamic therapy of multicell tumour spheroids.* Phys. Med. Biol., 1994. **39**(12): p. 2161-81.
225. Mueller-Klieser, W.F. and R.M. Sutherland, *Oxygen consumption and oxygen diffusion properties of multicellular spheroids from two different cell lines.* Adv. Exp. Med. Biol., 1984. **180**: p. 311–321.
226. Silbey, R.J., R.A. Alberty, and M.G. Bawendi, *Physical Chemistry*. 4th edition ed. 2005, New York: Wiley.
227. Potten, C.S., C. Booth, and D. Hargreaves, *The small intestine as a model for evaluating adult tissue stem cell drug targets.* Cell Prolif., 2003. **36**(3): p. 115-129.
228. Mueller-Klieser, W., J.P. Freyer, and R.M. Sutherland, *Influence of glucose and oxygen supply conditions on the oxygenation of multicellular spheroids.* Br. J. Cancer, 1986. **53**(3): p. 345-353.
229. Skeel, R.D. and M. Berzins, *A method for the spatial discretization of parabolic equations in one space variable.* SIAM J. Sci. Stat. Comput., 1990. **11**(1): p. 1-32.

230. Aquino-Parsons, C., C. Luo, C.M. Vikse, and P.L. Olive, *Comparison between the comet assay and the oxygen microelectrode for measurement of tumor hypoxia.* Radiother. Oncol., 1999. **51**(2): p. 179-185.
231. Cline, J.M., G.L. Rosner, J.A. Raleigh, and D.E. Thrall, *Quantification of CCI-103F labeling heterogeneity in canine solid tumors.* Int. J. Radiat. Oncol., 1997. **37**(3): p. 655-662.
232. Lee, C., J.-S. Kim, and T. Waldman, *PTEN gene targeting reveals a radiation-induced size checkpoint in human cancer cells.* Cancer Res., 2004. **64**(19): p. 6906-6914.
233. Jiang, B.H., G.L. Semenza, C. Bauer, and H.H. Marti, *Hypoxia-inducible factor 1 levels vary exponentially over a physiologically relevant range of O2 tension.* Am. J. Physiol., 1996. **271**(4 Pt 1): p. C1172-C1180.
234. Vukovic, V., H.K. Haugland, T. Nicklee, A.J. Morrison, and D.W. Hedley, *Hypoxia-inducible factor-1α is an intrinsic marker for hypoxia in cervical cancer xenografts.* Cancer Res., 2001. **61**(20): p. 7394-7398.
235. Hammond, E.M., N.C. Denko, M.J. Dorie, R.T. Abraham, and A.J. Giaccia, *Hypoxia links ATR and p53 through replication arrest.* Mol. Cell. Biol., 2002. **22**(6): p. 1834-1843.
236. Dang, C.V. and G.L. Semenza, *Oncogenic alterations of metabolism.* Trends Biochem. Sci., 1999. **24**(2): p. 68-72.
237. Robiolio, M., W.L. Rumsey, and D.F. Wilson, *Oxygen diffusion and mitochondrial respiration in neuroblastoma cells.* Am. J. Physiol., 1989. **256**(6 Pt 1): p. C1207-C1213.
238. Pasdois, P., J.E. Parker, E.J. Griffiths, and A.P. Halestrap, *The role of oxidized cytochrome c in regulating mitochondrial reactive oxygen species production and its perturbation in ischaemia.* Biochem. J., 2011. **436**(2): p. 493-505.
239. Warburg, O., F. Wind, and Negelein E., *The metabolism of tumors in the body.* J. Gen. Physiol., 1927. **8**(6): p. 519–530.
240. Ward, P.S. and C.B. Thompson, *Metabolic reprogramming: A cancer hallmark even warburg did not anticipate.* Cancer Cell, 2012. **21**(3): p. 297-308.
241. Wise, D.R., R.J. DeBerardinis, A. Mancuso, N. Sayed, X.-Y. Zhang, H.K. Pfeiffer, I. Nissim, E. Daikhin, M. Yudkoff, S.B. McMahon, and C.B. Thompson, *Myc regulates a transcriptional program that stimulates mitochondrial glutaminolysis and leads to glutamine addiction.* Proc. Natl. Acad. Sci. U S A 2008. **105**(48): p. 18782-18787.
242. Buzzai, M., D.E. Bauer, R.G. Jones, R.J. DeBerardinis, G. Hatzivassiliou, R.L. Elstrom, and C.B. Thompson, *The glucose dependence of Akt-transformed cells can be reversed by pharmacologic activation of fatty acid [beta]-oxidation.* Oncogene, 2005. **24**(26): p. 4165-4173.
243. Elstrom, R.L., D.E. Bauer, M. Buzzai, R. Karnauskas, M.H. Harris, D.R. Plas, H. Zhuang, R.M. Cinalli, A. Alavi, C.M. Rudin, and C.B. Thompson, *Akt stimulates aerobic glycolysis in cancer cells.* Cancer Res., 2004. **64**(11): p. 3892-3899.
244. Deprez, J., D. Vertommen, D.R. Alessi, L. Hue, and M.H. Rider, *Phosphorylation and activation of heart 6-phosphofructo-2-kinase by protein kinase B and other protein kinases of the insulin signaling cascades.* J. Biol. Chem., 1997. **272**(28): p. 17269-17275.
245. Rathmell, J.C., C.J. Fox, D.R. Plas, P.S. Hammerman, R.M. Cinalli, and C.B. Thompson, *Akt-directed glucose metabolism can prevent Bax conformation change and promote growth factor-independent survival.* Mol. Cell. Biol., 2003. **23**(20): p. 7315-7328.
246. Fang, M., Z. Shen, S. Huang, L. Zhao, S. Chen, T.W. Mak, and X. Wang, *The ER UDPase ENTPD5 promotes protein N-glycosylation, the Warburg effect, and proliferation in the PTEN pathway.* Cell, 2010. **143**(5): p. 711-724.

247. Bauer, D.E., G. Hatzivassiliou, F. Zhao, C. Andreadis, and C.B. Thompson, *ATP citrate lyase is an important component of cell growth and transformation.* Oncogene, 2005. **24**(41): p. 6314-6322.
248. Stryer, L., *Biochemistry*. Fourth Edition ed. 1995, New York: W.H. Feeman and Company.
249. Bentzinger, C.F., K. Romanino, D. Cloëtta, S. Lin, J.B. Mascarenhas, F. Oliveri, J. Xia, E. Casanova, C.F. Costa, M. Brink, F. Zorzato, M.N. Hall, and M.A. Rüegg, *Skeletal muscle-specific ablation of raptor, but not of rictor, causes metabolic changes and results in muscle dystrophy.* Cell Metab., 2008. **8**(5): p. 411-424.
250. Kim, J.-W. and C.V. Dang, *Cancer's molecular sweet tooth and the Warburg effect.* Cancer Res., 2006. **66**(18): p. 8927-8930.
251. Guppy, M., E. Greiner, and K. Brand, *The role of the Crabtree effect and an endogenous fuel in the energy metabolism of resting and proliferating thymocytes.* Eur. J. Biochem., 1993. **212**(1): p. 95-99.
252. Fan, Y., K.G. Dickman, and W.-X. Zong, *Akt and c-Myc differentially activate cellular metabolic programs and prime cells to bioenergetic inhibition.* J. Biol. Chem., 2010. **285**(10): p. 7324-7333.
253. Dang, C.V., A. Le, and P. Gao, *MYC-induced cancer cell energy metabolism and therapeutic opportunities.* Clin. Cancer Res., 2009. **15**(21): p. 6479-6483.
254. Mazurek, S., C.B. Boschek, F. Hugo, and E. Eigenbrodt, *Pyruvate kinase type M2 and its role in tumor growth and spreading.* Semin. Cancer Biol., 2005. **15**(4): p. 300-308.
255. Seyfried, T. and L. Shelton, *Cancer as a metabolic disease.* Nutr. Metab. (Lond). 2010 Jan 27; 7:7.
256. Sonveaux, P., F. Végran, T. Schroeder, M.C. Wergin, J. Verrax, Z.N. Rabbani, C.J. De Saedeleer, K.M. Kennedy, C. Diepart, B.F. Jordan, M.J. Kelley, B. Gallez, M.L. Wahl, O. Feron, and M.W. Dewhirst, *Targeting lactate-fueled respiration selectively kills hypoxic tumor cells in mice.* J. Clin. Invest., 2008. **118**(12): p. 3930-3942.
257. Evan, G.I. and K.H. Vousden, *Proliferation, cell cycle and apoptosis in cancer.* Nature, 2001. **411**(6835): p. 342-348.
258. Yun, J., C. Rago, I. Cheong, R. Pagliarini, P. Angenendt, H. Rajagopalan, K. Schmidt, J.K.V. Willson, S. Markowitz, S. Zhou, L.A. Diaz, V.E. Velculescu, C. Lengauer, K.W. Kinzler, B. Vogelstein, and N. Papadopoulos, *Glucose deprivation contributes to the development of KRAS pathway mutations in tumor cells.* Science, 2009. **325**(5947): p. 1555-1559.
259. Christofk, H.R., M.G. Vander Heiden, M.H. Harris, A. Ramanathan, R.E. Gerszten, R. Wei, M.D. Fleming, S.L. Schreiber, and L.C. Cantley, *The M2 splice isoform of pyruvate kinase is important for cancer metabolism and tumour growth.* Nature, 2008. **452**(7184): p. 230-233.
260. Mazurek, S., A. Michel, and E. Eigenbrodt, *Effect of extracellular AMP on cell proliferation and metabolism of breast cancer cell lines with high and low glycolytic rates.* J. Biol. Chem., 1997. **272**(8): p. 4941-4952.
261. Weber, K., D. Ridderskamp, M. Alfert, S. Hoyer, and R.J. Wiesner, *Cultivation in glucose-deprived medium stimulates mitochondrial biogenesis and oxidative metabolism in HepG2 hepatoma cells.* Biol. Chem., 2002. **383**(2): p. 283–290.
262. Renner, E.D., P.G. Plagemann, and R.W. Bernlohr, *Permeation of glucose by simple and facilitated diffusion by Novikoff rat hepatoma cells in suspension culture and its relationship to glucose metabolism.* J. Biol. Chem., 1972. **247**(18): p. 5765-5776.
263. Rossignol, R., R. Gilkerson, R. Aggeler, K. Yamagata, S.J. Remington, and R.A. Capaldi, *Energy substrate modulates mitochondrial structure and oxidative capacity in cancer cells.* Cancer Res., 2004. **64**(3): p. 985-993.

264. Spratlin, J.L., N.J. Serkova, and S.G. Eckhardt, *Clinical applications of metabolomics in oncology: a review.* Clin. Cancer Res., 2009. **15**(2): p. 431-440.
265. Altenberg, B. and K.O. Greulich, *Genes of glycolysis are ubiquitously overexpressed in 24 cancer classes.* Genomics, 2004. **84**(6): p. 1014-1020.
266. Fell, D.A. and S. Thomas, *Physiological control of metabolic flux: the requirement for multisite modulation.* Biochem. J., 1995. **311**(Pt 1): p. 35-39.
267. Berg, J.M., J.L. Tymoczko, and L. Stryer, *Biochemistry, 5th edition*. 2002, W. H. Freeman and Company.
268. Ko, Y.H., P.L. Pedersen, and J.F. Geschwind, *Glucose catabolism in the rabbit VX2 tumor model for liver cancer: characterization and targeting hexokinase.* Cancer Lett., 2001. **173**(1): p. 83-91.
269. Sánchez-Martínez, C. and J. J. Aragón, *Analysis of phosphofructokinase subunits and isozymes in ascites tumor cells and its original tissue, murine mammary gland.* FEBS Lett., 1997. **409**(1): p. 86-90.
270. Hammond, K.D. and D. Balinsky, *Isozyme studies of several enzymes of carbohydrate metabolism in human adult and fetal tissues, tumor tissues, and cell cultures.* Cancer Res., 1978. **38**(5): p. 1323-1328.
271. Van Veelen, C.W.M., H. Verbiest, A.M.C. Vlug, G. Rijksen, and G.E.J. Staal, *Isozymes of pyruvate kinase from human brain, meningiomas, and malignant gliomas.* Cancer Res., 1978. **38**(12): p. 4681-4687.
272. Diaz-Ruiz, R., S. Uribe-Carvajal, A. Devin, and M. Rigoulet, *Tumor cell energy metabolism and its common features with yeast metabolism.* Biochim. Biophys. Acta., 2009. **1796**(2): p. 252-265.
273. Pilkis, S.J., I.T. Weber, R.W. Harrison, and G.I. Bell, *Glucokinase: structural analysis of a protein involved in susceptibility to diabetes.* J. Biol. Chem., 1994. **269**(35): p. 21925-21928.
274. Wilson, J.E., *An introduction to the isoenzymes of mammalian hexokinase types I-III.* Biochem. Soc. T., 1997. **25**(1): p. 103-107.
275. Shinohara, Y., J. Ichihara, and H. Terada, *Remarkably enhanced expression of the type II hexokinase in rat heaptoma cell line AH130.* FEBS Lett., 1991. **291**(1): p. 55-57.
276. El-Bacha, T., M.S. de Freitas, and M. Sola-Penna, *Cellular distribution of phosphofructokinase activity and implications to metabolic regulation in human breast cancer.* Mol. Genet. Metab., 2003. **79**(4): p. 294-299.
277. Martensen, T.M. and T.E. Mansour, *Heart phosphofructokinase: allosteric kinetics with fructose 6-sulfate.* Biochemistry., 1976. **15**(23): p. 4973-4980.
278. Zancan, P., M. Sola-Penna, C.M. Furtado, and D. Da Silva, *Differential expression of phosphofructokinase-1 isoforms correlates with the glycolytic efficiency of breast cancer cells.* Mol. Genet. Metab., 2010. **100**(4): p. 372-378.
279. Herling, A., M. König, S. Bulik, and H.-G. Holzhütter, *Enzymatic features of the glucose metabolism in tumor cells.* FEBS J., 2011. **278**(14): p. 2436–2459.
280. Mazurek, S. and E. Eigenbrodt, *The tumor metabolome.* Anti-cancer Res., 2003. **23**(2 A): p. 1149-1154.
281. Eigenbrodt, E., M. Reinacher, U. Scheefers-Borchel, H. Scheefers, and R. Friis, *Double role for pyruvate kinase type M2 in the expansion of phosphometabolite pools found in tumor cells.* Criti. Rev. Oncogenesis, 1992. **3**(1-2): p. 91-115.
282. Sun, Q., X. Chen, J. Ma, H. Peng, F. Wang, X. Zha, Y. Wang, Y. Jing, H. Yang, R. Chen, L. Chang, Y. Zhang, J. Goto, H. Onda, T. Chen, M.-R. Wang, Y. Lu, H. You, D. Kwiatkowski, and H. Zhang, *Mammalian target of rapamycin up-regulation of pyruvate kinase isoenzyme type M2 is*

critical for aerobic glycolysis and tumor growth. Proc. Natl. Acad. Sci., 2011. **108**(10): p. 4129-4134.
283. Kornecki-Gerrity, E.H. and D.G. Penney, *The effect of phosphoenolpyruvate, fructose-1,6-diphosphate, alanine and valine on pyruvate kinase from turtle liver and heart.* Comp. Biochem. Physiol. B, 1974. **48**(4): p. 507-511.
284. Marchut, E., M. Gumińska, and T. Kedryna, *The inhibitory effect of various fatty acids on aerobic glycolysis in Ehrlich ascites tumour cells.* Acta Biochim. Pol., 1986. **33**(1): p. 7-16.
285. Burke, R.E., S.C. Harris, and W.L. McGuire, *Lactate dehydrogenase in estrogen-responsive human breast cancer cells.* Cancer Res., 1978. **38**(9): p. 2773-2776.
286. Miles, M.F., P. Hung, and R.A. Jungmann, *Cyclic AMP regulation of lactate dehydrogenase. Quantitation of lactate dehydrogenase M-subunit messenger RNA in isoproterenol-and N6,O2'-dibutyryl cyclic AMP-stimulated rat C6 glioma cells by hybridization analysis using a cloned cDNA probe.* J. Biol. Chem., 1981. **256**(23): p. 12545-12552.
287. Shim, H., C. Dolde, B.C. Lewis, C.-S. Wu, G. Dang, R.A. Jungmann, R. Dalla-Favera, and C.V. Dang, *c-Myc transactivation of LDH-A: implications for tumor metabolism and growth.* Proc. Natl. Acad. Sci., 1997. **94**(13): p. 6658-6663.
288. Leite, T.C., R.G. Coelho, D.D. Silva, W.S. Coelho, M.M. Marinho-Carvalho, and M. Sola-Penna, *Lactate downregulates the glycolytic enzymes hexokinase and phosphofructokinase in diverse tissues from mice.* FEBS Lett., 2011. **585**(1): p. 92-98.
289. Gladden, L.B., *Lactate metabolism: a new paradigm for the third millennium.* J. Physiol., 2004. **558**(1): p. 5-30.
290. Sola-Penna, M., *Metabolic regulation by lactate.* IUBMB Life, 2008. **60**(9): p. 605-608.
291. Papandreou, I., R.A. Cairns, L. Fontana, A.L. Lim, and N.C. Denko, *HIF-1 mediates adaptation to hypoxia by actively downregulating mitochondrial oxygen consumption.* Cell Metab., 2006. **3**(3): p. 187-197.
292. Seagroves, T.N., H.E. Ryan, H. Lu, B.G. Wouters, M. Knapp, P. Thibault, K. Laderoute, and R.S. Johnson, *Transcription factor HIF-1 is a necessary mediator of the pasteur effect in mammalian cells.* Mol. Cell. Biol., 2001. **21**(10): p. 3436-3444.
293. Khaitan, D., S. Chandna, M.B. Arya, and B.S. Dwarakanath, *Establishment and characterization of multicellular spheroids from a human glioma cell line; Implications for tumor therapy.* J. Transl. Med., 2006 Mar 2;4:12.
294. Wolf, A., S. Agnihotri, J. Micallef, J. Mukherjee, N. Sabha, R. Cairns, C. Hawkins, and A. Guha, *Hexokinase 2 is a key mediator of aerobic glycolysis and promotes tumor growth in human glioblastoma multiforme.* J. Exp. Med., 2011. **208**(2): p. 313-326.
295. Gatenby, R.A. and R.J. Gillies, *Why do cancers have high aerobic glycolysis?* Nat. Rev. Cancer, 2004. **4**(11): p. 891-899.
296. Simonnet, H., J. Demont, K. Pfeiffer, L. Guenaneche, R. Bouvier, U. Brandt, H. Schägger, and C. Godinot, *Mitochondrial complex I is deficient in renal oncocytomas.* Carcinogenesis, 2003. **24**(9): p. 1461-1466.
297. López-Ríos, F., M. Sánchez-Aragó, E. García-García, Á.D. Ortega, J.R. Berrendero, F. Pozo-Rodríguez, Á. López-Encuentra, C. Ballestín, and J.M. Cuezva, *Loss of the mitochondrial bioenergetic capacity underlies the glucose avidity of carcinomas.* Cancer Res., 2007. **67**(19): p. 9013-9017.
298. Plas, D.R. and C.B. Thompson, *Cell metabolism in the regulation of programmed cell death.* Trends Endocrin. Met., 2002. **13**(2): p. 75-78.
299. Kroemer, G. and J. Pouyssegur, *Tumor cell metabolism: cancer's Achilles' heel.* Cancer Cell, 2008. **13**(6): p. 472-482.

300. Stern, R., S. Shuster, B.A. Neudecker, and B. Formby, *Lactate stimulates fibroblast expression of hyaluronan and CD44: the Warburg effect revisited.* Exp. Cell Res., 2002. **276**(1): p. 24-31.
301. Koukourakis, M.I., A. Giatromanolaki, and E. Sivridis, *Lactate dehydrogenase isoenzymes 1 and 5: differential expression by neoplastic and stromal cells in non-small cell lung cancer and other epithelial malignant tumors.* Tumor Biol., 2003. **24**(4): p. 199-202.
302. Šmerc, A., E. Sodja, and M. Legiša, *Posttranslational modification of 6-phosphofructo-1-kinase as an important feature of cancer metabolism.* PLoS ONE, 2011. **6**(5): p. e19645.
303. Dunaway, G.A. and T.P. Kasten, *Physiological implications of the alteration of 6-phosphofructo-1-kinase isozyme pools during brain development and aging.* Brain Res., 1988. **456**(2): p. 310-316.
304. Zeitschel, U., R. Schliebs, S. Roßner, V. Bigl, K. Eschrich, and M. Bigl, *Changes in activity and expression of phosphofructokinase in different rat brain regions after basal forebrain cholinergic lesion.* J. Neurochem., 2002. **83**(2): p. 371-380.
305. Dombrauckas, J.D., B.D. Santarsiero, and A.D. Mesecar, *Structural basis for tumor pyruvate kinase M2 allosteric regulation and catalysis.* Biochem., 2005. **44**(27): p. 9417-9429.
306. Allison, W.S., J. Admiraal, and N.O. Kaplan, *The subunits of dogfish M4 lactic dehydrogenase.* J. Biol. Chem., 1969. **244**(17): p. 4743-4749.
307. Kurokawa, T., M. Miyamoto, K. Kato, Y. Cho, Y. Kawarada, Y. Hida, T. Shinohara, T. Itoh, S. Okushiba, S. Kondo, and H. Katoh, *Overexpression of hypoxia-inducible-factor 1[alpha](HIF-1[alpha]) in oesophageal squamous cell carcinoma correlates with lymph node metastasis and pathologic stage.* Br. J. Cancer, 2002. **89**(6): p. 1042-1047.
308. Freyer, J.P. and R.M. Sutherland, *Proliferative and clonogenic heterogeneity of cells from EMT6/Ro multicellular spheroids induced by the glucose and oxygen supply.* Cancer Res., 1986. **46**(7): p. 3513-3520.
309. Buchwald, P., *A local glucose-and oxygen concentration-based insulin secretion model for pancreatic islets.* Theor. Biol. Med. Model., 2011 Jun 21; 8:20.
310. Walenta, S., S. Snyder, Z.A. Haroon, R.D. Braun, K. Amin, D. Brizel, W. Mueller-Klieser, B. Chance, and M.W. Dewhirst, *Tissue gradients of energy metabolites mirror oxygen tension gradients in a rat mammary carcinoma model.* Int. J. Radiat. Oncol. Biol. Phys., 2001. **51**(3): p. 840-848.
311. Turowski, G.A., Z. Rashid, F. Hong, J.A. Madri, and M.D. Basson, *Glutamine modulates phenotype and stimulates proliferation in human colon cancer cell lines.* Cancer Res., 1994. **54**(22): p. 5974-5980.
312. Koukourakis, M.I., M. Pitiakoudis, A. Giatromanolaki, A. Tsarouha, A. Polychronidis, E. Sivridis, and C. Simopoulos, *Oxygen and glucose consumption in gastrointestinal adenocarcinomas: correlation with markers of hypoxia, acidity and anaerobic glycolysis.* Cancer Sci., 2006. **97**(10): p. 1056-1060.
313. Hill, A.V., *The diffusion of oxygen and lactic acid through tissues.* Proc. R. Soc. B, 1928. **104**(728): p. 39-96.
314. Gaglio, D., C. Soldati, M. Vanoni, L. Alberghina, and F. Chiaradonna, *Glutamine deprivation induces abortive S-phase rescued by deoxyribonucleotides in transformed fibroblasts.* PLoS ONE, 2009. **4**(3): p. 1-17.
315. Evans, S.M., K.W. Jenkins, H.I. Chen, W.T. Jenkins, K.D. Judy, W.T. Hwang, R.A. Lustig, A.R. Judkins, M.S. Grady, S.M. Hahn, and C.J. Koch, *The relationship among hypoxia, proliferation, and outcome in patients with de novo glioblastoma: a pilot study.* Transl. Oncol., 2010. **3**(3): p. 160-9.

316. Evans, S.M., S.M. Hahn, D.P. Magarelli, and C.J. Koch, *Hypoxic heterogeneity in human tumors: EF5 binding, vasculature, necrosis, and proliferation.* Am. J. Clin. Oncol., 2001. **24**(5): p. 467-72.
317. Evans, S.M., A.E. Schrlau, A.A. Chalian, P. Zhang, and C.J. Koch, *Oxygen levels in normal and previously irradiated human skin as assessed by EF5 binding.* J. Invest. Dermatol., 2006. **126**(12): p. 2596-2606.
318. Wheaton, W.W. and N.S. Chandel, *Hypoxia. 2. Hypoxia regulates cellular metabolism.* Am. J. Physiol. Cell Physiol., 2011. **300**(3): p. C385-C393.